HAL open science

Chiral magnetic textures in epitaxial thin films with C2v symmetry

Jose Antonio Pena Garcia

To cite this version:

Jose Antonio Pena Garcia. Chiral magnetic textures in epitaxial thin films with C2v symmetry. Materials Science [cond-mat.mtrl-sci]. Université Grenoble Alpes [2020-..], 2021. English. NNT : 2021GRALY046 . tel-03525781v2

HAL Id: tel-03525781

https://theses.hal.science/tel-03525781v2

Submitted on 19 Jan 2022

HAL is a multi-disciplinary open access archive for the deposit and dissemination of scientific research documents, whether they are published or not. The documents may come from teaching and research institutions in France or abroad, or from public or private research centers.

L'archive ouverte pluridisciplinaire **HAL**, est destinée au dépôt et à la diffusion de documents scientifiques de niveau recherche, publiés ou non, émanant des établissements d'enseignement et de recherche français ou étrangers, des laboratoires publics ou privés.

THÈSE

Pour obtenir le grade de

DOCTEUR DE L'UNIVERSITE GRENOBLE ALPES

Spécialité : **NANOPHYSIQUE**

Arrêté ministériel : 25 mai 2016

Présentée par

Jose Antonio PEÑA GARCIA

Thèse dirigée par **Stefania PIZZINI**, Directrice de Recherche, et
codirigée par **Jan VOGEL,** Directeur de Recherche
préparée au sein du **Laboratoire Institut Néel**
dans **l'École Doctorale de Physique**

Textures magnétiques chirales en couches minces épitaxiales avec symétrie C2v

Thèse soutenue publiquement le **12 de juillet de 2021,**
devant le jury composé de :

Monsieur Julio CAMARERO, PROFESSEUR, IMDEA-UAM, Madrid, Rapporteur
Monsieur Mairbek CHSHIEV, PROFESSEUR, CNRS/CEA-SPINTEC, Examinateur
Monsieur Michael FOERSTER, DOCTEUR EN SCIENCES, ALBA SYNCHROTRON, Examinateur
Monsieur Olivier FRUCHART, DIRECTEUR DE RECHERCHE, CNRS/CEA-SPINTEC, Président
Monsieur Joo-Von KIM, CHARGE DE RECHERCHE, CNRS-C2N, Palaiseau, Rapporteur
Monsieur André THIAVILLE, DIRECTEUR DE RECHERCHE, CNRS-LPS, Orsay, Examinateur

To Cheshire Cat

We're all mad here

Abstract

Chirality is a fascinating property of nature, observed for the first time in 1848 by Louis Pasteur, in the optical response of molecules. More generally, chiral textures often appear in physics as a result of symmetry breaking, either spontaneously, for example in macroscopic quantum systems, or when stabilised by a chiral interaction, as in liquid crystals or magnetism. In magnetism, chirality emerges naturally due to a chiral anti-symmetric exchange interaction called Dzyaloshinskii-Moriya interaction (DMI), in systems with a breaking inversion symmetry and a large spin-orbit coupling. In competition with other magnetic interactions, the DMI promotes chiral non-collinear magnetic textures whose symmetry depends on the crystal symmetry.

In this thesis, we study the $Au_{1-x}Pt_x/Co/W(110)$ stack grown epitaxially on sapphire, where inversion symmetry is broken and a large spin-orbit-coupling arises due to the large atomic number of the buffer and capping layers. The particularity of the $Au_{1-x}Pt_x/Co/W(110)$ stack is that it possess a C_{2v} symmetry, which results into an anisotropic DMI, with a Néel and a Bloch component, and an uniaxial strain-induced in-plane anisotropy, in addition to the out-of-plane anisotropy promoted by the spin-orbit-coupling.

The crystal structure and symmetry of the $Au_{1-x}Pt_x/Co/W(110)$ stack is investigated by grazing X-ray diffraction and reflection high energy electron diffraction. We found that the C_{2v} symmetry is conserved as the Pt content increases, and that the $Au_{1-x}Pt_x$ unit cell lattice parameter follows Vegard's law, decreasing monotonously as the Pt content increases.

The evolution of the magnetic parameters as a function of the Au-to-Pt content in the $Au_{1-x}Pt_x/Co/W(110)$ stack is investigate with Brillouin light scattering in the Damon-Eshbach and the magnetostatic-backward-volume-waves configuration. The interfacial anisotropy is found to follow Vegard's law, decreasing monotonously as the Pt content increases. On the other hand, the Néel-type DMI is found to increase non-monotonously up to a certain value with the increasing of Pt content, and to decrease above. The in-plane anisotropy energy density is found to remain constant for all the different Pt compositions and to possess a two-fold symmetry. A non-zero Bloch-type DMI is observed using the magnetostatic-backward-volume-waves configuration for $Au_{0.58}Pt_{0.42}/Co/W(110)$ where the anisotropic Néel-type DMI was found to be maximum.

The different chiral magnetic configurations that can be stabilised in the magnetic stacks are investigated with X-ray magnetic circular dichroism photoemission electron microscopy (XMCD-PEEM). The energy difference of domain walls (DWs) aligned along the two main in-plane directions depends on the Au-to-Pt content, as explained by a one-dimensional model and micromagnetic simulations. When the DW energy difference is high, this leads to the stabilisation of self-organised

stripe domains or to elliptical magnetic skyrmions. Finally, when approaching the spin-reorientation transition and under specific circumstances, magnetic merons, topologically equivalent to half-skyrmion, are observed in magnetic nanodots.

Abstract

La chiralité est une propriété fascinante de la nature, qui fut observée pour la première fois par Louis Pasteur en 1848, dans la réponse optique des molécules. En général, des textures chirales apparaissent en physique lorsqu'il y a brisure de symétrie, soit de façon spontanée, comme dans des systèmes quantiques, ou quand stabilisées par une interaction chirale, comme dans les cristaux liquides ou en magnétisme. En magnétisme, la chiralité apparaît naturellement à cause d'une interaction chirale anti-symétrique appelée interaction Dzyaloshinskii-Moriya (DMI) dans des systèmes avec inversion de symétrie et une large interaction spin-orbite. Quand elle est en compétition avec d'autres interactions magnétiques, la DMI favorise la formation de textures chirales non-colinéaires dont la symétrie dépend de la symétrie cristalline.

Dans cette thèse, nous étudions des empilements de couches minces de $Au_{1-x}Pt_x/Co/W(110)$ déposés de façon épitaxiale sur des substrats de saphir, dans lesquels la symétrie est brisée et une forte interaction spin-orbite est présente grâce aux atomes lourds constituant les couches de buffer et de couverture. Les empilements $Au_{1-x}Pt_x/Co/W(110)$ possèdent une symétrie C_{2v}, qui résulte en une DMI anisotrope, avec une composante Bloch et Néel, aussi bien qu'une anisotropie magnéto-cristallline dans le plan des couches qui s'ajoute à l'anisotropie dans la direction perpendiculaire au plan.

La structure cristalline et la symétrie de la multicouche $Au_{1-x}Pt_x/Co/W(110)$ a été étudiée par diffraction rasante de rayons X et par diffraction d'électrons à haute énergie. Nous avons observé que la symétrie C_{2v} est conservée quand la concentration de Pt augmente, et que les paramètres cristallins suivent la loi de Vegard, diminuant de façon monotone avec la concentration de Pt.

L'évolution des paramètres magnétiques en fonction de la concentration de Pt dans les multicouches $Au_{1-x}Pt_x/Co/W(110)$ a été étudié par diffusion de lumière Brillouin dans la géomètrie Damon-Eshbach et dans la configuration dite " magnetostatic-backward-volume-waves". L'anisotropie d'interface suit la loi de Vegard, diminuant de façon monotone avec la concentration de Pt. La DMI de type Néel augmente de façon non-monotone jusqu'à une certaine concentration de Pt, puis diminue. L'anisotropie dans le plan reste constante pour toutes les concentrations de Pt, et possède une symétrie C_{2v}. Une DMI de type Bloch différente de zéro est observée en utilisant la configuration « magnetostatic-backward-volume-waves » dans la multicouche $Au_{0.58}Pt_{0.42}/Co/W(110)$, où la DMI de type Néel a la valeur maximum.

Les différentes configurations chirales stabilisées dans les multicouches ont été étudiées par microscopie de photoemission d'électrons associée au dichroisme circulaire magnétique des rayons X (XMCD-PEEM) au synchrotron ELETTRA (Italie). La différence d'énergie de parois de domaines alignées selon les deux directions

cristallographiques varie selon la concentration de Pt, comme expliqué par des calculs analytiques 1D et des simulations micromagnétiques. Quand cette différence d'énergie est importante, on observe la stabilisation de domaines auto-organisés et de skyrmions magnétiques. Au voisinage de la réorientation de spin et dans des circonstances particulières, des merons magnétiques, (équivalents topologiquement à des demi-skyrmions), ont été observés dans des nanostructures magnétiques.

Contents

1 Introduction **1**

2 Magnetism in thin films **6**

2.1 Principles of micromagnetism 7

2.2 Energies at play 7

2.2.1 Heisenberg exchange 8

2.2.2 Zeeman Energy 9

2.2.3 Dipolar Energy 9

2.2.4 Magnetic anisotropy 11

2.2.5 Dzyaloshinskii-Moriya interaction 15

2.2.6 Summary 18

2.3 Characteristic lengths 19

2.4 Magnetic dynamics 19

2.4.1 Spin-Transfer Torque 20

2.4.2 Spin-Orbit Torque 21

3 Chiral Magnetic textures **23**

3.1 Domain walls in ultrathin films with perpendicular magnetic anisotropy 24

3.1.1 Introduction 24

3.1.2 Statics 25

3.1.3 Dynamics 27

3.2 Topology in a nutshell 41

3.3 Magnetic skyrmions 43

3.3.1 Skyrmion stability 45

3.3.2 Skyrmion or skyrmion-bubbles 47
3.4 Magnetic antiskyrmions 47
3.5 Magnetic meron 49

4 Growth and characterisation: $Au_{1-x}Pt_x$/Co/W(110) 50
4.1 Overview of the ultra-high vacuum system and the structural characterisation 52
4.2 Growth of $Au_{1-x}Pt_x/Co(t_{Co})/W(110)$ stack 53
4.2.1 Growth procedure 53
4.2.2 Sapphire substrate 53
4.2.3 Tungsten 55
4.2.4 Cobalt 57
4.2.5 Gold and platinum 62
4.2.6 Summary 64
4.3 Magnetic characterisation 65
4.3.1 BLS introduction 65
4.3.2 C_{2v} DMI symmetry 68
4.3.3 Spontaneous magnetisation 71
4.3.4 Magnetic exchange 71
4.3.5 Magnetic anisotropy 72
4.3.6 Néel-type DMI 78
4.3.7 Bloch-type DMI 82
4.3.8 Summary 83
4.4 Field-driven domain-wall motion 85
4.4.1 Introduction 85
4.4.2 Experiments: DW vs B_z 86
4.4.3 DW motion vs B_z with B_x 92
4.4.4 Summary 94

5 Magnetic textures: $Au_{1-x}Pt_x$/Co/W(110) 95
5.1 Imaging the domain and domain wall structure 96
5.1.1 XMCD 96
5.1.2 PEEM 97
5.1.3 XMCD-PEEM 98
5.2 Stripe domains in $Au_{1-x}Pt_x/Co(t_{Co})/W(110)$ 100
5.2.1 One-dimensional model 100

5.2.2 Observation by Kerr and XMCD-PEEM 104
5.2.3 Summary 110
5.3 Skyrmions 111
5.3.1 Introduction 111
5.3.2 Observation by XMCD-PEEM 111
5.3.3 Why an elliptical shape? 112
5.4 Merons 118
5.4.1 Introduction 118
5.4.2 Observation by XMCD-PEEM 120
5.4.3 Stabilisation of merons 124

6 Conclusions **130**
6.1 Future Work 132

References **134**

List of Figures

1.1 Three dimensional technology: Racetrack Memory 4.0. Red and blue regions represent areas that are oppositely magnetized. 2
1.2 Micromagnetic simulated depending on the Dzyaloshinskii-Moriya interaction strength and sign 3

2.1 Spherical reference system 8
2.2 Demagnetising field inside a uniformly magnetised thin film 10
2.3 Atomistic spin-orbit coupling 12
2.4 Magnetocrystalline anisotropy energies 13
2.5 Interfacial anisotropy 15
2.6 Interface three-site Dzyaloshinskii-Moriya interaction mechanism for ultrathin magnetic films 16
2.7 Torques and effective field affecting the magnetisation vector 20

3.1 Sketch of domain walls in perpendicularly magnetised thin films 24
3.2 Magnetisation profile of a Néel domain wall 25
3.3 Chiral Néel domain wall in the presence of the Dzyaloshinskii-Moriya interaction 26
3.4 Sketch of the collective coordinates 28
3.5 Different regimes of the field-driven Néel domain wall motion in the presence of Dzyaloshinskii-Moriya interaction 29
3.6 One-dimensional and micromagnetic simulations of the field-driven motion of a Néel domain wall in the presence of the Dzyaloshinskii-Moriya interaction 32
3.7 Experimental domain wall speed driven by an out-of-plane magnetic field . 34

3.8 Domain wall dynamics by spin-transfer torque for different non-adiabatic parameters . . . 38
3.9 Manganite Nitride spin-transfer torque-domain wall motion . . . 39
3.10 Bloch and Néel-type skyrmions and merons in the real space and their stereographical projection . . . 42
3.11 Experimental observation of Bloch-type and Néel-type skyrmion . . . 43
3.12 Magnetic skyrmion energies variation . . . 46
3.13 Magnetic antiskyrmion . . . 48

4.1 Crystal structure of hcp-Al_2O_3 . . . 54
4.2 Crystal structure bcc-W . . . 56
4.3 Morphology of as-deposited tungsten studied wit scanning tunneling microscopy and after annealing with x-ray diffraction . . . 57
4.4 Crystal structure hcp-Co . . . 58
4.5 hcp-Co(0001)/bcc-W(110) reflection high energy electron diffraction along the two main in-plane directions . . . 59
4.6 hcp-Co(0001)/bcc-W(110) interface . . . 60
4.7 Crystal structure fcc-Au . . . 62
4.8 In-plane lattice parameter fcc-$Au_{1-x}Pt_x$ for different compositions . . . 63
4.9 Feynman diagram of the Brillouin light scattering mechanism . . . 66
4.10 Spin waves propagation geometries . . . 67
4.11 Brillouin light scattering framework W(110) for anisotropic Dzyaloshinskii–Moriya interaction . . . 69
4.12 Polar representation of the anisotropic Dzyaloshinskii–Moriya interaction . 70
4.13 Hysteresis loops taken by polar magneto-optical Kerr effect under the application of an external magnetic field in $Au_{1-x}Pt_x/Co(t_{Co})/W(110)$ . . . 72
4.14 Brillouin light scattering spectrum for the $Au_{1-x}Pt_x/Co(0.78nm)/W(110)$ stack as function of the Au-to-Pt content x . . . 75
4.15 Magnetic anisotropies as function of Pt content determined in the Demon-Eshbach configuration . . . 76
4.16 Angular dependence of the symmetric component of the spin-wave frequency in the magnetostatic backward volume waves configuration . . . 77
4.17 Spin-wave frequency asymmetry as a function of the wavector along the two main in-plane directions measured in the Damon-Eshbach configuration for the $\mathbf{Au_{0.58}Pt_{0.42}/\ Co(0.78nm)/W(110)}$ stack . . . 78
4.18 Néel-type Dzyaloshinskii–Moriya interaction as function of the Pt content . 79

4.19 Ab-initio calculations for Au/Co and Pt/Co 80
4.20 Brillouin light scattering geometry scheme used in the backward-volume configuration on the W(110) plane 81
4.21 Angular dependence of the spin-wave frequency asymmetry in the magnetostatic backward volume waves configuration 82
4.22 Field-driven domain wall motion for different Au-to-Pt compositions of the $Au_{1-x}Pt_x$/Co(0.6nm)/W(110) stacks 86
4.23 Domain shape for different Au-to-Pt content of the $Au_{1-x}Pt_x$/Co(0.6nm)/W(110) stack 88
4.24 Calculated Walker velocity as function of the in-plane anisotropy 89
4.25 Field-driven domain wall motion for Au/Co(0.6nm)/W(110) 90
4.26 Field-driven domain wall motion for $Au_{0.8}Pt_{0.2}$/Co(0.6nm)/W(110) 91
4.27 Field-driven domain wall motion for $Au_{0.67}Pt_{0.33}$/Co(0.6nm)/W(110) . . . 92
4.28 Field-driven domain wall motion for Au/Co(0.6nm)/W(110) under an static in-plane field 93

5.1 X-ray magnetic circular dichroism working principle 96
5.2 X-ray photo-emission electron microscope 99
5.3 Micromagnetic W(110) framework 100
5.4 Variation of domain wall internal magnetisation and energy density as function of dimensionless parameters 102
5.5 Anisotropic domain wall energy phase diagram 103
5.6 Calculated variation of κ and d_0 as function of the cobalt thickness for different platinum compositions 104
5.7 Differential Kerr images showing reversed domains for different compositions of Au-to-Pt, $Au_{1-x}Pt_x$ 105
5.8 Micromagnetic simulations of self-organised stripe domains 106
5.9 X-ray magnetic circular dichroism photoemission electron microscopy images for $Au_{0.67}Pt_{0.33}$/Co(t_{Co})/W(110) taken with the projection of the x-ray beam on the sample surface parallel to the hard in-plane axis direction . . . 108
5.10 X-ray magnetic circular dichroism photoemission electron microscopy image for $Au_{0.67}Pt_{0.33}$/Co(0.8nm)/W(110) with the projection of the x-ray beam on the sample surface parallel to the easy in-plane axis direction 109
5.11 Elliptical skyrmion observed with x-ray magnetic circular dichroism photoemission electron microscopy 112

5.12 Micromagnetic simulated elliptical skyrmion due to different sources of anisotropy 113
5.13 Skyrmion ellipticity phase diagram. 115
5.14 Micromagnetic stabilised elliptical skyrmion with experimental parameters 116
5.15 Schematic representation of a Néel Skyrmion and a Meron 119
5.16 Scanning electron microscopy image of the nanostructures 120
5.17 X-ray magnetic circular dichroism photoemission electron microscopy image for $Au_{0.58}Pt_{0.42}/Co(0.75nm)/W(110)$ with the projection of the x-ray beam on the sample surface parallel to the $W[\bar{1}10]$ direction. 121
5.18 Magnetic meron observed at room temperature and zero external magnetic field. 122
5.19 Magnetic response of magnetic merons observed by x-ray magnetic circular dichroism photoemission electron microscopy for different dot sizes under an out-of plane magnetic field 123
5.20 Topological charge phase diagram in a nanodot. 126
5.21 Stabilised magnetic states for a fix spin cycloid length for different domain wall parameters 127
5.22 Stabilised magnetic states with experimental values 129

List of Tables

4.1 Experimental lattice parameters or hcp-Co(0001) and bcc-W(110) found by grazing x-ray diffraction 61
4.2 Spin-wave stiffness measured by Brillouin light scattering in the Damon-Eshbach configuration for $Au_{0.58}Pt_{0.42}$/Co(0.78 nm)/W(110) along t 71
4.3 Experimental anisotropies determined by Brillouin light scatteringin the Damon-Eshbach configuration 74
4.4 Micromagnetic parameters used for the one-dimensional model and simulations calculations 85

5.1 Micromagnetic parameters derived from BLS measurements in $Au_{0.67}Pt_{0.33}$ /Co(0.8nm)/W(110) 105
5.2 Micromagnetic parameters of an elliptical Néel skyrmion 114
5.3 Magnetic parameters extracted from VSM and BLS measurements for $Au_{0.58}Pt_{0.42}$ /Co(0.75nm)/W(110). 120
5.4 Derived domain wall parameter and cycloid length along the two main in-plane axes for $Au_{0.58}Pt_{0.42}$ /Co(0.75nm)/W(110). 128

List of Abbreviations

1D 1-dimensional . . . 25
2D 2-dimensional . . . 30
3D 3-dimensional . . . 55
Bloch DW Bloch domain wall . . . 24
BLS Brillouin light scattering . . . 65
BVW Magnetostatic backward volume waves . . . 65
DE Damon-Eshbach . . . 65
DMI Dzyaloshinskii-Moriya interaction . . . 15
DW domain wall . . . 24
GXRD grazing X-ray diffraction . . . 52
LLG Landau-Lifschitz-Gilbert . . . 19
MOKE magneto-optical Kerr effect . . . 65
MCA magneto-crystalline anisotropy . . . 11
ML monolayer . . . 48
Néel DW Néel domain wall . . . 24
PLD pulsed laser deposition . . . 52
PEEM Photoemission electron microscopy . . . 97
RHEED reflection high energy electron diffraction . . . 52
SHE spin Hall effect . . . 21
SOC spin-orbit coupling . . . 11
SOT spin-orbit torque . . . 21
STM scanning-tunneling microscopy . . . 44

SW spin-waves 65
STT spin-transfer torque 20
UHV ultra-high vacuum 52
VBL vertical Bloch-lines 31
VSM-SQUID vibrating sample magnetometry with superconducting quantum interference devices 71
XMCD X-ray magnetic circular dichroism 96
XMCD-PEEM X-ray magnetic circular dichroism photoemission electron microscopy 98
XRD X-ray diffraction 56

1

Introduction

> "It's the questions we can't answer that teach us the most. They teach us how to think. If you give a man an answer, all he gains is a little fact. But give him a question and he'll look for his own answers."
>
> The Wise Man's Fear

Information storage and handling continuously demands faster, denser, non-volatile and low-power-consuming technologies. In these circumstances, spintronics, which employs both electronic and spin degrees of freedom, has provided some novel concepts to improve the former state of the art. During the last decade, the so-called spin-orbit torque was discovered in systems with structural inversion asymmetry using materials with a larger spin-orbit coupling such as a heavy metal, adjacent to a ferromagnet [1; 2; 3]. This type of torque has been shown to be more efficient in ferromagnetic materials than former technologies such as spin-transfer torque, allowing therefore to have an efficient way of writing and reading information for MRAM memories.

An alternative idea to manipulate information is the so-called racetrack memory, which originally was conceived considering chiral domain walls as information carriers [5]. Here an information bit is no longer localised in an MRAM cell but is mobile in a nanowire consisting of a chain of *up* and *down* domains separated by domain walls. Based on a three dimensional array of nanowires with integrated reading and writing elements, an even higher storage density may be achieved. Alternatively to domain walls, a two-dimensional texture called magnetic skyrmion has been proposed as infor-

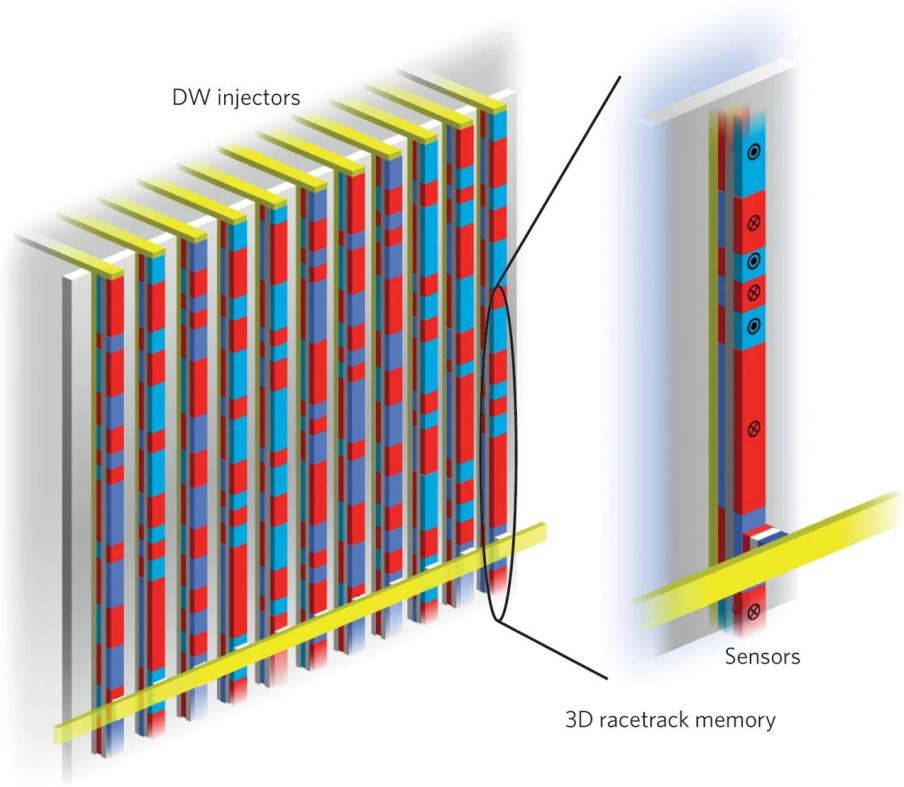

Figure 1.1: **Three dimensional technology: Racetrack Memory 4.0. Red and blue regions represent areas that are oppositely magnetized. Adapted from [4].**

mation carrier instead of domain walls [6]. In simple words, a magnetic skyrmion is a two-dimensional chiral texture with a whirling magnetisation configuration. Their potential nanoscale-size , their expected efficient current-induced displacement by spin-orbit torque, high stability, and the possibility of nucleating and detecting them individually [6; 7; 8; 9; 10; 11] allow to conceive that individual skyrmions could serve as information bits inside storage devices and even inside logic processing units [12]. A foreseen advantage of skyrmions over domain walls is their potentially very small, nanometer scale sizes, which could provide denser memory bits integration.

Independently whether domain walls or skyrmions are considered as information carriers, the key interaction responsible on their stabilisation is the Dzialoshinskii-Moriya interaction, an anti-symmetric exchange interaction which arises in systems without inversion symmetry and a large spin-orbit coupling [13; 14]. This interaction favours a perpendicular alignment of the neighbouring magnetic moments, favouring the formation of non-collinear magnetic textures [15; 16]. The Dzyaloshinskii-Moriya interaction

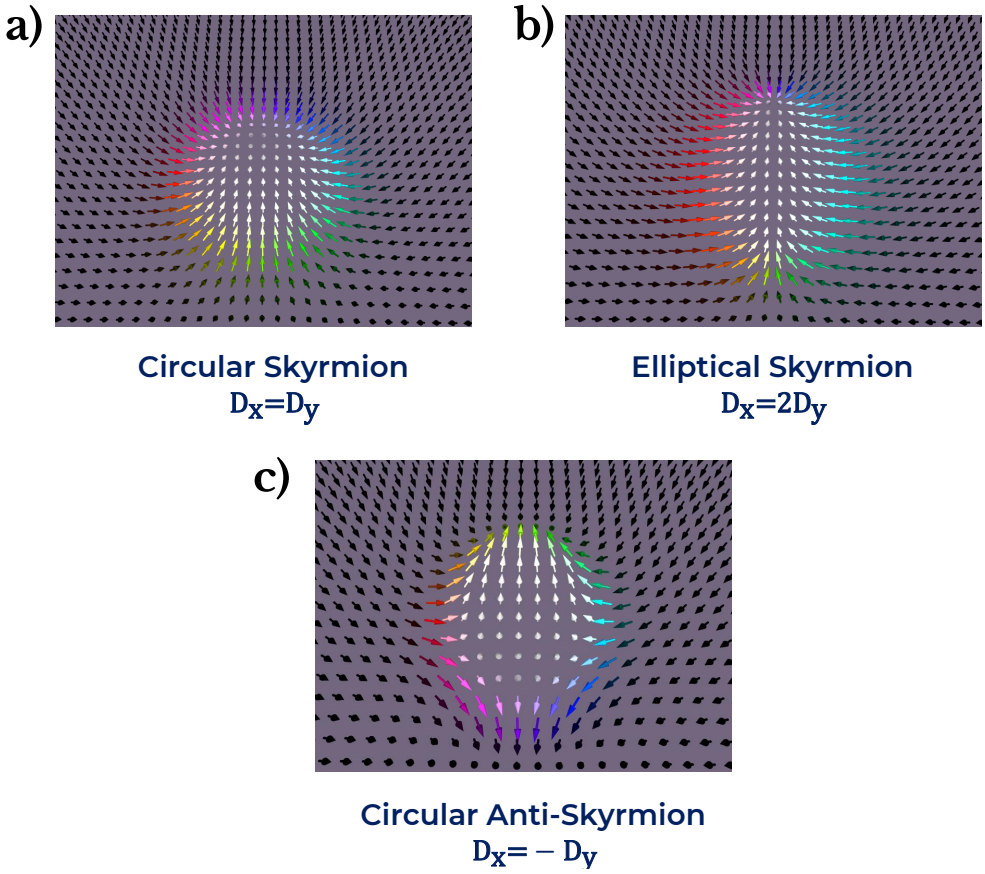

Figure 1.2: **Micromagnetic simulated depending on the Dzyaloshinskii-Moriya interaction strength and sign.**

manifests as a volume interaction in non-centrosymmetric bulk materials and as an interfacial interaction at the interface between magnetic materials and heavy metals.

In thin films with a C_{2v} symmetry, the Dzyaloshinskii-Moriya interaction may be anisotropic in strength, but may also have opposite sign along the two main in-plane directions of the magnetic layer [17; 18; 19], promoting opposite chiral Néel-type rotations along these directions, leading to the so-called antiskyrmion the anti-particle of the magnetic skyrmions [17; 18; 19]. In simple words, a magnetic antiskyrmion is characterised by boundary walls that have alternating Néel configurations with opposite chirality, separated by Bloch configurations as one traces around the boundary. Similarly to magnetic skyrmions, antiskyrmion have been also proposed as promising candidates as information carriers. In this context, figure 1.2 shows the different magnetic configurations that can be stabilised due to an anisotropic Dzyaloshinskii-Moriya

interaction depending on the strength and sign:

- When the sign and the strength are the same, a circular magnetic skyrmion is stabilised (Fig. 1.2 **a)**);
- when the sign is the same but the strength is anisotropic, an elliptical skyrmion is stabilised (Fig. 1.2 **b)**);
- when the Dzyaloshinskii-Moriya interaction sign is opposite, a magnetic antiskyrmion is stabilised. The magnetic antiskyrmion will be circular when the Dzyaloshinskii-Moriya interaction strength is isotropic, and elliptical otherwise (Fig. 1.2 **c)**).

Therefore, depending on the Dzyaloshinskii-Moriya interaction sign and strength, skyrmions or antiskyrmions can be stabilised. Skyrmion and antiskyrmion share the same topological charge, $\mathcal{Q} = \pm 1$ but opposite in sign, for a fixed core direction, due to the opposite vorticity that they have. Experimental evidence of magnetic antiskyrmions have been found in D_{2d} bulk non-centrosymmetric crystals [20; 21; 22], and very recently in S_4 bulk crystals [23]. In thin films, magnetic antiskyrmions may be stabilised in C_{2v} interfaces [17; 18; 19; 24]. While largely studied in theoretical works [19; 25], their observation in thin films is still evasive.

In this thesis, we study cobalt thin films grown epitaxially on tungsten oriented along the (110) plane, showing a two-fold crystal symmetry. This two-fold crystal symmetry results into an anisotropic Dzyaloshinskii-Moriya interaction and a two-fold magnetic anisotropy. These interactions promote an anisotropic energetic environment which results into anisotropic magnetic textures. Therefore, the aim of this thesis is to study the different magnetic textures in the $Au_{1-x}Pt_x/Co(t_{Co})/W(110)$ trilayer, where depending on the thickness and Au-to-Pt composition the strength of the different magnetic interactions can be modulated.

In this manuscript, the $Au_{1-x}Pt_x/Co(t_{Co})/W(110)$ trilayer is studied from a fundamental perspective, aiming to improve the knowledge of anisotropic chiral magnetic textures in thin films with a two-fold symmetry. Hence, the manuscript is divided in four chapters:

Chapter 2. The different energies present in our system is presented. A special emphasis to the Dzyaloshinskii-Moriya interaction and the importance of its symmetry is given.

Chapter 3. We review the main concepts on the statics and dynamics of chiral Néel domain walls combining a one-dimensional model and two-dimensional micro-

magnetic simulations. In addition, we present other two-dimensional textures such as skyrmions, anti-skyrmions and magnetic merons and we discuss briefly under which circumstances they may be stabilised.

Chapter 4. In this chapter we describe the growth process of the $Au_{1-x}Pt_x/Co(t_{Co})/W(110)$ stack as well as its *in-situ* and *ex-situ* structural characterisation. On the other hand, the characterisation of the different magnetic parameters as function of the Au-to-Pt content is determined by Brillouin light scattering. Finally, the field-driven domain wall motion as function of the Pt content is investigated by magneto-optical Kerr effect microscopy in the polar configuration and discussed in terms of the micromagnetic parameters derived by Brillouin light scattering.

Chapter 5. In this chapter we present the different magnetic textures observed in our system by x-ray magnetic circular dichroism photoemission electron microscopy. Three different magnetic textures are observed: stripe domains, elliptical skyrmions and merons. A large discussion for each texture is given, combining analytical models and micromagnetic simulations to explain the experimental findings.

Finally, the main conclusions, the most relevant results and the perspectives for future work are summarised.

2

Magnetism in thin films

Contents

2.1 Principles of micromagnetism **7**
2.2 Energies at play **7**
2.2.1 Heisenberg exchange 8
2.2.2 Zeeman Energy 9
2.2.3 Dipolar Energy 9
2.2.4 Magnetic anisotropy 11
2.2.5 Dzyaloshinskii-Moriya interaction 15
2.2.6 Summary 18
2.3 Characteristic lengths **19**
2.4 Magnetic dynamics **19**
2.4.1 Spin-Transfer Torque 20
2.4.2 Spin-Orbit Torque 21

This chapter provides a brief overview about some basic concepts of magnetism in ultrathin films. Far from being exhaustive, the aim of this chapter is simply to set the bases and the context for the physics behind the stabilised micromagnetic textures, which will be presented in the next chapter.

2.1 | Principles of micromagnetism

Ferromagnetism cannot be explained by classical statistical mechanics, as proved by Niels Bohr in 1911 [26] and Hendrika Johanna van Leeuwen in 1919 [27]. The microscopic description of magnetic systems considers the atomic spins to be the relevant physical entities. On the other hand, the atomic-spin interactions give rise to their measurable macroscopic properties, such as magnetisation.

A mesoscopic approach which lies between microscopic and macroscopic approaches is micromagnetism. Micromagnetism describes the magnetic systems using a continuous approach, on length scales that are too large for a quantum mechanical treatment. This model started with the works of Landau and Lifshitz [28] and Bloch [29]. A rigorous development was made in 1940 by William Fuller Brown Jr [30] which relies on two hypotheses:

1. The spatial variation of any physical quantity (magnetic moments, etc.) is slow with respect the length-scale of interatomic distances.

2. The norm of the magnetisation $\mathbf{M}(\mathbf{r})$ is constant and uniform, M_s, in any homogeneous material.[1]

Therefore, the magnetisation is described as $\mathbf{M}(\mathbf{r}) = M_s\mathbf{m}(\mathbf{r})$ with $|\mathbf{m}| = 1$. The unitary magnetisation $\mathbf{m}(\mathbf{r})$, can be expressed in spherical coordinates,(θ, φ) defined in Fig. 2.1 with $0 \leq \theta \leq \pi$ and $0 \leq \phi < 2\pi$, as $\mathbf{m}(\mathbf{r}) = (\sin\theta\cos\phi, \sin\theta\sin\phi, \cos\theta)$.

2.2 | Energies at play

We consider an ultrathin ferromagnetic film, of thickness t_{FM}. The total magnetic energy of our film is given by:

$$\varepsilon = \varepsilon^i_{\mathrm{EX}} + \varepsilon_{\mathrm{z}} + \varepsilon_{\mathrm{d}} + \varepsilon_{\mathrm{MCA}} + \varepsilon_{\mathrm{DMI}} \tag{2.1}$$

The first term represents the isotropic or Heisenberg exchange, the second term is the Zeeman energy induced by the application of an external magnetic field, the third term is the dipolar energy accounting for the internal dipolar field. The last two terms are the magneto-crystalline anisotropy and the anti-symmetric exchange interaction or Dzyaloshinskii-Moriya interaction, which are relativistic effects, and their symmetry depends on the crystal symmetry.

[1] This assumption is valid when the system is not closed to the transition point where the thermal fluctuations may be neglected, and to length scales where spins behave discretely and no longer continuously.

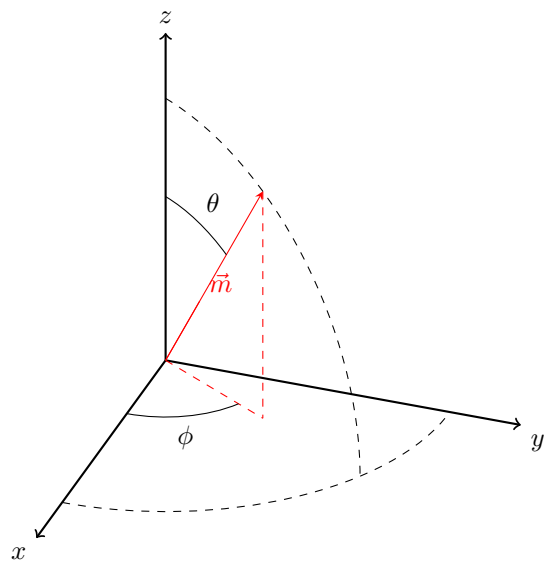

Figure 2.1: **Spherical reference system for magnetisation.**

2.2.1 | Heisenberg exchange

The exchange interaction is a pure quantum phenomenon arising from the Coulomb interaction and the Pauli principle. Considering only the interaction between neighbouring magnetic atoms, this interaction can be described by an effective Heisenberg Hamiltonian:

$$\varepsilon^i_{EX} = -\sum_{i \neq j} J_{ij} \mathbf{S}_i^T \cdot \mathbf{S}_j, \tag{2.2}$$

where J_{ij} is the exchange coupling, whose sign determines the magnetic ordering. A positive (negative) exchange coupling stabilises a ferromagnetic (antiferromagnetic) ordering. In the micromagnetic framework, the exchange energy reads as:

$$\varepsilon^i_{EX} = A \iiint_V (\nabla \mathbf{m})^2 dV, \tag{2.3}$$

$$= A \iiint_V \left[(\nabla\theta)^2 + \sin^2\theta (\nabla\phi)^2 \right] dV, \tag{2.4}$$

where $(\nabla X)^2$ stands for $\left(\frac{\mathrm{d}X}{\mathrm{d}x}\right)^2 + \left(\frac{\mathrm{d}X}{\mathrm{d}y}\right)^2 + \left(\frac{\mathrm{d}X}{\mathrm{d}z}\right)^2$ with $X = \mathbf{m}, \theta, \phi$. Finally, the link between J and A depends on the lattice symmetry, but scales as J/a, with a the interatomic distance. In $3d$ ferromagnets such as Co or Fe, A usually ranges between 5-30 pJ/m. [31; 32].

2.2.2 | Zeeman Energy

The Zeeman energy density is the energy of a magnetic body with magnetisation $\mathbf{M}$ under a uniform external applied magnetic field, $\mu_0\mathbf{H}_{\text{ext}}$ with unit vector $\mathbf{u}_{\text{ext}}$. The Zeeman energy density reads as

$$E_z = \frac{\varepsilon_z}{V} = -\mu_0 M_s H_{\text{ext}} \mathbf{m} \cdot \mathbf{u}_{\text{ext}}, \tag{2.5}$$

where V is the volume of the film.

2.2.3 | Dipolar Energy

The dipolar energy is the result of the mutual Zeeman interaction between all the dipoles of the system. It is the most difficult contribution to evaluate in micromagnetism due to its non-local behaviour. In the micromagnetism framework, the dipolar energy is expressed as:

$$\varepsilon_{\text{d}} = -\frac{\mu_0}{2} \iiint_V \mathbf{M} \cdot \mathbf{H_d} \text{dV}, \tag{2.6}$$

where $\mathbf{H_d}$ is the dipolar or stray field. This expression may be divided into two different contributions: the volume magnetic charges, $\rho = -\nabla \cdot \mathbf{M}(\mathbf{r})$ and the surface charges, $\sigma = \mathbf{M}(\mathbf{r}) \cdot \mathbf{n}$ where $\mathbf{n}$ is the surface normal. The relationship between the dipolar field and the volume and surface charges is given by:

$$\mathbf{H_d}(\mathbf{r}) = \iiint_V \frac{\rho(\mathbf{r}')(\mathbf{r}-\mathbf{r}')}{4\pi|\mathbf{r}-\mathbf{r}'|^3} \text{dV} + \oint_{\partial S} \frac{\sigma(\mathbf{r}')(\mathbf{r}-\mathbf{r}')}{4\pi|\mathbf{r}-\mathbf{r}'|^3} \text{dS}. \tag{2.7}$$

Volume magnetic charges arise whenever the magnetisation is nonuniform; surface magnetic charges arise whenever the magnetisation has a component normal to an external or internal surface. Consequently, to minimise surface charges the magnetisation tends to be parallel to the surface. Finally, Eq. 2.8 may be written in an equivalent form:

$$\varepsilon_{\text{d}} = \frac{\mu_0}{2} \iiint_{\text{Space}} \mathbf{H_d^2} \text{dV}, \tag{2.8}$$

where now the integral is over the all space. From this expression, it is inferred that the dipolar energy is always positive or zero.

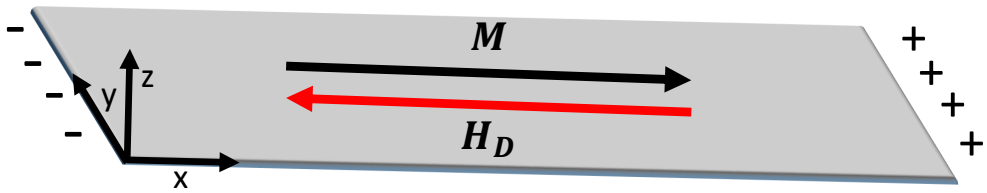

Figure 2.2: **Demagnetising field, inside a uniformly magnetised thin film. M** denotes the magnetisation, $\mathbf{H_D}$ the demagnetising field and the $+/-$ symbols indicate the magnetic surface charges created by the uniform magnetisation. In the case of a thin film, of dimensions $[l, w, t]$, the magnetisation aligns preferentially along the longest direction, as this configuration minimises magnetic surface charges. In this particular case, as $t < w < l$, the magnetisation aligns along the x-axis.

For a uniformly magnetised body only the surface contribution remains, allowing to express the demagnetising energy in terms of demagnetising factors,

$$E_d = K_\mathrm{d} \sum_{i=x,y,z} m_i^T [N_i] m_i, \tag{2.9}$$

$$= K_\mathrm{d}(N_x m_x^2 + N_y m_y^2 + N_z m_z^2), \tag{2.10}$$

where $K_\mathrm{d} = \frac{\mu_0 M_s^2}{2}$ is the dipolar constant and $[N_i]$ is called the demagnetising tensor [33; 34] with $\mathrm{Tr}(N) = 1$ (i.e. $N_x + N_y + N_z = 1$). Note, that in the last step we have taken into account that the demagnetising tensor is a symmetric and positive matrix and therefore it can be be diagonalised. The set of xyz axes upon diagonalisation are called the main or major axes of the system.

Expressing the magnetisation in spherical coordinates, (θ, φ), the demagnetising energy density reads as:

$$E_\mathrm{d} = -K_\mathrm{d}((N_z - N_y)\sin^2\theta + (N_x - N_y)\sin^2\theta\cos^2\phi). \tag{2.11}$$

Let's consider the case of an ultrathin film of dimensions $[x, y, z] = [w, l, t]$, schematically shown in Fig. 2.2. The magnetisation will align preferentially along directions that generates less magnetic charges and minimise the demagnetising energy. Generally, it will try to avoid to be perpendicularly magnetised as it would generate surface

magnetic charges. Therefore, under the absence of perpendicular magnetic anisotropy (see section 2.2.4), the magnetisation will align along the x-axis, as it can be seen easily by inspecting Eq. 2.11, and noticing that in ultra thin films, $N_z \gg N_x, N_y$. Taking this into account, $N_z \approx 1$, leading to the so-called shape anisotropy energy density:

$$E_{\mathrm{d}} = -K_{\mathrm{d}} \sin^2 \theta. \tag{2.12}$$

2.2.4 | Magnetic anisotropy

In real materials, the magnetisation shows a preference to align along specific crystallographic directions. The energy responsible for this tendency is called magneto-crystalline anisotropy (MCA). The MCA is linked to the crystal field, which is the static electric field produced by the surrounding charge distribution of the crystal. Due to the spin-orbit coupling (SOC), the spins prefer to align along certain crystallographic directions that minimise the SOC energy.

Spin-Orbit Coupling

The SOC describes the interaction between the electron spin **S** and the orbital angular momentum, **L**. It is a relativistic effect responsible for many effects in magnetism such as the spin Hall effect, the magneto-crystalline anisotropy [34] or the Dzyaloshinskii-Moriya Interaction [13; 14].

In a semi-classical description the electronic spin is coupled with the magnetic field that the electron feels while it moves around the nuclei (see Fig. 2.3). This orbital movement is coupled directly with the crystal lattice via the electric potential of the ions [33; 35].

The energy associated to the SOC can be calculated, assuming a radial potential, by calculating the Zeeman energy that the spin feels due to the SOC effective field, $\mu_0 \mathbf{H}_{\mathrm{SO}}$:

$$E_{\mathrm{SO}} = -\mu_0 \mu_{\mathrm{s}} \cdot \mathbf{H}_{\mathrm{SO}} = \lambda_{\mathrm{SO}} \mathbf{S} \cdot \mathbf{L}, \tag{2.13}$$

where λ_{SO} is the SOC constant. As shown by Herman and Skillman [36], the λ_{SO} of the outermost electrons which are the relevant electrons in the solid, follows roughly a Z^2 scaling dependence, being Z the atomic number.

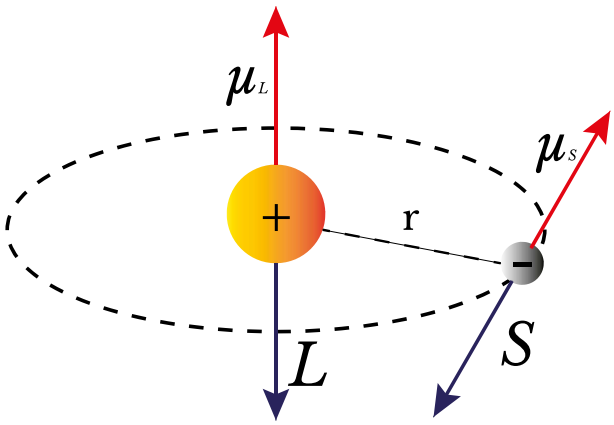

Figure 2.3: **Atomistic spin-orbit coupling.** Classical picture of an atom with the nucleus and the electron orbiting around it. The electron has two different angular momenta: the orbital angular momentum **L** and the spin angular momentum **S**. The two of them result into two different magnetic moments: the orbital magnetic moment μ_L and the spin magnetic moment μ_S.

The simplest form of anisotropy results when the magnetisation has one preferred direction, often called the easy axis. This kind of anisotropy is usually called uniaxial anisotropy, and can be expressed as:

$$E_{MCA} = K_u \sum_i (1 - \mathbf{m_i} \cdot \mathbf{u_i})^2 \tag{2.14}$$

where the MCA constant is represented by K_u. A representation of the MCA energy in three dimensions is shown in Fig. 2.4 when the magnetisation is isotropic (2.4 **a)**), and when it is uniaxial along the z-axis (2.4 **b)**). In the uniaxial case, the energy has a minimum along the z-direction, $\theta = 0, \pi$ and a maximum along the xy-plane, $\theta = \pi/2$ (Fig. 2.4 **c)**).

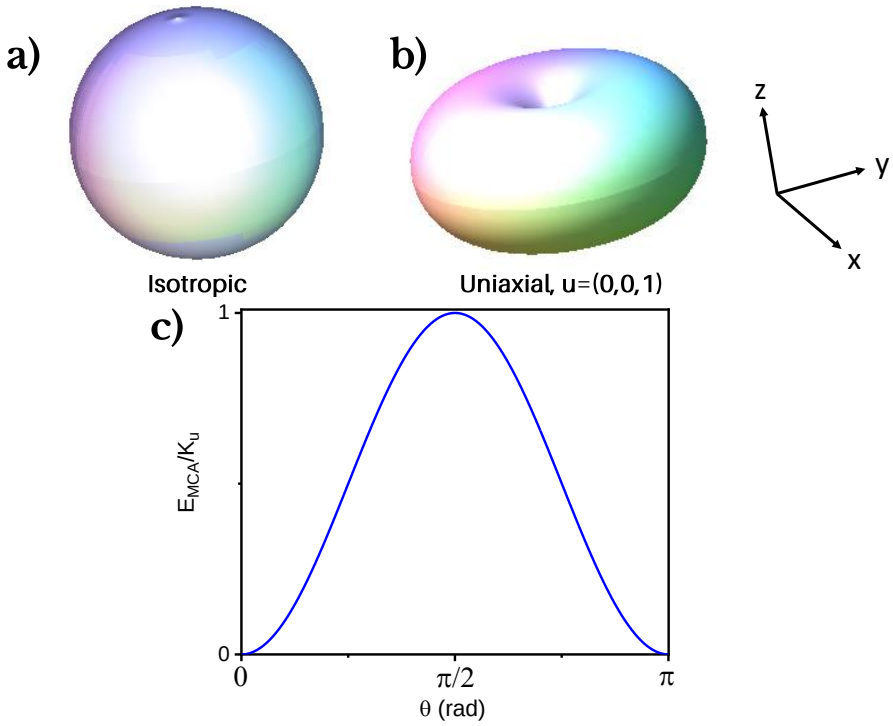

Figure 2.4: **Magnetocrystalline anisotropy energies.** **a)** 3D representation of an isotropic energy: any direction of the magnetisation has the same energy. **b)** 3D representation of a uniaxial anisotropy energy along the z direction. **c)** Magneto-crystalline anisotropy energy per uniaxial anisotropy constant as function of θ for $\mathbf{u} = (0,0,1)$. The energy shows a minimum along the z axis $\theta = 0, \pi$.

2.2.4.1 | Interface-induced anisotropy

In thin films, the broken translation symmetry at an interface produces an additional contribution to the anisotropy known as surface anisotropy [37]. Therefore, the MCA constant can be divided into two components: a volume contribution and a surface contribution [33; 38]:

$$K_u = K_V + \frac{2K_s}{t_{FM}} \tag{2.15}$$

where K_V is the MCA volume anisotropy constant and K_s is the surface anisotropy constant. The factor of two is due to the formation of two surfaces. Typical values of K_s ranges between 0.2 and 0.8 mJ/m^2 [39]. Patrick Bruno suggested a simple physical model that relates the orbital magnetic moment $\mu_L = \mu_B \mathbf{L}$, to the MCA constant per magnetic atom for a uniaxial anisotropy [40]. He showed that the MCA constant increases linearly with the strength of the SOC, λ_{SO}, and with the difference of orbital

magnetic moment between the hard and easy directions, $\Delta\mu_L$. Therefore, a large interface anisotropy is expected for ultrathin films of Co, where $\Delta\mu_L$ is large, deposited on metals with a large atomic number, i.e. with a large spin-orbit coupling constant, λ_{SO} .

In ultrathin films, the volume contributions are mostly due to the demagnetising energy. Consequently, the combination of the MCA and the shape anisotropy, translates into an effective out-of-plane anisotropy between the easy out-of plane axis and the hard in-plane axis:

$$K_{\mathrm{out}} = K_{\mathrm{u}} - K_{\mathrm{d}} = \frac{2K_{\mathrm{s}}}{t_{\mathrm{FM}}} - \frac{\mu_0 M_{\mathrm{s}}^2}{2}. \tag{2.16}$$

According to Eq. 2.16, which is represented in Fig.2.5, we can distinguish three different situations:

- When $K_{\mathrm{out}} < 0$, the MCA overcomes the demagnetising energy, and the magnetisation points out-of plane;
- When $K_{\mathrm{out}} = 0$ the MCA is compensated by the demagnetising energy. The thickness at which this occurs is called critical thickness, $t_{FM,C}$. Typically, $t_{FM,C}$ is about 1 nm;
- When $K_{\mathrm{out}} > 0$, the MCA is overcome by the demagnetising energy, and the magnetisation lies in-plane.

2.2.4.2 | Strain-induced anisotropy

Finally, other anisotropies such as magnetoelastic anisotropy or exchange anisotropy may be present in the system. In this thesis, Co strained ultrathin films are studied, resulting into a strain-induced anisotropy leading to the magnetisation easy-axis pointing along the x-axis. Therefore, the strain-induced anisotropy energy density reads as:

$$E_{\mathrm{Strain}} = -K_{\mathrm{in}} m_x^2 = -K_{\mathrm{in}} \sin^2\theta \cos^2\phi \tag{2.17}$$

Here K_{in} is the in-plane anisotropy constant defined as the difference in energy between the in-plane easy axis (x-axis) and the in-plane hard axis (y-axis).

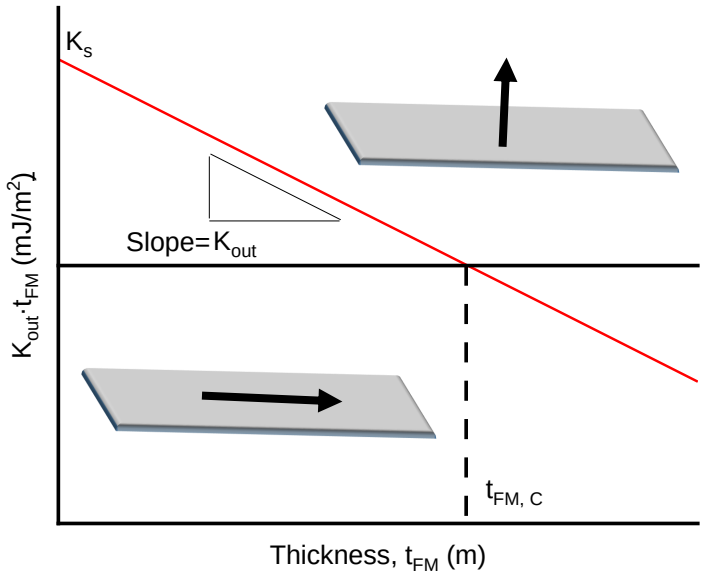

Figure 2.5: **Interfacial anisotropy.** Plot of out-of-plane magnetic anisotropy K_{out} multiplied by the thickness t_{FM} of the ferromagnet as a function of the ferromagnetic thickness. When $K_{\text{out}} > 0$ the magnetisation points out-of-plane, whereas when $K_{\text{out}} < 0$, the magnetisation lies in-plane. The transition from out-of-plane to in-plane occurs at a critical thickness, $t_{FM,C}$ which typically is about 1 nm.

2.2.5 | Dzyaloshinskii-Moriya interaction

The Dzyaloshinskii-Moriya interaction (DMI) is an antisymmetric exchange interaction [13; 14]. In 1958, Dzyaloshinskii proposed that in a crystal with a large SOC and low symmetry, an additional exchange interaction to the Heisenberg exchange results [13] $E_{\text{DMI}} = \mathbf{D}_{ij} \cdot \mathbf{S}_i \times \mathbf{S}_j$, where $\mathbf{D}_{ij}$ is the DMI vector. Two years later, in 1960, Moriya proposed a microscopic model to calculate the antisymmetric exchange interaction in a localised magnetic system, which based on symmetry arguments introduced some constrains that the DMI vector must fulfill. These constrains are known as the so-called *Moriya rules*. Contrary to the Heisenberg exchange interaction, which favours a parallel alignment of neighboring magnetic moments, the DMI favours a perpendicular alignment of the magnetic moments with a preferential rotation, either clockwise or anticlockwise, determined by the DMI vector direction.

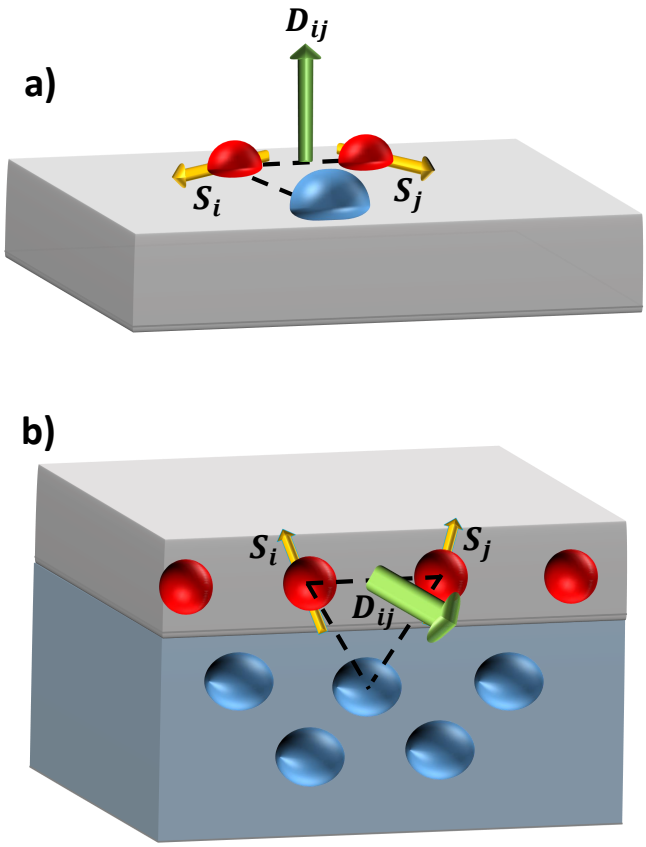

Figure 2.6: **Interface three-site Dzyaloshinskii-Moriya interaction mechanism for ultrathin magnetic films. a)** Sketch of a Dzyaloshinskii-Moriya interaction vector (green arrow) generated due to the 3-site exchange interaction between the magnetic atoms (red) and the non-magnetic atom with large spin-orbit coupling (blue). The yellow arrows represent the magnetic spins. **b)** Sketch of a Dzyaloshinskii-Moriya interaction at the interface between a ferromagnetic layer in gray and a metal in blue with strong spin-orbit coupling. The triangle configuration shown in **a)** is highlighted by the black dashed triangle.

2.2.5.1 | Interfacial Dzyaloshinskii-Moriya interaction

Several theories have been developed to understand the origin of interfacial DMI in ultrathin ferromagnetic films in contact with a heavy metal. Albert Fert and Peter. M. Levy were the first to propose that DMI can occur in magnetic transition metals in the absence of inversion of crystal symmetry owing to the presence of non-magnetic impurities with high spin-orbit coupling [41; 42]. The model considers a 3-site exchange

interaction between the atomic spins and the non-magnetic impurity (Fig. 2.6 **a)**). This 3-site exchange interaction occurs due to the spin-orbit scattering of the conduction electrons by the nonmagnetic impurities [41; 42]. Consequently, the spin-orbit scattering process depends on the spin-orbit interaction strength, which in metals scales with Z^2, and the geometrical distance between the 3 atoms.

Later, Albert Fert extended the Fert-Levy model to the case of the interface between a ferromagnetic thin layer and a metallic layer with a large SOC [42]. This mechanism is illustrated in Fig. 2.6 **b)**. In this case, the 3-site indirect exchange mechanism between two atomic spins (red atoms) with a magnetic moment (yellow arrow) S_1 and S_2 with a neighbouring atom having a large SOC, results into a DMI vector perpendicular to the plane of the triangle (green arrow). Early evidence of this interfacial DMI was obtained from the observation of non-collinear magnetic ordering in the magnetic structure of ultrathin films grown in ultra-high vacuum conditions, and observed at cryogenic temperatures under the application of strong magnetic fields [43; 44; 45; 46].

2.2.5.2 | Dzyaloshinskii-Moriya interaction symmetry

As mentioned above, the relationship between the crystal symmetry and the DMI symmetry was first investigated by Moriya [14] who proposed some rules to determine the constraints imposed on the atomistic DMI vector. Later, Crépieux and Lacroix discussed systematically the vector configurations of the DMI at surfaces of the simple cubic, body centered cubic and face-centered cubic structures [47]. Finally, Bogdanov et al. [48] showed that the micromagnetic DMI energy density could be expressed in terms of first-order spatial derivatives of the magnetisation known as the Lifshitz invariants, which are defined as

$$\mathcal{L}^{\mathrm{i}}_{\mathrm{jk}} = \left[m_{\mathrm{j}} \frac{\partial m_{\mathrm{k}}}{\partial m_{\mathrm{i}}} - m_{\mathrm{k}} \frac{\partial m_{\mathrm{k}}}{\partial m_{\mathrm{i}}} \right]. \tag{2.18}$$

By means of this formalism, it was shown that depending on the crystal symmetry of the noncentrosymmetric crystal or interface, the DMI energy density adopts different forms. For instance, in $B20$ crystals, such as MnSi, FeGe or MnGe the DMI energy is expressed as:

$$\varepsilon_{\mathrm{DMI}} = D \iiint (\mathcal{L}^{\mathrm{x}}_{\mathrm{yz}} + \mathcal{L}^{\mathrm{y}}_{\mathrm{zx}} + \mathcal{L}^{\mathrm{z}}_{\mathrm{xy}}) \mathrm{dV}, \tag{2.19}$$

where D is the micromagnetic DMI. Note than in this case, we are in the situation of an isotropic bulk DMI.

Let's consider the case of C_{nv} $(n \geq 3)$ symmetries. In this case, the DMI energy reads as

$$\varepsilon_{\mathrm{DMI}} = D_s \iint (\mathcal{L}^{\mathrm{x}}_{\mathrm{xz}} + \mathcal{L}^{\mathrm{y}}_{\mathrm{yz}}) \mathrm{dS}, \tag{2.20}$$

Here, $D_s = D \cdot t_{FM}$ is the interfacial DMI constant (in Jm^{-1}) . In this case, the DMI has an interfacial nature, and it is isotropic and isochiral i.e. it keeps the same chirality in the space. This symmetry is typical of Co(0001)/Pt(111) or Co(111)/Au(111) interfaces.

Finally, we consider the case of C_{2v} symmetries. In this case, the DMI energy reads as

$$\varepsilon_{\mathrm{DMI}} = \iint (D^x_{s,xz} \mathcal{L}^x_{xz} + D^y_{s,yz} \mathcal{L}^y_{yz}) \mathrm{dS}, \tag{2.21}$$

$$= \iint (D_{s,x} \mathcal{L}^x_{xz} + D_{s,y} \mathcal{L}^y_{yz}) \mathrm{dS}, \tag{2.22}$$

where we have defined $D^x_{s,xz}$ and $D^y_{s,yz}$ as $D_{s,x}$ and $D_{s,y}$ respectively. Note, that as in the case of C_{3v} symmetries, the DMI has an interfacial origin. The main difference with respect to C_{3v} symmetries relies on the fact that the micromagnetic DMI strength and imposed chirality may be different along the two main in-plane directions of the system x, y. Therefore the DMI may be anisotropic and allow the stabilisation of anisotropic magnetic textures such as elliptical Néel skyrmions or antiskyrmions [17; 18], as we will discuss later. In this manuscript, we will present the study of epitaxial strained Co(0001) ultrathin films deposited on W(110) showing a C_{2v} symmetry. Consequently, the DMI in these systems is described by Eq. 2.22.

2.2.6 | Summary

In summary, the energy density of our strained Co layers with a C_{2v} symmetry, without the application of an external field, is therefore given by:

$$E(\mathbf{m}) = A(\nabla \mathbf{m})^2 + K_{\mathrm{out}}(1 - m_z^2) - (K_{\mathrm{in}} + K_{\mathrm{d}}(N_x - N_y))m_x^2 + D_x \mathcal{L}^x_{xz} + D_y \mathcal{L}^y_{yz}. \tag{2.23}$$

2.3 | Characteristic lengths

Due to the competition between the different magnetic interactions, different characteristic lengths emerge. Characteristic lengths are of special importance in nanomagnetism, determining the size on which specific phenomena occur. Here we will mention only the more relevant:

- Anisotropy exchange length, also named Bloch parameter or domain wall parameter, $\Delta = \sqrt{A/K_u}$. It denotes the relative importance of the exchange energy with respect to the MCA. An ultrathin films of thickness below the exchange length has its magnetisation uniformly aligned along its normal.
- Dipolar exchange length or exchange length: $\Delta_D = \sqrt{A/K_d}$. It describes the relative importance of the exchange energy with respect to the magnetostatic energy.
- Spin cycloid length: $\xi = 2A/D$ which accounts for the balance between the exchange and the DMI energy.

2.4 | Magnetic dynamics

The Landau-Lifschitz-Gilbert (LLG) equation describes the time evolution of the magnetisation. Thereby, the different energies involved in the system are gathered into an effective local field which accounts for all the micromagnetic energies $\mathbf{H_{eff}} = -\frac{1}{\mu_0}\frac{\delta\varepsilon_{\text{Tot}}}{\delta\mathbf{m}}$,

$$\frac{d\mathbf{m}}{dt} = \mu_0\gamma\mathbf{H_{eff}} \times \mathbf{m} + \alpha\mathbf{m} \times \frac{d\mathbf{m}}{dt} + \mathbf{\Gamma}_{\text{others}} \tag{2.24}$$

where α is the damping parameter and $\gamma = g|e|/2m_e$ the gyromagnetic ratio. g is the Landé factor or g-factor[2], e the electron charge and m_e the electron mass. Finally, other torques such as the spin-transfer torque or the spin-orbit torque can be also included.

When the magnetisation and the effective field are not parallel, the system is out of equilibrium. It is then described by two torques (Figure 2.7 **a)**). The first one is a conservative torque describing the precession of the magnetisation around the effective field $\mathbf{H_{eff}}$ (Figure 2.7 **b)**). The angular speed of the precession is proportional to the effective field and the gyromagnetic ratio $\gamma_0 = \gamma\mu_0$. The second term is dissipative and tends to bring the system back to equilibrium. This torque is proportional to the damping parameter and to the temporal variation of the magnetisation. It is perpendicular to the magnetisation and to its trajectory (Figure 2.7 **a)**).

[2] g takes values of 2 for a single electron, but for Co is equal to 2.17

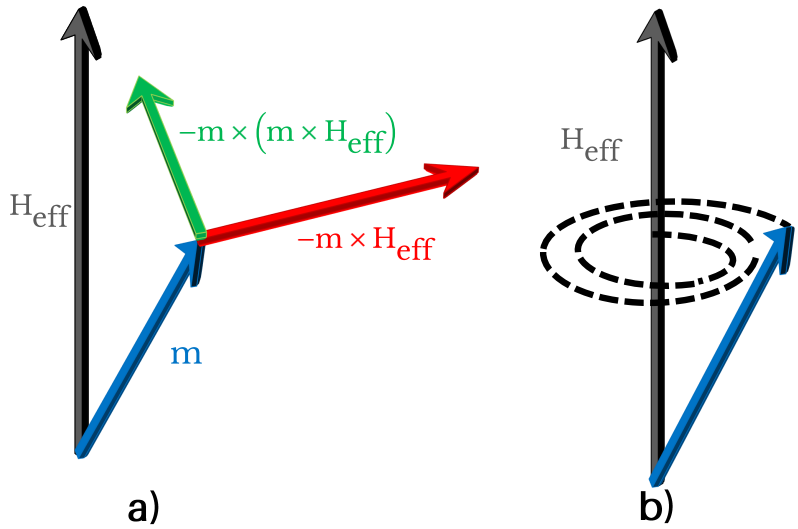

Figure 2.7: **Torques and effective field affecting the magnetisation vector. a)** Torques acting on the magnetisation vector **m** **b)** Damped precession of the magnetisation **m** about the effective field $\mathbf{H}_{\text{eff}}$

2.4.1 | Spin-Transfer Torque

The magnetisation cannot be only modified by an external field but electrical currents can also be used. This effect was firstly predicted theoretically by Berger [49] and Slonczewski [50]. This phenomenon is known as spin-transfer torque (STT) as its mechanism is based on the transfer of angular momentum between the carrier electrons and the local magnetisation. The STT relies on the exchange interaction between the conduction electron spin s and the d electrons, responsible for the local magnetisation **m** [51]. This interaction acts as an effective field, $\mathbf{H}_{\text{sd}}$, which results into two torques: an adiabatic torque due to the spin precession around $\mathbf{H}_{sd}$ and a non-adiabatic torque due to spin-relaxation towards the $\mathbf{H}_{\text{sd}}$ direction.

The STT torques can be included into the LLG equation as shown by Zhang et al. [51], Tatara et al. [52] and Thiaville et al. [15]. Following the formalism proposed by Thiaville et al. [15], the adiabatic and non-adiabatic torques read as:

$$\mathbf{\Gamma}_{\text{Adiabatic}} = -(\mathbf{u} \cdot \nabla) \cdot \mathbf{m} \tag{2.25a}$$

$$\mathbf{\Gamma}_{\text{Non-adiabatic}} = \beta \mathbf{m} \times (\mathbf{u} \cdot \nabla) \cdot \mathbf{m} \tag{2.25b}$$

where $\mathbf{u} = \frac{g\mu_B}{2e}\frac{P}{M_s}\mathbf{J}$ with M_s the spontaneous magnetisation, P the spin-polarisation,

and $\mathbf{J}$ is the current density vector. The spin-drift velocity, $\mathbf{u}$ is a vector directed along the direction of the electron motion. Finally, β is the non-adiabatic factor.

These torques can induce different physical effects among which current-driven domain wall dynamics.

2.4.2 | Spin-Orbit Torque

In the case of STT, the electrical current gets naturally spin-polarised within the magnetic material. In the case of spin-orbit torque (SOT), the spin current is generated by the conversion of orbital angular momentum into spin angular momentum via the SOC, either in the heavy metal layer or at the heavy metal/ferromagnetic interface.

Two main mechanism have been proposed for the generation of this spin-polarised current: the spin Hall effect (SHE) [53; 54; 55] and the Rashba-Edelstein or inverse spin-galvanic effect, usually called just Rashba effect [56; 57; 58; 59] .

The SHE effect is a relativistic effect in which a charge current is transformed into a transverse spin-current due to SOC. When the metal has a large SOC, mostly for large atomic number Z such as Pt, W or Ta, the conducting electrons suffer a spin-dependent scattering process, where up- and down-spins are scattered along opposite directions. This phenomenon leads to an imbalance of the spin population, resulting into a spin-current perpendicular to the electrical charge current. The polarisation of the spin-current will also be perpendicular to the charge current and the spin-current.

The SHE creates a damping-like torque that can be included into the LLG equation by adding the following term

$$\mathbf{\Gamma}_{\mathrm{SHE}} = \gamma_0 \frac{|g|\mu_B}{2e} \frac{\theta_{SHE}}{M_s t_{FM}} [\mathbf{m} \times (\mathbf{m} \times \sigma)] \tag{2.26}$$

Here, t_{FM} is the film thickness and θ_{SHE} is the spin Hall angle defined as the conversion efficiency of the charge-current to spin-current. Finally, σ is the polarisation direction of the spin-current.

Let's consider the following configuration: $\sigma = \mathbf{J_e} \times \mathbf{J_e} = J_c \mathbf{u_y}$. Since the spin polarisation is fixed to the y- direction, the SHE torque will be optimised when the magnetisation points along the z or x-axes. The torque vanishes when the magnetisation points along the y-axis. Within the domain wall framework, the SHE torque will be maximised when the domain wall has Néel-type structure, while it vanishes when the domain wall has a Bloch-type structure.

Finally, the other source of SOT is the Rashba effect which induces a field-like torque which has the form of:

$$\mathbf{\Gamma}_R = \gamma_0 \frac{\alpha_R P}{\mu_0 \mu_B M_s e} [\mathbf{m} \times \boldsymbol{\sigma}] \tag{2.27}$$

where α_R quantifies the strength of the Rashba spin-orbit coupling. Note that if the spin polarised current is along the z-direction, $\boldsymbol{\sigma} = \mathbf{u_y}$, and therefore the Rashba field is equivalent to an effective in-plane field along the y-direction.

To conclude, SOT torques, independently of the mechanism behind its origin, act as an effective in-plane magnetic field whose magnitude scales with the injected current, J_c and an intrinsic mechanism parameter, θ_{SHE} or α_R.

3

Chiral Magnetic textures

Contents

3.1 Domain walls in ultrathin films with perpendicular magnetic anisotropy **24**
- 3.1.1 Introduction 24
- 3.1.2 Statics 25
- 3.1.3 Dynamics 27

3.2 Topology in a nutshell **41**

3.3 Magnetic skyrmions **43**
- 3.3.1 Skyrmion stability 45
- 3.3.2 Skyrmion or skyrmion-bubbles 47

3.4 Magnetic antiskyrmions **47**

3.5 Magnetic meron **49**

This chapter discusses the different magnetic textures that can be stabilised in our system. We focus our discussion mostly on the stabilisation and dynamics of domain walls as well as on the stabilisation of skyrmions. Finally, other magnetic textures such as antiskyrmions and merons will be briefly introduced.

3.1 | Domain walls in ultrathin films with perpendicular magnetic anisotropy

3.1.1 | Introduction

Magnetic domains are regions of a magnetic material where the atomic magnetic moments are oriented on average along the same direction. Magnetic domains result from the necessity to minimise the dipolar energy, which reduces as the number of domains increases, while the other energies such as the exchange or the MCA increase. The small region separating two magnetic domains, is called a domain wall (DW). In perpendicularly magnetised films, for a DW separating upward and downward domains, the magnetisation within the DW rotates in a plane parallel or perpendicular to the DW plane:

- **Bloch domain wall (Bloch DW)** shown in Fig. 3.1 **a)**, the magnetisation rotation occurs in the plane parallel to the DW plane (yz-plane in Fig. 3.1).
- **Néel domain wall (Néel DW)** shown in Fig. 3.1 **b)**, the magnetisation rotation occurs in the plane perpendicular to the DW plane (xz-plane in Fig. 3.1).

As known for many years, the formation of Bloch DWs in perpendicularly magnetised thin films is favoured because of the lower energy cost associated with its dipolar field [60]. More recently, chiral Néel DWs have been predicted in ultrathin films [61] due to the presence of a large interfacial DMI [13; 14]. The first observation of chiral Néel DWs at room temperature was reported by Chen et al.[62] in a Fe/Ni bilayer on

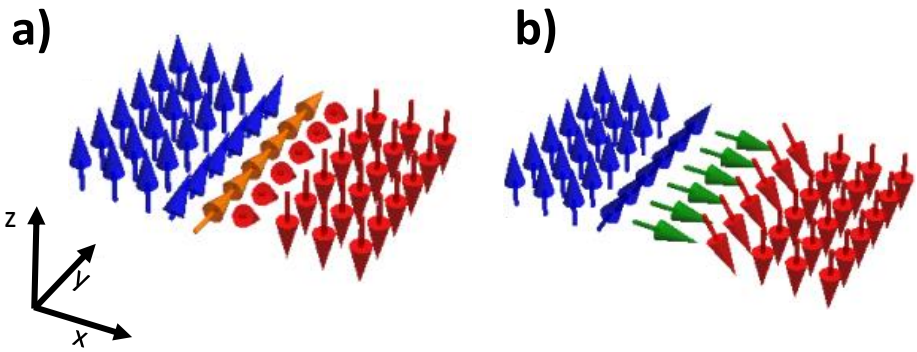

Figure 3.1: **Sketch of domain walls in perpendicularly magnetised thin films.** **a)** Bloch domain wall **b)** Néel domain wall.

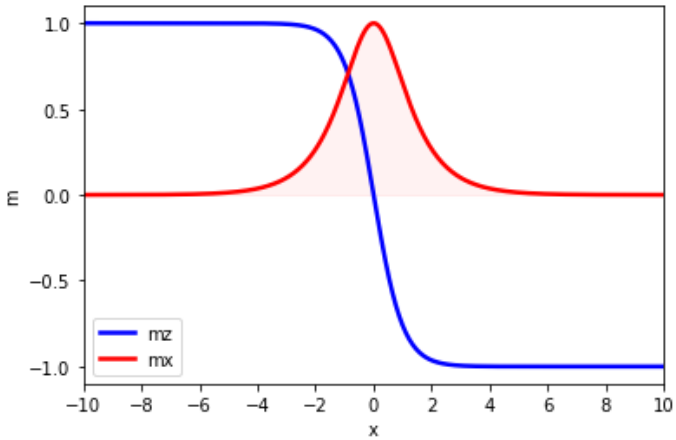

Figure 3.2: **Magnetisation profile of a Néel domain wall**. In blue, $m_z = \cos\theta$ and in red, $m_x = \sin\theta\cos\varphi$ with $\varphi = 0$. The x-axis is in units of Δ. Note that the area under the red curve, $\int \sin\theta(x)$, corresponds with the domain wall width $\pi\Delta$.

Cu[1], in MgO/Co/Pt trilayers by SPINTEC and Institut Néel teams [9] by X-ray magnetic circular dichroism photoemission electron microscopy and in AlO_x/Co/Pt with scanning-nitrogen vacancy magnetometry [63].

In the following, we will review the main concepts on the statics and dynamics of DWs in perpendicular magnetised thin films with C_{3v} symmetry, where the DMI and the MCA interactions are isotropic.

3.1.2 | Statics

A DW is modelled as a 1-dimensional (1D) object whose magnetisation varies uniquely along one direction, which we consider to be the x-axis. The DW energy can be derived by the integration along the x-axis of the energy functional, or energy density, $E(x)$:

$$\sigma_{DW} = \int E(x)\mathrm{dx}, \tag{3.1}$$

$$= \int \left[A\left(\frac{d\theta(x)}{dx}\right)^2 + (K_{\mathrm{out}} + K_{\mathrm{DW}}\cos^2\phi)\sin^2\theta(x) - D\left(\frac{d\theta(x)}{dx}\right)\right]\mathrm{dx}, \tag{3.2}$$

where $K_{\mathrm{DW}} = N_x K_d$ is the DW shape anisotropy constant, with $N_x = \frac{t_{\mathrm{FM}}\ln 2}{\pi\Delta}$ the demagnetising factor of a Néel DW [61; 64], and D the micromagnetic DMI constant. Note that the y-component of the demagnetising field is neglected, which is justified for the assumption that the magnetisation rotates in a vertical plane.

[1] In this case, the main DMI contribution locates at the Fe/Ni interface

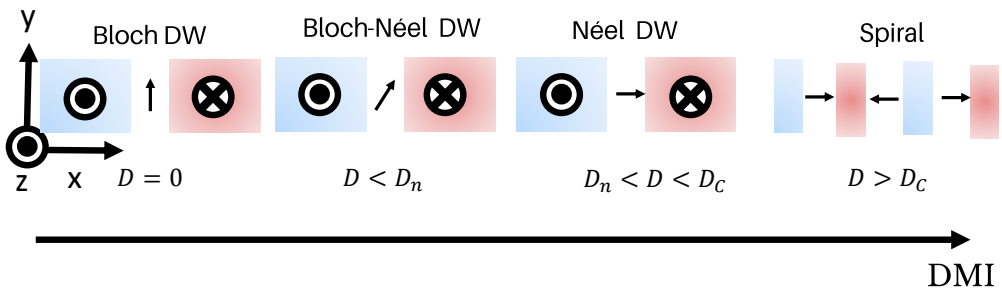

Figure 3.3: **Chiral Néel domain wall in the presence of the Dzyaloshinskii-Moriya interaction** . Evolution of the static domain wall configuration for increasing values of micromagnetic the Dzyaloshinskii-Moriya interaction constant. When $D_N < D < D_c$, a pure chiral Néel domain wall is stabilised. When $D > D_C$ the domain wall energy, Eq. 3.6 becomes negative, and the magnetisation starts to rotate continuously, stabilising a spin spiral.

The magnetisation profile of a DW in a system whose energy density is described by Eq. 3.2 may be found by solving the Euler-Lagrange equations, which leads to the following magnetisation profile [65]:

$$\theta(x,t) = 2\arctan\exp\left(\frac{x-q(t)}{\Delta}\right), \tag{3.3}$$

$$\phi(x,t) = \varphi(t), \tag{3.4}$$

where Δ is the DW parameter, $q(t)$ is the DW position and $\varphi(t)$ is the DW internal angle as sketched in Fig.3.4. The spatial distribution of the unitary magnetisation for a DW is therefore given by $\mathbf{m}(x) = (\sin\theta(x)\cos\varphi_0, \sin\theta(x)\sin\varphi_0, \cos\theta(x))$. The spatial distribution of the unitary magnetisation for a Néel DW, $\varphi_0 = 0$ is shown in Fig. 3.2 using the above magnetisation profile.

The DW energy can be derived by introducing Eq. 3.3 into Eq. 3.2, leading to

$$\sigma_{\mathrm{DW}} = \sigma_0 + \sigma_{\mathrm{DMI}}, \tag{3.5}$$

$$= \frac{2A}{\Delta} + 2\Delta K_{\mathrm{out}} + 2\frac{t_{\mathrm{FM}}\ln 2}{\pi}K_d\cos^2\varphi_0 - \pi D\cos\varphi_0. \tag{3.6}$$

The minimisation of Eq. 3.6 with respect φ_0 and Δ allows to find the static DW parameter:

$$\Delta_0 = \sqrt{\frac{A}{K_{\mathrm{out}}}}. \tag{3.7}$$

The DMI determines the static magnetisation configuration, φ_0 (see Fig. 3.3) as:

$$\cos\varphi_0 = \begin{cases} 1, -1 & \text{if } |D_\mathrm{n}| \leq |D| < |D_\mathrm{c}| \\ \dfrac{D}{D_n} = \dfrac{\pi^2 D}{4K_\mathrm{d} t_\mathrm{FM} \ln 2} & \text{if } |D| < |D_\mathrm{n}| \end{cases} \tag{3.8}$$

Where we have defined $D_\mathrm{n} = \dfrac{4K_\mathrm{d} t_\mathrm{FM} \ln 2}{\pi^2}$ and $D_\mathrm{c} = \dfrac{\sigma_0}{\pi}$. In the absence of DMI, a Bloch DW is stabilised, $\left(\varphi_0 = \pm\dfrac{\pi}{2}\right)$. In order to stabilise a Néel DW, $(\varphi_0 = 0, \pi)$, the DMI needs to be strong enough to compensate the gain in dipolar energy that the Bloch DW constitutes, namely that $D > D_\mathrm{n}$, which is of the order of $0.1\,\mathrm{mJ/m^2}$ in typical ferromagnetic materials. Furthermore, when the DMI is larger than a critical DMI, D_c, the DW energy may become negative, promoting the continuous rotation of the magnetisation, describing a spin spiral whose characteristic length is $\xi = 2A/D$. All these situations are sketched in Fig. 3.3 .

3.1.3 | Dynamics

A DW can be driven to motion either by the application of an external magnetic field along the magnetisation easy-axis, or by spin-polarised currents as already mentioned in section 2.4. A useful tool to describe the DW dynamics either by field or current, is the collective coordinate model which rearranges the LLG equation in terms of collective coordinates. This approach allows reducing the number of degrees of freedom, and helps finding analytical expressions. The main drawback of this approach is that it is necessary to "guess" an analytical expression for the magnetisation profile and the energy density functional.

The LLG equations can be derived following a Lagrangian approach, calculating the Lagrangian and Rayleigh dissipative function [66; 67; 68], which may be derived for a given magnetisation profile and energy functional. The LLG equation can be transformed in terms of the collective coordinates by solving the Euler-Lagrange-Rayleigh equations. For simplicity we will consider only two collective coordinates: the DW position q and the DW internal angle, φ, the so-called $q - \varphi$ model. Note that more complex models such as the (q, φ, Δ) model, accounting for the temporal variation of the DW parameter, or the (q, φ, χ)[69] or the $(q, \varphi, \Delta, \chi)$[70] models, accounting also for the tilting angle of the DW in the plane of the sample χ have been derived. Yet, the $q - \varphi$ model is sufficient to explain the main physical phenomena described in this manuscript.

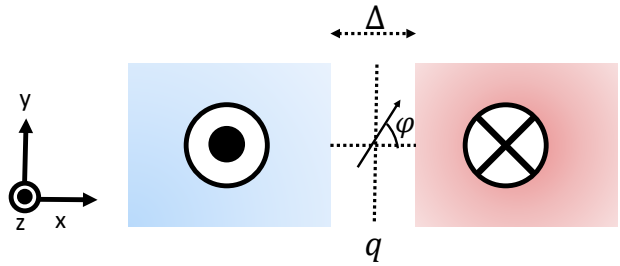

Figure 3.4: **Sketch of the collective coordinates.** The domain wall centre position q, the internal angle φ and the DW parameter, Δ

3.1.3.1 | Magnetic field-driven domain wall motion

We derive the Euler-Lagrange-Rayleigh equations for DW described by equations 3.2 and 3.3. As a driving force, we assume a magnetic field applied along the z-axis direction (the magnetisation easy-axis), $\mu_0 \mathbf{H}_{\text{ext}} = (0, 0, \mu_0 H_z)$ leading to:

$$\alpha \frac{\dot{q}(t)}{\Delta} + \dot{\varphi}(t) = \gamma_0 H_z, \tag{3.9a}$$

$$\frac{\dot{q}(t)}{\Delta} - \alpha \dot{\varphi}(t) = \gamma_0 \sin \varphi(t) \left(\frac{\pi}{2} H_{\text{DMI}} - H_{\text{DW}} \cos \varphi(t) \right). \tag{3.9b}$$

Here, Δ is the DW parameter in static, and $\mu_0 H_{\text{DW}} = \frac{2K_{DW}}{M_s} = \frac{t_{\text{FM}} \ln 2}{\pi \Delta} \mu_0 M_s$ is the shape anisotropy effective field of the DW. Finally, the effective DMI field, which is equivalent to an effective in-plane magnetic field, is given by:

$$\mu_0 H_{\text{DMI}} = \frac{D}{M_s \Delta}. \tag{3.10}$$

Equations 3.9a and 3.9b can be rearranged in a more convenient way:

$$\dot{q}(t) = \frac{\gamma_0 \Delta}{\alpha} H_z - \frac{\Delta}{\alpha} \dot{\varphi}(t), \tag{3.11a}$$

$$\dot{\varphi}(t) = \frac{\gamma_0}{1 + \alpha^2} \left[H_z - \alpha \left(-\frac{H_{\text{DW}}}{2} \sin 2\varphi(t) + \frac{\pi}{2} H_{\text{DMI}} \sin \varphi(t) \right) \right]. \tag{3.11b}$$

At low fields the DW motion shows a linear increase of velocity with field. In this regime, the external field-like torques and the damping-like torques compensate each other, keeping a constant value of φ. This regime of motion is called steady or stationary regime, and the DW velocity is given by:

$$\dot{q} = \frac{\gamma_0 \Delta}{\alpha} H_z \tag{3.12}$$

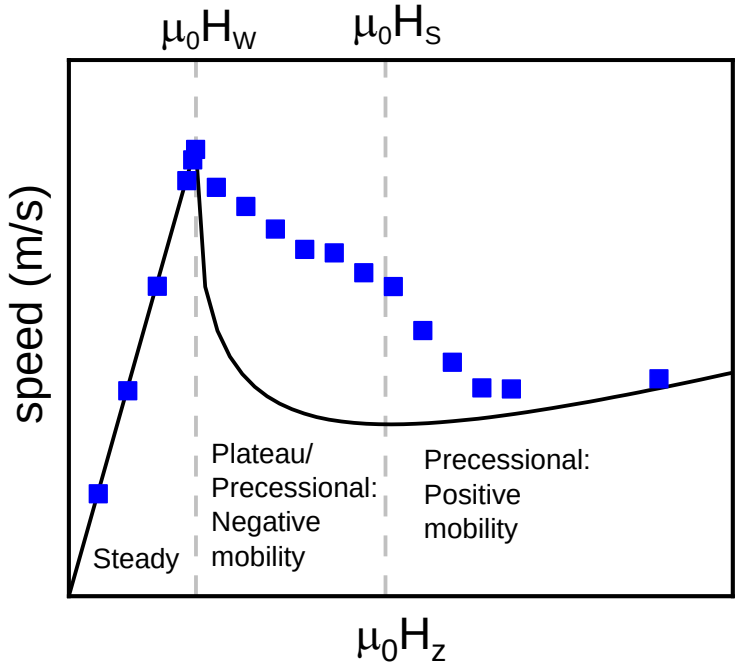

Figure 3.5: **Different regimes of the field-driven Néel domain wall motion in the presence of Dzyaloshinskii-Moriya interaction**. The solid line represents the one-dimensional model, where the different regimes are labelled as well as their characteristic fields (Walker and Slonczewski). The blue dots represent the two-dimensional micromagnetic simulations. Note that in the negative mobility regime, a velocity plateau may appear as it is discussed in the precessional regime section. The magnetic parameters used here correspond to those of a Ta/GdCo/Pt trilayer, as in Ref [71].

Above a threshold field called Walker field, the external field-induced torque cannot be compensated by the damping torque, resulting into the precession of the internal DW magnetic moment, $\dot{\varphi} \neq 0$, and an abrupt drop of the DW velocity. This phenomenon is called the Walker breakdown [72]. In the first stage of the precessional regime, the DW mobility is negative so that a straight DW is unstable [73]. The field $\mu_0 H_S$, named Slonczewski field in honour of J.C.Slonczewski in [71], is the magnetic field where the DW velocity reaches a minimum, the negative mobility regime ends and above which the DW starts precessing with a given period, T. In the asymptotic limit, ($H_z \gg H_W$), the velocity is given by:

$$\dot{q} = \frac{\gamma_0 \Delta}{\alpha^{-1} + \alpha} H_z \tag{3.13}$$

A sketch of the different regimes of the field-driven DW motion predicted by the 1D model and the results of 2-dimensional (2D) micromagnetic simulations are shown in Fig. 3.5. In the following, we are going to describe the DW motion in these different regimes, following the results of Thiaville et al. [61] and our team [71; 74] combining experimental measurements with 2D micromagnetic simulations and the 1D model.

Steady regime

From Eq. 3.11b we can search for stationary solutions, by imposing $\dot{\varphi} = 0$. This allows us to find the Walker field, $\mu_0 H_W$ and velocity, v_W, i.e. the maximum field at which the DW will be driven steadily and the velocity at this field:

$$H_W = \alpha H_D \sin\varphi_W \left(1 - \frac{\cos\varphi_W}{\delta}\right), \tag{3.14a}$$

$$v_W = \gamma_0 \Delta H_D \sin\varphi_W \left(1 - \frac{\cos\varphi_W}{\delta}\right), \tag{3.14b}$$

where $H_D = \frac{\pi}{2} H_{DMI}$, $\delta = \frac{H_D}{H_{DW}}$, and $\cos\varphi_W = \frac{\delta - \sqrt{\delta^2 + 8}}{4}$. Figure 3.6 **a)** shows the normalised $\frac{H_W}{\alpha H_D}$ as function of δ. When $\delta = 0$ i.e. $D = 0$, the Walker field reduces to $H_W = \alpha \frac{H_{DW}}{2}$ as found by Slonczewski in 1972 [73]. On the other hand, for sufficiently large H_D ($\delta > 2$, $\cos\varphi_W \longrightarrow 0$), the Walker field and velocity can be approximated as:

$$\mu_0 H_W \approx \alpha \mu_0 H_D, \tag{3.15a}$$

$$v_W \approx \gamma_0 \Delta H_D = \frac{\pi}{2} \gamma \frac{D}{M_s}. \tag{3.15b}$$

As can be observed, when the DMI field is much larger than the DW shape anisotropy field, the Walker field and velocity increases linearly with H_{DMI}. This approximation is justified in most cases, as the majority of the systems explored by field-driven DW motion are based on Co/Pt heterostructures, which show a very large DMI [75; 76]. Therefore, by the measurement of the Walker velocity, the micromagnetic DMI can be determined, when the spontaneous magnetisation, M_s, is known. This method provides a big advantage with respect to other DW-motion methods to determine the DMI, where many others parameters play a role, giving rise to a big uncertainty in the determined DMI constant. The DMI in several magnetic trilayers has been determined using Eq. 3.15b in the works of Pham et al. [75], Chaves et al. [77] and Ajejas et al. [78] showing a very good agreement with the values derived by Brillouin light scattering.

A more complex situation occurs when the DMI and the DW shape anisotropy are comparable to each other, $0 < \delta < 2$. In this case, Eq. 3.15a makes an underestimation

of H_W leading to errors up to 30% in the calculation of H_W and v_W. This is discussed in a work that we have recently published in *Physical Review B* [74].

Precessional regime

Above the Walker field, the 1D model predicts that the average DW velocity should drop. Yet, it has been observed experimentally that for sufficiently large DMI strength, the DW speed *vs* $\mu_0 H_z$ does not decrease above $\mu_0 H_W$, but a plateau with constant velocity $v \approx v_W$ is observed, its length being proportional to D/M_s (see the micromagnetic simulations shown in Fig. 3.6 **c)**) [71; 75; 79]. The mechanism behind this behaviour is the nucleation and annihilation of 2π vertical Bloch-lines (VBL) [71; 79], making the DW behave as a 2D object rather than a 1D object, as assumed in the 1D model. The microscopic description of this mechanism is outside the scope of this manuscript, and it is extensively discussed in [71; 79]. One of our interesting findings is that the end of the plateau is directly linked to the the Slonczewski field $\mu_0 H_S$, the field at which the DW velocity is minimum in the negative mobility regime.

The starting point to derive the Slonczewski field $\mu_0 H_S$ are Eq. 3.9a and 3.9b. By taking the average over one period of 2π, the average DW velocity reads as:

$$\langle \dot{q} \rangle = \frac{\gamma_0 \Delta}{\alpha} H_z - \frac{\Delta}{\alpha} \frac{2\pi}{T} \quad \text{with} \tag{3.16a}$$

$$T = \frac{1+\alpha^2}{\gamma_0} \int_0^{2\pi} \frac{d\varphi}{H_z - \alpha \sin\varphi \left(H_D - H_{DW} \cos\varphi\right)} \tag{3.16b}$$

$$= \frac{1+\alpha^2}{\gamma_0 \alpha H_D} I_1[h_z] \quad \text{with} \tag{3.16c}$$

$$I_1[h_z] = \int_0^{2\pi} \frac{d\varphi}{h_z - \sin\varphi \left(1 - \frac{\cos\varphi}{\delta}\right)}, \tag{3.16d}$$

where T is the precession period function, which depends on the value of the integral $I_1[h_z]$ which is a function of the variable $h_z = \frac{H_z}{\alpha H_D}$, with δ a parameter. By minimising Eq. 3.16a with respect to H_z, we can find an implicit equation whose solution allows determining $\mu_0 H_S$

$$\frac{1+\alpha^2}{2\pi} = \frac{I_2[h_z]}{I_1[h_z]^2} \quad \text{with} \tag{3.17a}$$

$$I_2[h_z] = \int_0^{2\pi} \frac{d\varphi}{\left[h_z - \sin\varphi \left(1 - \frac{\cos\varphi}{\delta}\right)\right]^2}. \tag{3.17b}$$

The integrals $I_1[h_z]$ and $I_2[h_z]$ are easily evaluated by numerical integration, for all values of their argument, h_z, and parameter δ. Taking into account the value of α,

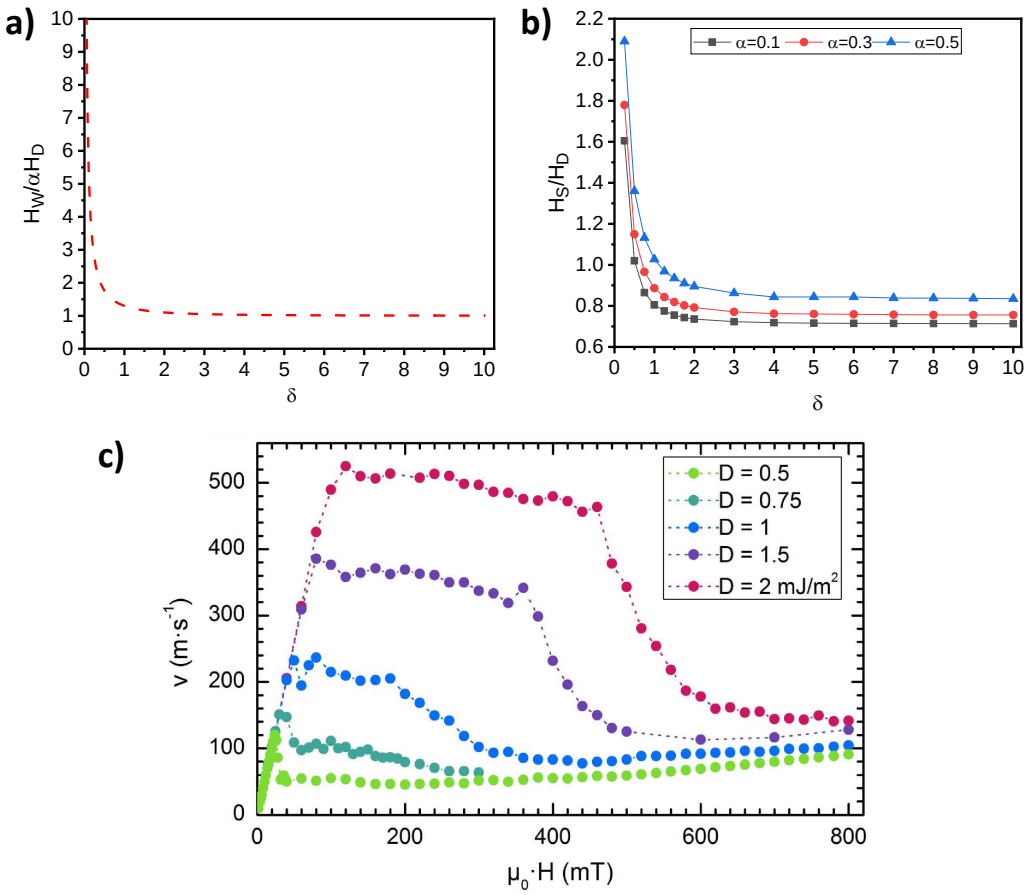

Figure 3.6: **One-dimensional and micromagnetic simulations of the field-driven motion of a Néel domain wall in the presence of the Dzyaloshinskii-Moriya interaction. a)** Calculated $H_W/\alpha H_D$ as function of $\delta = H_D/H_{DW}$ **b)** Calculated H_S/H_D as function of δ for different values of the damping parameter, α. **c)** Micromagnetic simulated field-driven domain wall velocity with M_s=1.01 MAm^{-1} and K_{out}=0.8 MJm^{-3}, and different values of Dzyaloshinskii–Moriya interaction strength. Adapted from [71].

the value of H_S/H_D is found by numerically solving Eq. 3.17a (Fig. 3.6 **b)**), and the Slonczewski velocity, v_S follows by inserting H_S into Eq. 3.16a. It is interesting to note that $\mu_0 H_S$ depends on the damping parameter, but its dependence on δ is similar to the one found for $\mu_0 H_W$ as can be observed inf Fig. 3.6 **a)** and **b)**.

Two limiting cases can be considered: when there is no DMI, and when the DMI is much larger than the DW shape anisotropy. Under these circumstances an analytical expression for T (Eq. 3.16b) may be found [68], and analytical expressions for $\mu_0 H_s$ and

v_s may be derived:

$$H_S = H_W \left(\frac{1+\alpha^2}{\alpha\sqrt{\alpha^2+2}} \right); \tag{3.18}$$

$$v_S = v_W \left(\frac{\alpha\sqrt{\alpha^2+2}}{1+\alpha^2} \right). \tag{3.19}$$

The micromagnetic simulations reported in Fig. 3.6 **c)** show that the length of the velocity plateau (when it exists) increases when the H_{DMI} increases. In these circumstances, the Walker field and velocity may be approximated by Eqs. 3.15a and 3.15b. Consequently, H_S and v_S (Eq. 3.18 and 3.19) are proportional to H_{DMI} and therefore the end of the DW plateau (whose end is correlated with the value of H_s [71]) increases as H_{DMI}. To summarise, by the determination of H_{DMI}, and guessing the value of α, it is possible to estimate the field at which the DW velocity *plateau* starts ($\mu_0 H_W$) and ends ($\mu_0 H_S$), together with its velocity, v_W.

Real or false plateau?

We have shown that the micromagnetic DMI can be measured from the velocity plateau which, due to the 2D effects, keeps the value reached at the Walker field. Therefore, it is tempting to consider that *any* velocity plateau observed in the speed *vs* B_z experimental curves in systems with DMI, corresponds with the velocity plateau occurring after the Walker field. In fact, in our recent work [74] we have shown that this is not always the case. In order to illustrate this, we discuss the experimental results with micromagnetic and 1D analytical model for different stacks. Details on the experimental and micromagnetic simulations are given in Sec. 4.4. We consider four experimental cases:

- Pt/Ta(0.16nm)/Co(0.8nm)/Pt, with $\mu_0 H_{DMI}$ =39 mT, and $\delta = 1.04$
- Pt/Ta(0.32nm)/Co(0.8nm)/Pt, with $\mu_0 H_{DMI}$ =77 mT, and $\delta = 1.94$
- Au/Co(0.8nm)/Pt, with $\mu_0 H_{DMI}$ =198 mT, and $\delta = 4.82$
- Ta/GdCo(4nm)/Pt, with $\mu_0 H_{DMI}$ =90 mT, and $\delta = 5.21$

where the $\mu_0 H_{DMI}$ fields were measured by DW motion driven by a B_z field in the presence of an in-plane field B_x (See Sec. 3.1.3.2).

The experimental speed *vs* B_z curves, measured by magneto-optical Kerr microscopy, are displayed in Fig. 3.7 (blue dots). All the curves show the features expected for a DW motion in the presence of disorder and non-zero temperature. For low fields, the

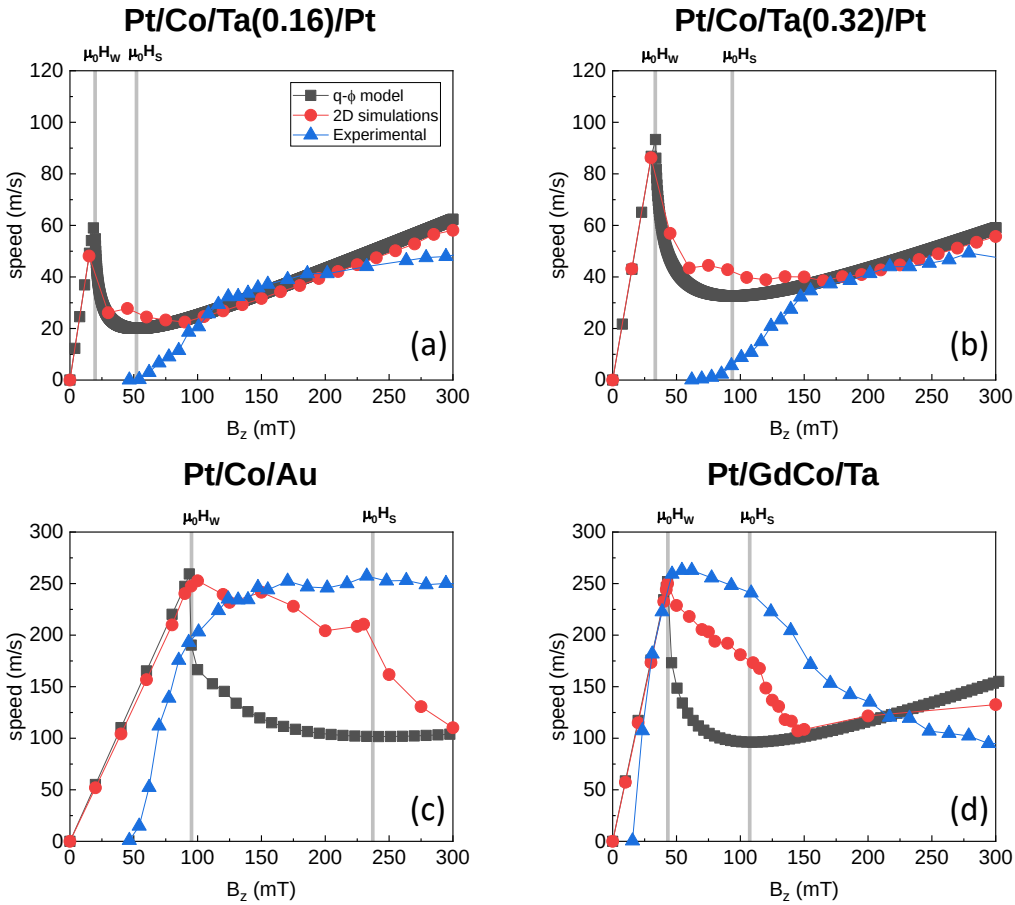

Figure 3.7: **Experimental domain wall speed driven by an out-of-plane magnetic field.** Blue dots represent the experimental speeds, the red dots the micromagnetic simulations, and the black dots, the 1D model. The vertical gray lines represent the exact values of the Walker and Sloncewski field, $\mu_0 H_W$ and $\mu_0 H_S$ respectively. **a)** Pt/Ta(0.16nm)/Co(0.8nm)/Pt; **b)** Pt/Ta(0.32nm)/Co(0.8nm)/Pt; **c)** Au/Co(0.8nm)/Pt; **d)** Ta/GdCo(4nm)/Pt.

DW moves very slowly in the *creep regime*, where the DW speed increases exponentially with the magnetic field, as its motion is very sensitive to disorder and temperature fluctuations, until it enters into the *flow regime*, where the motion is insensitive to defects.

The DW velocities for the two Pt/Co/Ta/Pt samples (see Fig. 3.7 **a)** and **b)**) have similar variations with B_z: a large depinning field of $\sim 100\,\mathrm{mT}$ and a saturating DW speed of $\approx 50\,\mathrm{ms}^{-1}$ for larger magnetic fields. In these stacks, the calculated Walker and Slonczewski fields are much smaller than the measured depinning field. Also, the 1D model and the 2D simulations predict a drop of the DW velocity immediately after

the Walker field. Therefore, the observed DW velocity behaviour for large field cannot be associated to the velocity plateau produced by the 2D effects induced by the DMI. Indeed, the observed velocity corresponds to the precessional regime, as confirmed by the 2D micromagnetic simulations.

The situation is different for the Au/Co/Pt and Ta/GdCo/Pt samples (see Fig. 3.7 **c)** and **d)**, respectively), where the value of H_{DMI} indicates the presence of a large interfacial DMI ($\delta \gg 1$). For Au/Co/Pt, the calculated Walker field (around 90 mT) is much larger than that of the previous samples, but it is situated below the end of the thermally activated regime, so that the steady flow regime is not observable. However, the measured plateau velocity fits remarkably well with the calculated Walker velocity and the micromagnetic simulations, using the measured H_{DMI} field. Yet, in contrast with the 2D simulations, the experimental DW velocity conserves the Walker velocity beyond the calculated Slonczewski field and up to the highest measured fields.

For Pt/GdCo/Ta the velocity curve is different from that observed for the Pt/Co/M stacks: the weaker depinning field, probably due to the larger DW parameter, Δ, allows us to observe the end of the steady flow regime and the Walker field, whose value agrees with the micromagnetic simulations and the 1D model. The velocity stays almost constant after the H_W, before decreasing rapidly above 100 mT. The change of slope of the velocity curve occurs for a field close to the predicted Slonczewski field, and the precessional flow regime is reached around 200 mT. After the Walker field, the measured DW velocity decreases less rapidly than that expected from the 2D simulations.

These results show that the determination of the micromagnetic DMI constant from the plateau velocity needs to be considered carefully as the observed plateau may not be associated to the velocity plateau produced by the 2D effects induced by the DMI.

3.1.3.2 | Magnetic field-driven domain wall motion under an static in-plane field

The application of a static in-plane magnetic field in addition to the out-of-plane magnetic field was proposed by Je et al.[80] and Hrabec et al.[81] as a way to extract the DMI effective field. Yet, their method relies on the application of an out-of-plane magnetic field in the creep regime field window, under an static in-plane magnetic field, which leads to a large uncertainty on the determination of the DMI effective field. These drawbacks may be solved by applying an out-of-plane field in the *flow* regime

working on the [74; 82].

According to the $q - \varphi$ model, the equations of motion under an static in-plane magnetic field are given by:

$$\dot{q}(t) = \frac{\gamma_0 \Delta}{\alpha} H_z - \frac{\Delta}{\alpha} \dot{\varphi}(t), \tag{3.20a}$$

$$\dot{\varphi}(t) = \frac{\gamma_0}{1+\alpha^2} \left[H_z - \alpha \left(-\frac{H_{\mathrm{DW}}}{2} \sin 2\varphi(t) + \frac{\pi}{2} (H_{\mathrm{DMI}} \pm H_x) \sin \varphi(t) \right) \right]. \tag{3.20b}$$

In the precessional regime, the inclusion of an external in-plane field will change Eq. 3.16d by

$$I_1[h_z, h_x] = \int_0^{2\pi} \frac{d\varphi}{h_z - \sin\varphi \left(1 + h_x - \frac{\cos\varphi}{\delta}\right)}, \tag{3.21}$$

where $h_x = \frac{H_x}{H_{\mathrm{DMI}}}$. The minimum velocity will occur when T is minimum which occurs when $\frac{\partial I_1}{\partial h_x} = 0$.

$$\frac{\partial I_1}{\partial h_x} = 2(1+h_x) \int_0^{\pi} \frac{\sin^2\phi}{\left(h_z + \frac{\sin\phi\cos\phi}{\delta}\right)^2 - (\sin\phi(1+h_x))^2} d\phi. \tag{3.22}$$

This expression vanishes when $h_x = -1$, or equivalently, when $H_x = -H_{\mathrm{DMI}}$. Physically, this can be seen as the in-plane field at which the precession is maximum.

Therefore, by measuring the DW minimum velocity, the H_{DMI} field can be measured. This method has been widely used in several works for different systems [75; 77; 80; 81; 83].

3.1.3.3 | Current-induced domain wall motion by spin-transfer torque

As discussed in section 2.4.1, the STT is related to the exchange interaction between the conduction electrons and the local magnetisation. Contrary to the case of field-driven DW dynamics, all the DWs are moved in the same direction. Considering only the

application of current along the x-direction, we find the equations of motion [15; 68; 84]:

$$\dot{q}(t) = \frac{\beta}{\alpha}u - \frac{\Delta}{\alpha}\dot{\varphi}(t) \tag{3.23a}$$

$$\dot{\varphi}(t) = \frac{\alpha}{1+\alpha^2}\left[\frac{u}{\Delta}\frac{|\alpha-\beta|}{\alpha} - \gamma_0\frac{H_{\mathrm{DW}}}{2}\sin 2\varphi(t)\right] \tag{3.23b}$$

where $u = \frac{g\mu_B}{2e}\frac{P}{M_s}J_x$ is the spin-drift velocity (see section 2.4.1).

As in the case of field-driven DW dynamics, two propagation regimes may occur: a steady and a precessional regime. According to the $q-\varphi$ model, the DW velocity and temporal DW magnetisation read as:

$$\dot{q} = \begin{cases} \frac{\beta}{\alpha}u & \text{when } u < u_W \\ \left(\frac{1+\alpha\beta}{1+\alpha^2}\right)u & \text{when } u \gg u_W \end{cases} \qquad \dot{\varphi} = \begin{cases} 0 & \text{when } u < u_W \\ \left(\frac{\beta-\alpha}{1+\alpha^2}\right)\frac{u}{\Delta} & \text{when } u \gg u_W \end{cases} \tag{3.24}$$

where the Walker spin-drift velocity is given by;

$$u_W = \frac{\gamma_0 \Delta H_{\mathrm{DW}}}{2}\frac{\alpha}{|\beta-\alpha|} \tag{3.25}$$

Figure 3.8 shows Eq. 3.24 as a function of the spin-drift velocities for different values of the non-adiabatic torque. The non-adiabatic torque plays an essential role in the DW motion. When the non-adiabatic torque is not present, $\beta = 0$, the DW cannot move below $u_c = \frac{\gamma_0 \Delta H_{\mathrm{DW}}}{2}$, frequently refereed as the critical spin-drift velocity. On the other hand, when the non-adiabatic torque is introduced, the DW is driven steadily for low current densities with a mobility equal to $\frac{\beta}{\alpha}$, until it reaches u_W. Above u_W the DW starts precessing, with a mobility equal to $\frac{1+\alpha\beta}{1+\alpha^2}$, which is weakly dependent on the non-adiabatic torque. A particular case occurs when the non-adiabatic torque completely compensates the adiabatic torque, (see $\beta = \alpha$ in Fig. 3.8), and an infinite steady motion occurs, as the Walker spin-drift velocity is infinite.

In-plane magnetised thin films made of soft magnetic materials such as permalloy $Fe_{20}Ni_{80}$, were widely studied twenty years ago. In such systems, the non-adiabatic torque was necessary in order to explain the experimental velocities measured below the theoretical critical current density [15; 51; 52]. Domain wall dynamics induced by STT in perpendicularly magnetised systems has been rarely studied. Practically no efficient STT motion has been reported in such systems, even if the critical spin-drift

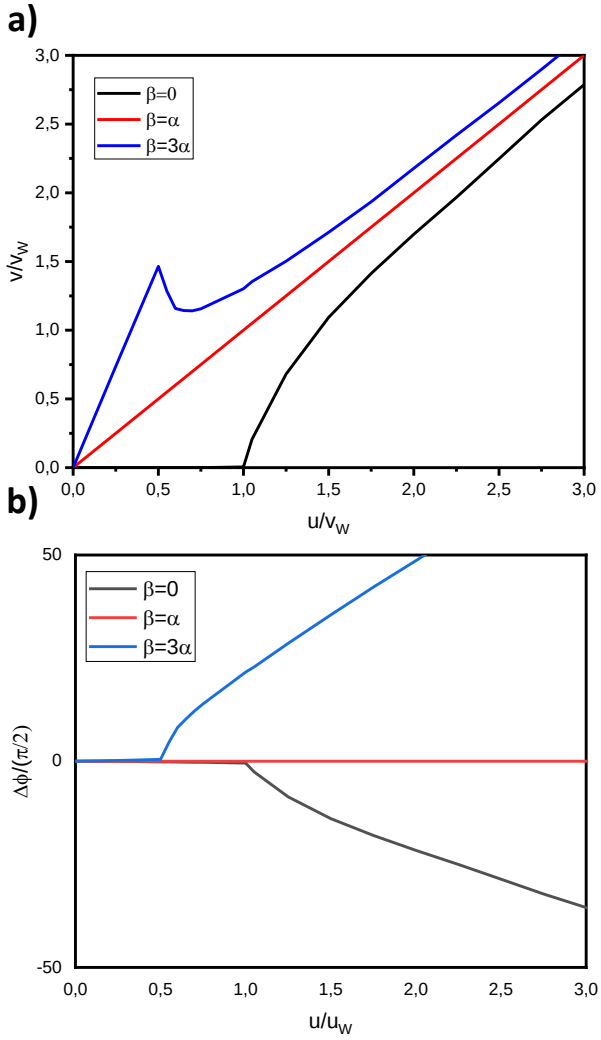

Figure 3.8: **Domain wall dynamics by spin-transfer torque for different non-adiabatic parameters** A a damping parameter $\alpha = 0.1$ is considered. The domain wall and spin-drift velocities are normalised to the Walker threshold velocity $v_W = \gamma_0 \Delta H_{\mathrm{DW}}/2$. **a)** Domain wall velocity **b)** Domain wall internal angle

velocity is lower than in in-plane magnetised films [85]. Furthermore, the discovery of efficient motion of DWs by SOT [1; 2; 86; 87], did not encourage the scientific community to continue exploring STT-current driven DW motion in perpendicularly magnetised films. However, recently very large STT current driven DW velocities have been observed in Mn_4N epitaxial ferrimagnetic thin films, in the framework of a collaboration between SPINTEC and Institut Néel [88]. The Mn_4N layers crystallises in the

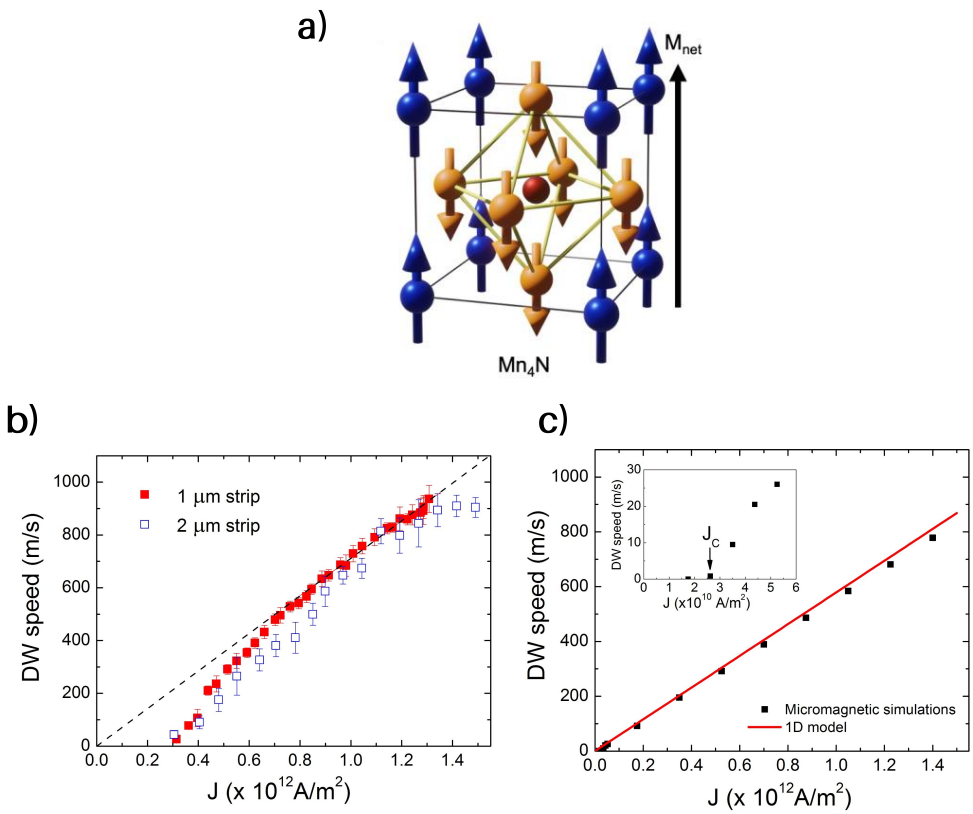

Figure 3.9: **Manganite Nitride spin-transfer torque-domain wall motion**. **a)** Crystal structure of Mn_4N. **b)** Experimental measurements of domain walls driven by STT for two different stripe widths. **c)** Micromagnetic simulations (dots) and 1D model (solid red line).

tetragonal anti-perovskite crystal structure (Fig. 3.9 **a)**), with two types of Mn atoms at the corner (site I) and at the face centred sites (site II) which are antiferromagnetically coupled to each other, resulting into a net magnetisation parallel to the Mn(I) moment. These films show a low magnetisation (around 100 kAm^{-1}) and a relatively high uniaxial perpendicular anisotropy (around 0.1 MJm^{-3}). Due to the absence of DMI, the DW configuration is Bloch, and therefore the motion of the DW is driven by STT along the the electron flow direction.

The experimental curve (Fig. 3.9 **b)**), shows that the DW starts to displace at current densities about fifty times the critical current, estimated to be $J_c \approx 1.1 \cdot 10^{10}$ A/m^2. Therefore, the observed DW linear mobility can be attributed to the precession of the magnetisation within the DW. In this system, the damping parameter is estimated

to be $\alpha = 0.15$, and therefore it can be approximated that the DW velocity is equal to spin drift velocity, u. From the experimental mobility, a polarisation equal to 0.8 may be estimated. With the experimental magnetic parameters the STT-DW motion is reproduced by micromagnetic simulations (Fig. 3.9 **c)**), showing a very good agreement with the experimental results. With this work, we showed that STT can be an efficient way to drive DWs, as long as the system has a reduced spontaneous magnetisation M_s and a large spin polarisation, P.

3.2 | Topology in a nutshell

During the last decade, a part of the scientific community has focused on topological materials. Topology, from the Greek word *topos*, "place" and *logos*, "study", studies the properties of an object under continuous deformations.

In magnetism, 2D textures such as skyrmions or vortices, may have an associated topological charge, also called skyrmion number or just winding number, that is a measure of the local winding of $\mathbf{m}(x, y)$ in the space. Following [89], the topological charge of 2D magnetic textures is given by:

$$\mathcal{Q} = \frac{1}{4\pi} \iint \mathbf{m} \cdot \left(\frac{\partial \mathbf{m}}{\partial x} \times \frac{\partial \mathbf{m}}{\partial y} \right) \mathrm{dxdy}, \tag{3.26}$$

where $\mathbf{m}(x, y)$ is the normalised magnetisation vector, a function of $\mathbb{R}^2$ which evolves in the unit sphere $\mathbb{S}^2$. This expression, may be represented in a more convenient way by making the transformation to polar coordinates (r, Ψ):

$$\mathcal{Q} = \frac{1}{4\pi} \int_{r=0}^{r=\infty} \int_{\Psi=0}^{\Psi=2\pi} \frac{\mathrm{d}\theta}{\mathrm{d}r} \sin\theta \frac{\mathrm{d}\varphi}{\mathrm{d}\Psi} \mathrm{d}r\mathrm{d}\Psi = \mathcal{P} \cdot \mathcal{V}, \tag{3.27}$$

where $\mathcal{P}$ is the polarity and $\mathcal{V}$ the vorticity functions defined as;

$$\mathcal{P} = \frac{[-\cos\theta]_{r=0}^{r=\infty}}{2} = \frac{[m_z(r=0) - m_z(r=\infty)]}{2}, \tag{3.28}$$

$$\mathcal{V} = \frac{[\phi(\Psi)]_{\Psi=0}^{\Psi=2\pi}}{2\pi}. \tag{3.29}$$

It is interesting to study the topological charge associated with different magnetic states. Let's consider first the uniform magnetised state $\mathbf{m}(x, y) = +\mathbf{z}$, which as $\frac{d\theta}{dr} = 0$, has associated $\mathcal{Q} = 0$, which is characteristic of a *trivial topology*. Yet, the skyrmion, which can be described as a small, 2D, circular magnetic domain enclosed by a chiral DW, has associated a $\mathcal{Q} = \pm 1$. A non-zero integer topological charge is characteristic of a *non-trivial topology*. When two magnetic textures have the same topological charge, they belong to the same homotopy class, and they can be converted into each other by continuous transformations. Yet, when they have different topological charge, $\mathcal{Q}$, they belong to different homotopy classes and they cannot be transformed into each other by continuous transformations . For example, a magnetic skyrmion, with $\mathcal{Q} = \pm 1$ cannot be transformed by continuous transformation into the uniform ferromagnetic state, $\mathbf{m}(x, y) = +\mathbf{z}$. This is the recurrently called, *topological protection*. While topology may predict distinct and separate homotopy classes, the magnetisation of physical thin films

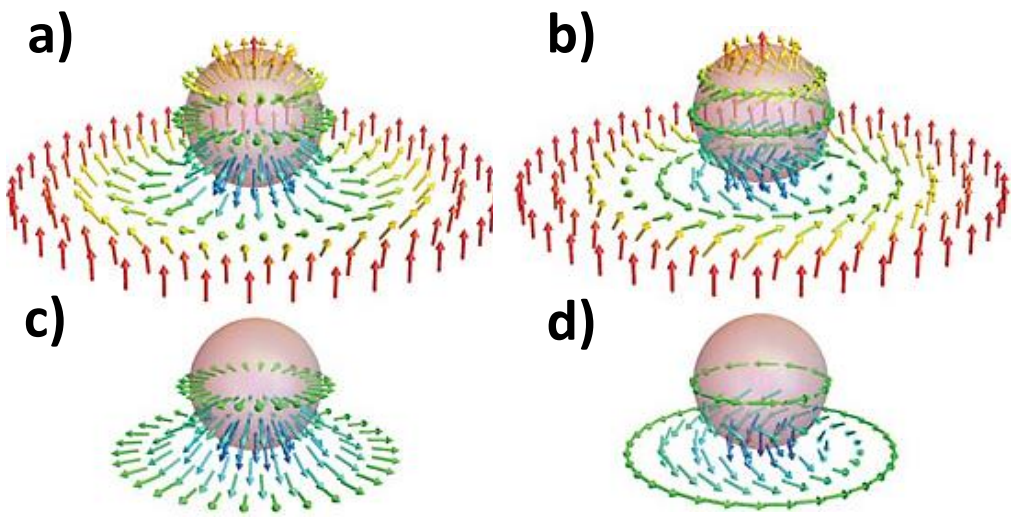

Figure 3.10: **Bloch and Néel-type skyrmions and merons in the real space and their stereographical projection a)** A Néel-type skyrmion in a 2D space and its stereographical projection. Note that the unit sphere is covered once, leading to $\mathcal{Q} = 1$. **b)** A Bloch-type skyrmion in a 2D space and its stereographical projection. Note that the unit sphere is covered once, leading to $\mathcal{Q} = 1$. Configurations **a)** and **b)** are topologicall equivalent. **c)** Néel-type meron, often also described as a radial vortex, corresponds to half a skyrmion which is evident upon stereographic projection. **d)** A Bloch-type meron is topologically equivalent to the hedgehog-type meron shown in **c)**. Adapted from [90].

.

is determined by a discrete lattice of atoms, breaking, therefore the assumption of continuity necessary for topology. Consequently, the predicted *topological protection* is not observed, and for example, a skyrmion with unity topological charge can be injected into the uniformly magnetised configuration. Nevertheless, the tools of topology still remain useful for the classification of the different magnetic textures presented hereafter.

3.3 | Magnetic skyrmions

A skyrmion is a concept originally proposed in particle physics half a century ago by the physicist Tony Skyrme [91]. In magnetism, skyrmions are localised, swirling arrangements of the spin texture [24; 92; 93]. As shown in Fig. 3.10 **a)** and **b)**, the stereographical projection of the magnetic skyrmion, no matter its type, covers completely the unit sphere, giving rise to a topological charge $\mathcal{Q} = \pm 1$, and therefore, its homotopy class is non-trivial. Its unique topological properties and (potentially) very small size confer them particle-like properties [6; 11; 89].

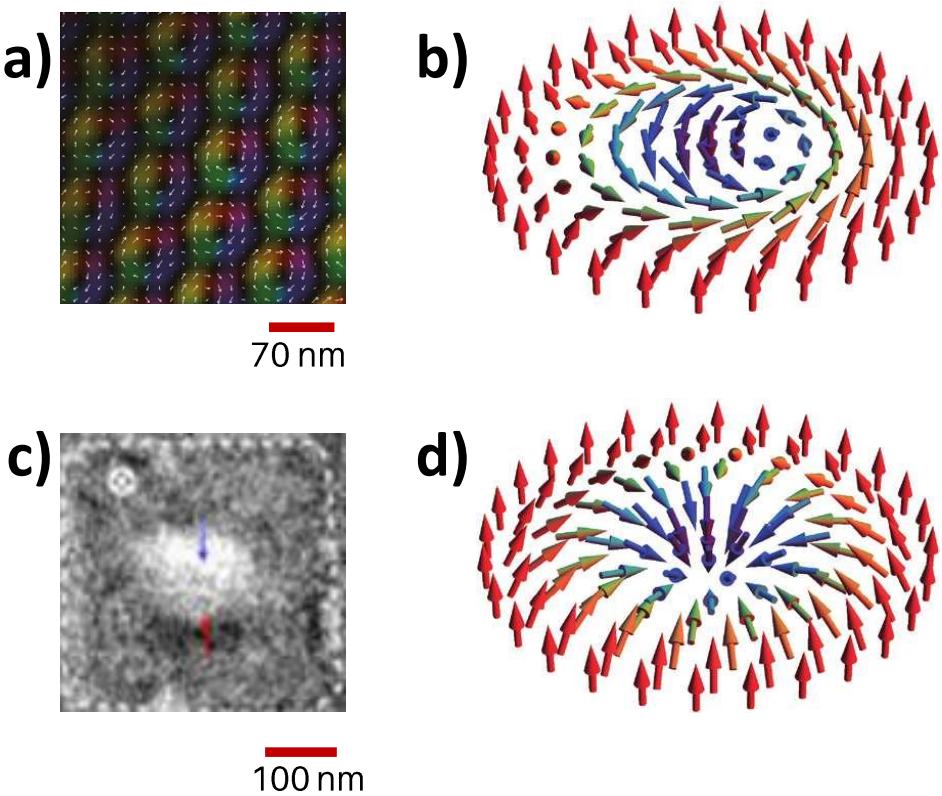

Figure 3.11: **Experimental observation of Bloch-type and Néel-type skyrmion**. **a)** Bloch-type skyrmion lattice in a 50 nm thick FeGe crystal ($\mu_0 H_z = 0.1$ T, 260 K) observed by Lorentz transmission electron microscopy. The white arrows represent the in-plane magnetisation direction. From [94] **b)** Artistic sketch of a Bloch-type skyrmion **c)** Néel-type skyrmion in a square nanostructure by X-ray magnetic circular dichroism photoemission electron microscopy in MgO/Co/Pt. Red and blue arrows, represent the in-plane component of the magnetisation parallel to the X-ray beam. From [9] **d)** Artistic sketch of a Néel-type skyrmion

Their potential nanoscale size and their predicted dynamics properties [11; 89; 95], have made skyrmions strong candidates for electronic devices. The field of skyrmion-electronics mainly focuses on the design and development of information storage and processing devices [96; 97; 98; 99]. The most highlighted skyrmionic device, is the so-called skyrmionic racetrack memory [6] proposed by Fert et al. in 2013, as an adaptation of the DW-racetrack memory proposed by Parkin et al. in 2008 [5]. Other devices such as logical-devices [12; 100] or even for neuromorphic computing [101; 102] have also been proposed.

Magnetic skyrmions may be Bloch-type (Fig. 3.11 **b)**) or Néel-type (Fig. 3.11 **d)**). The skyrmion-type is determined by the DMI symmetry as discussed previously (see section 2.2.5.2). In non-centrosymmetric crystals, where the DMI has a bulk origin, the DMI promotes a Bloch-type rotation, stabilising therefore Bloch-type skyrmions. On the other hand, in interfacial-DMI systems the magnetisation evolves following a Néel-type rotation, and therefore, the skyrmions are Néel-type.

Magnetic skyrmions were first observed in bulk non-centrosymmetric single-crystals [94; 103; 104; 105]. These single crystals, very often just called *B20* crystals, are a specific family of non-centrosymmetric single-crystals belonging to the $P2_13$ space group. These skyrmions were found to exist in the form of a Bloch-type skyrmion in a hexagonal lattice, observed in the presence of an external magnetic field at cryogenic temperatures (Fig. 3.11 **a)**). The first observation of Néel-type skyrmions, was reported in an epitaxial ultrathin layer of Fe(110) grown on Ir(111) using spin-polarised scanning-tunneling microscopy (STM) at cryogenic temperatures[106]. In addition, sub-10 nm skyrmions were observed by spin-polarised STM under a large magnetic field and at cryogenic temperatures, as the system was paramagnetic at room temperature. The major breakthrough occurred when the successful stabilisation of isolated magnetic Néel-type skyrmions, in the following called just skyrmions, was achieved. This took place in 2016, when magnetic skyrmions were observed in sputtered non-magnetic/ferromagnet ($\approx$ 1nm)/heavy metal stacks with perpendicular magnetic anisotropy and an interfacial isotropic DMI [2] promoting chiral Néel DWs. Among these systems we may mention MgO/Co/Pt trilayers [9], where skyrmions were stabilised in nanostructures without the application of an external field, or in Pt-based multilayers such as $[Ta/Co/Pt]_{15}$ [107], $[MgO/CoFeB/Pt]_{15}$ [107], or $[Pt/Co/Ir]_{10}$ [10], where skyrmions were stabilised under a weak external field. These observations were achieved using a synchrotron radiation technique sensitive to the magnetisation direction namely scanning X-ray transmission microscopy or X-ray magnetic circular dichroism photoemission electron mi-

[2] These stacks present a C_{3v} crystal symmetry

croscopy [9]. From then on, skyrmions have been observed in a wide variety of systems and using very different techniques such as Lorentz transmission electron microscopy, Kerr microscopy, magnetic force microscopy or nitrogen vacancy microscopy.

A magnetic skyrmions is uniquely characterised by its vorticity and its size. While the skyrmion vorticity depends on the DMI sign, which depends on the DMI vector, the skyrmion size depends on the balance between the different energy terms in the system. Therefore, skyrmion sizes ranging from few nanometers to few microns have been observed.

3.3.1 | Skyrmion stability

The starting point for the study of the skyrmion stability and size, is expressing the skyrmion energy, which due to the cylindrical axial symmetry is expressed in cylindrical coordinates [3]. :

$$\begin{aligned}\varepsilon_{\text{Sky}}(r) = 2\pi t_{\text{FM}} \int_{r=0}^{r=\infty} \text{rdr}A \left[\left(\frac{d\theta}{dr} \right)^2 + \frac{\sin^2\theta}{r^2} \right] \\ + D \left[\frac{d\theta}{dr} + \frac{\sin 2\theta}{2r} \cos\varphi \right] + K_{\text{out}} \sin^2\theta - \mu_0 M_s B_z \cos\theta + E_{\text{demag}}^{\text{long range}}.\end{aligned} \tag{3.30}$$

The minimisation of Eq. 3.30 allows finding the skyrmion profile and radius. This has been already performed by assuming an initial skyrmion profile. Yet, the most challenging and complex part is the calculation of the long range demagnetising energy due to its non-local behaviour. The solutions to this model have been performed by computing the long range dipolar interactions with different approaches [7; 8; 108]. Two main types of axially symmetric solutions exist in systems with interfacial DMI: what is usually referred as the skyrmion and the skyrmion-bubble solution. In order to illustrate this, we consider the model developed by Bernand-Mantel et al. [7], where the skyrmion energy is expressed analytically as a function of the skyrmion radius, R as:

$$\varepsilon_{\text{Sky}}(R) = \frac{E_0 \pi \Delta}{2R + \pi\Delta} + \sigma_{DW} 2\pi R t_{\text{FM}} + 2\pi M_s \mu_0 H_z R^2 t_{\text{FM}} - 2\pi \mu_0 M_s^2 R t_{FM}^2 I(d), \tag{3.31}$$

where $I(d)$ is a function in terms of complete elliptic integrals of the first and second kind, with $d = \frac{2R}{t_{\text{FM}}}$. The first term is the non-linear exchange energy with $E_0 = 8\pi A t_{\text{FM}}$. the zero-radius limit for the exchange energy [109]. The second term is the DW energy,

[3] Therefore, the discussion is limited to circular skyrmions and not elliptical

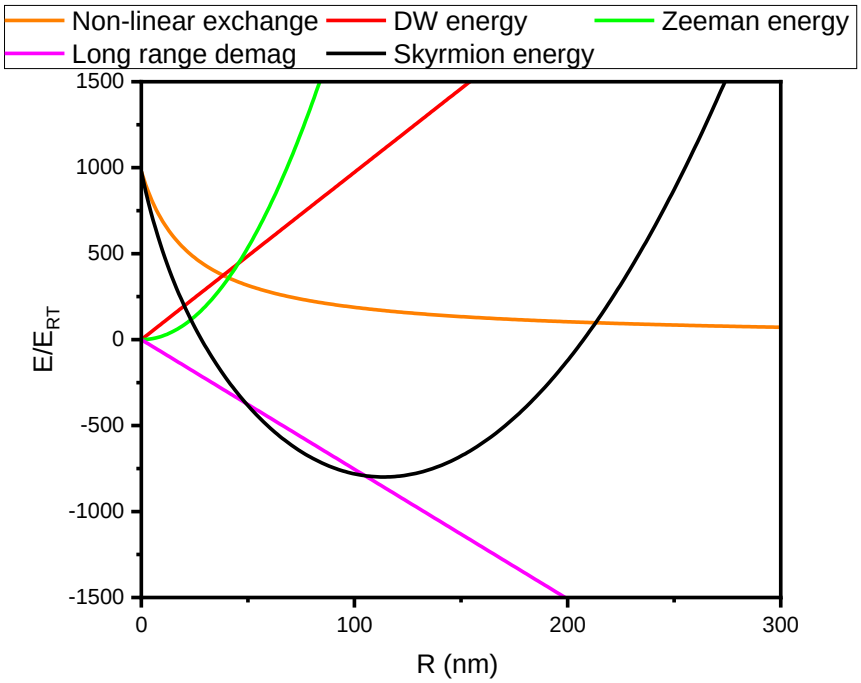

Figure 3.12: **Magnetic skyrmion energies variation** . All the different energies discussed in Eq. 3.31 using the values given in the main text, and normalised to the room-temperature thermal energy $k_B T$. Note that an Skyrmion bubble solution of radius 110 nm is found.

which includes the linear exchange, out-of-plane anisotropy and the DMI energy. The third term is the Zeeman energy, and the last term is the long-range demagnetising energy. The variation of these energies as function of the skyrmion radius is shown in Fig. 3.11 for experimental values: σ_{DW} =0.24 mJ/m^2, $\mu_0 H_z$ =10 mT, M_s =1.15 MA/m, t_{FM} =1 nm, A =16 pJ/m, and Δ =15 nm. From Eq. 3.31 it can be concluded the following:

1. In the absence of DMI, no stable skyrmion solution is found.

2. When only the shape anisotropy is considered, scaling all the intrinsic magnetic parameters by a unique factor, multiplies the skyrmion energy by the same factor, but not its size.

3. In the low radius range, a non-linear contribution on the exchange interaction is present due to the large curvature of the skyrmion in this range.

4. Large skyrmions, with $r_{Sk} \gg \pi\Delta$, are only formed when the wall energy cost is lower than the energy gain due to long range demagnetising effect.

3.3.2 | Skyrmion or skyrmion-bubbles

According to the model of Bernand-Mantel et al. [7] two different solutions may be possible:

- **Skyrmion.** In the low radius range, $r < \pi\Delta$, the non-linear variation of the exchange energy, due to the curvature, and the linear variation of the DMI with the skyrmion radius stabilises a skyrmion (also called DMI-skyrmions). Its radius increases with D and it can be stabilised without the application of an external magnetic field. Due to their small size, DMI-skyrmions are insensitive to an external magnetic field.

- **Skyrmion bubble.** In the long radius range, $r \gg \pi\Delta$, the non-linear variation of the exchange energy is negligible. In this range, when the DW energy cost is lower than the gain given by the long range demagnetising energy, under the application of an external magnetic field, a second solution can be stabilised. Consequently, in presence of a magnetic field, two solutions are observed separated by a local maximum of energy. The lower radius solution is the DMI-skyrmion solution described before. The second solution presents the characteristics of what is usually described as a magnetic bubble: under an increasing magnetic field, it will collapse, but its size diverges when the field is zero. The local maximum of energy creates an energy barrier which is at the origin of eight-shape magnetic hysteresis loops of bubbles [65].

3.4 | Magnetic antiskyrmions

The antiskyrmion is a quasi 2D magnetic texture and it is the anti-quasiparticle of the skyrmion. Antiskyrmions also show a $\mathcal{Q} = \pm 1$, but with an opposite vorticity, $\mathcal{V}$. Therefore, given a skyrmion and antiskyrmion with the same polarity, $\mathcal{P}$, their topological charge $\mathcal{Q}$ will be opposite.

Antiskyrmions are characterised by boundary walls that have alternating Néel configurations with opposite chirality, separated by Bloch configurations as one traces around the boundary. Therefore, in order to stabilise an antiskyrmion, a DMI with opposite sign along the two main in-plane axis of the systems is necessary.

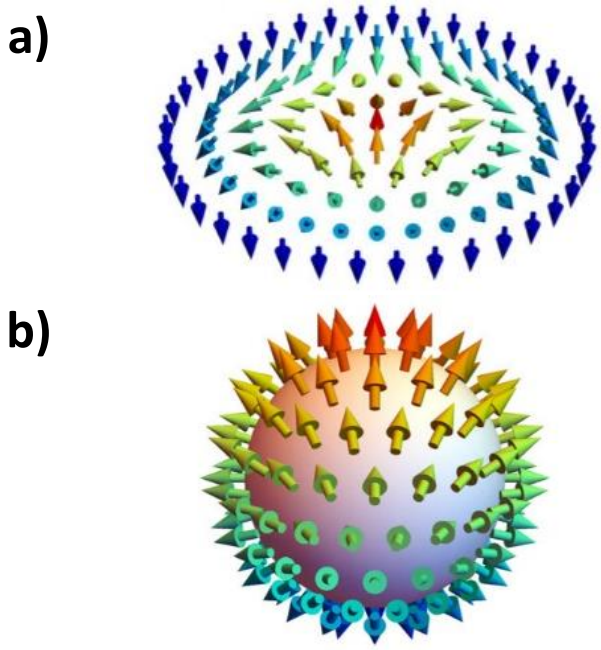

Figure 3.13: **Magnetic antiskyrmion**. **a)** Magnetic antiskyrmion distribution **b)** Stereographical projection of the antiskyrmion shown in **a)**. Note that the unit sphere is covered completely, i.e. $\mathcal{Q} = 1$. From [25]

Magnetic antiskyrmions are predicted to be stable in D_{2d} and S_4 non-centrosymmetric crystals [24]. Experimental evidence of magnetic antiskyrmions have been found in D_{2d} bulk non-centrosymmetric crystals [20; 21; 22], and very recently in S_4 bulk crystals [23]. In thin films, magnetic antiskyrmions may be stabilised in C_{2v} interfaces[17; 18; 19; 24]. While largely studied in theoretical works [19; 25], their observation in thin films is still evasive. The biggest challenge for their stabilisation, relies on finding an interfacial DMI with opposite sign. Theoretically, (2 monolayer (ML)) Fe(110)/W(110) has been predicted to host antiskyrmions [17]. Yet, experimentally this system has not been found to show a perpendicular magnetisation.

Overall, the need for a ferromagnet/heavy metal bilayer with $C_{2\mathrm{v}}$ symmetry and the proper symmetry of DMI, in addition to the perpendicular magnetisation at room temperature, make extremely challenging the stabilisation of antiskyrmions in thin films.

3.5 | Magnetic meron

Magnetic merons are half-skyrmions, in which the magnetic moments in the core region point upwards or downwards, and those near the perimeter align in-plane. As in the case of skyrmions, Bloch-type (Fig. 3.10 **c)**) and Néel-type (Fig. 3.10 **d)**) merons can be stabilised. Bloch-type merons are in fact the traditional vortex structures, stabilised in in-plane magnetised thin films. The transformation from a Bloch-type meron to a Bloch-type skyrmion was achieved recently in bulk materials of the chiral-lattice magnet $Co_8Zn_9Mn_3$ [110].

Néel-type merons show a radial magnetisation distribution, that was already predicted by Rohart et al. [16] in circular nanodots. A more detailed discussion will be given in Chapter 5.4

4

Growth and characterisation: $Au_{1-x}Pt_x$/Co/W(110)

Contents

4.1 Overview of the ultra-high vacuum system and the structural characterisation . . . **52**

4.2 Growth of $Au_{1-x}Pt_x$/Co(t_{Co})/W(110) stack . . . **53**

4.2.1 Growth procedure . . . 53

4.2.2 Sapphire substrate . . . 53

4.2.3 Tungsten . . . 55

4.2.4 Cobalt . . . 57

4.2.5 Gold and platinum . . . 62

4.2.6 Summary . . . 64

4.3 Magnetic characterisation . . . **65**

4.3.1 BLS introduction . . . 65

4.3.2 C_{2v} DMI symmetry . . . 68

4.3.3 Spontaneous magnetisation . . . 71

4.3.4 Magnetic exchange . . . 71

4.3.5 Magnetic anisotropy . . . 72

4.3.6 Néel-type DMI . . . 78

4.3.7 Bloch-type DMI . . . 82

4.3.8 Summary . . . 83

4.4 Field-driven domain-wall motion . . . **85**

4.4.1 Introduction . . . 85

4.4.2 Experiments: DW vs B_z 86
4.4.3 DW motion vs B_z with B_x 92
4.4.4 Summary 94

4.1 | Overview of the ultra-high vacuum system and the structural characterisation

The $Au_{1-x}Pt_x(111)/Co(0001)/W(110)$ trilayer is grown in ultra-high vacuum (UHV) conditions with pulsed laser deposition (PLD). The UHV system is composed of four different chambers connected via a tunnel: two depositions chambers for the deposition of metals or molecules, an analysis chamber where the substrate is degased and the STM chamber. The whole system is equipped with primary, turbo and ionic pumps, which allow working in UHV conditions. The deposition chamber that we use has a base pressure of $6.7 \cdot 10^{-9}$ Pa. It is equipped with a heated sample holder with a tantalum filament, which may be rotated in the azimuthal direction, a 10-30 keV high resolution electron gun coupled to a fluorescent screen equipped with a 10 bit CCD camera for reflection high energy electron diffraction (RHEED) experiments, and a eight-slot metal target holder for PLD. Furthermore, the chamber is equipped with a movable mask that allows varying the composition/thickness of the layer, and two electron-beam evaporators (Tectra GmbH) for molecular beam epitaxy. The movements of the mask and the target holder are motorised and computer-controlled.

Substrate temperatures up to 1223 K can be achieved with this setup, calibrated by an optical pyrometer and controlled routinely with a thermocouple in direct contact with the rear of the molybloc. Owing to this indirect measurement of temperature, error bars on temperature reading might be significant, especially in the low temperature range, between 298-523 K, because of thermal inertia. On the other hand, the growth rate, typically of 0.5 Å/min, is calibrated with a quartz microbalance.

A solid state laser with crystals of Nd-YAG is used for the PLD. It emits a pulsed photon beam with a wavelength of 532 nm. The pulse frequency may be tuned between 10 Hz and 20 Hz, the pulse length is below 10 ns and its power is 10 MW. Typically the spot size is 3 mm^2, with a fluence (density of laser energy per pulse and area) on the target surface of 100 MW/cm^2.

The stack has been structurally characterised in-situ by RHEED and STM, and *ex-situ* by the in-lab X-ray diffraction and grazing X-ray diffraction (GXRD) experiments performed at the BM32 beamline of ESRF[1].

[1]The measurements were performed by Maurizio De Santis (Institut Néel) as the sanitary restrictions because of *Covid-19*, limited the numbers of users allowed at ESRF

4.2 | Growth of $Au_{1-x}Pt_x/Co(t_{Co})/W(110)$ stack

This section is organised as follows: first, we will describe the procedure followed for the growth. Then we will give the details of each step of the growth, which was carried out taking into account the state of the art reported in the literature. The structural characterisation will also be described.

4.2.1 | Growth procedure

In this subsection, we will summarise the procedure followed to grow the $Au_{1-x}Pt_x/Co/W(110)$ stack.

1. The sapphire substrates are cleaned and mounted on sample holders of molybdenum, and outgased prior to the deposition.
2. Deposition of 0.8 nm of Mo (molybdenum) at room temperature.
3. Deposition of 10 nm of W (tungsten) at 373 K, followed by an annealing at 1073 K for 1 h.
4. Deposition of a Co (cobalt) layer at approximately 373 K, either of fixed thickness, or as a wedge between 0.6 nm and 2 nm.
5. Deposition of a 2 nm layer of Au (gold), Pt (platinum) or a solid solution, $Au_{1-x}Pt_x$, at room temperature, at a deposition rate of $v = 1\text{ML}/300\text{s}$. The solid solution is achieved by depositing sequentially Au and Pt with the shape of opposite wedges, with an area of pure element on each side. Their typical thickness is 0.1 nm with a view to promote the mixture of both elements at the atomic level and avoid the formation of misfit dislocations that would occur for thick individual layers. The growth temperature protocol is identical to that used for pure layers.

4.2.2 | Sapphire substrate

Sapphire, Al_2O_3, crystallises in a hexagonal close-packed (hcp) Bravais lattice with parameters $a = 4.785$ Å, $c = 12.991$ Å (Figure 4.1). Sapphire is an ideal substrate for the deposition of epitaxial thin films due to the absence of grain boundaries and porosity.

The epitaxial relationship between bcc refractory metals such as W or Mo and sapphire bulk planes is unique:

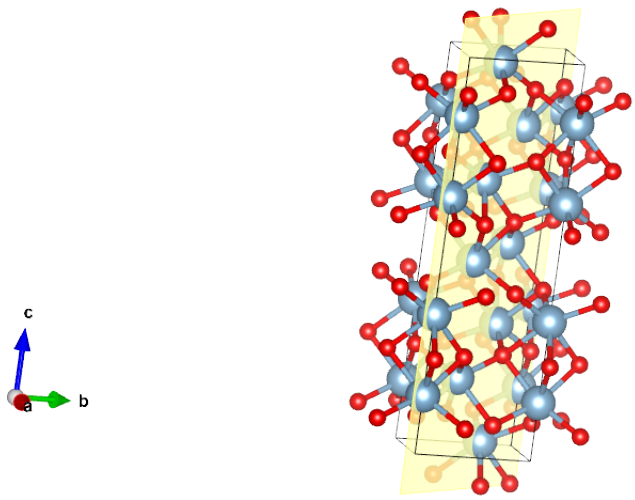

Figure 4.1: **Crystal structure of hcp-**Al_2O_3. The red spheres represent the oxygen atoms while the blue spheres represent aluminium atoms. The yellow plane represents the $(11\bar{2}0)$ plane.

- $(110) \parallel Al_2O_3(11\bar{2}0)$,
- $(111) \parallel Al_2O_3(0001)$,
- $(112) \parallel Al_2O_3(1\bar{1}00)$.

As we are interested in the bcc (110) plane, we use Al_2O_3 with the $(11\bar{2}0)$ orientation, also called R-plane (yellow plane in Figure 4.1). Commercial sapphire wafers are cut into 6.5 mm× 8.5 mm rectangles with the help of a Nd—YAG laser focused on the backside of the wafer, with a spherical lens with $f = 200$ mm. The rear of the wafer is then coated with a 200-300 nm-thick layer of W deposited by magnetron sputtering. The purpose of this layer is to absorb most of the heating radiation emitted by the filament on the deposition stage. Without this layer a significant amount of radiation is absorbed directly by the epitaxial film, resulting in high and uncontrollable temperatures.

Prior to its introduction into the UHV system, the substrate is cleaned with an ultrasonic bath of RBS25 and deionised water (20%/80%) for 5 min, rinsed with an ultrasonic bath of deionised water for 5 min and finally dried with nitrogen. Once introduced into the UHV system, the substrate it is outgased at 1073 K for 1 h and allowed to cool down at room temperature for 1 h. At this stage, the crystal surface consists of atomically-flat 150 nm wide terraces separated by single atomic steps [111].

RHEED

Due to its surface-monolayer sensitivity, RHEED can be used to have an idea of the surface topography. As in other diffraction-based techniques, the resulting diffraction pattern displayed by RHEED results from the intersection between the Ewald's sphere of the incident electron beam and the reciprocal space of the crystal. Due to the low penetration depth of electrons, a flat epitaxial film is viewed by grazing incidence electrons as a one monolayer monocrystalline film, whose corresponding reciprocal space is made of rods.

The intersection of these rods with a large radius in the Ewald's sphere, generally results into parallel streaks rather than spots. Spots or short streaks can be observed only in the case of exceptionally good monocrystalline surfaces, both in terms of in-plane crystallite size and surface flatness. Similarly to X-ray diffraction, broader streaks are characteristic of smaller crystallite extension in real space. Finally, when the surface is no longer 2D, and has multi steps, or 3-dimensional (3D) islands, the diffraction pattern becomes more complex. A more general and detailed description of RHEED may be found on [112; 113; 114].

4.2.3 | Tungsten

The bulk tungsten (W) crystal is a cubic crystal system with a body-centered cubic (bcc) Bravais lattice with lattice parameter $a = b = c = 3.165$ Å, and space group $Im\bar{3}m$ (Figure 4.2 **a)**). Tungsten is chosen as buffer layer because of its large SOC and therefore, a non-zero DMI is expected at the interface with a ferromagnetic material.

Tungsten grows on Al_2O_3 $(11\bar{2}0)$ on the W(110) orientation (Figure 4.2 **b)**). As already known, the growth of refractory bcc-(110) metals on sapphire $Al_2O_3(11\bar{2}0)$ shows a dual epitaxial relationship both sharing bcc[111] ∥ Al_2O_3[0001]. The dominant epitaxial relationship is bcc[001] ∥ $Al_2O_3[1\bar{1}02]$ [115], while the minority epitaxial relationship is attributed to a 70° in-plane rotated relationship. These two relationships lead to the formation of twin crystals [116].

While in the case of Mo [115], or Nb [117] a unique epitaxial relationship can be promoted by annealing at high temperature, this is not the case of W layers. In order to eliminate the minority twins, we follow the procedure proposed by Fruchart et al. [111], and a dusting layer of Mo is deposited, typically 0.6-1 nm at room temperature, prior to the W deposition. Next, 10 nm of W are deposited at 373 K. At this stage,

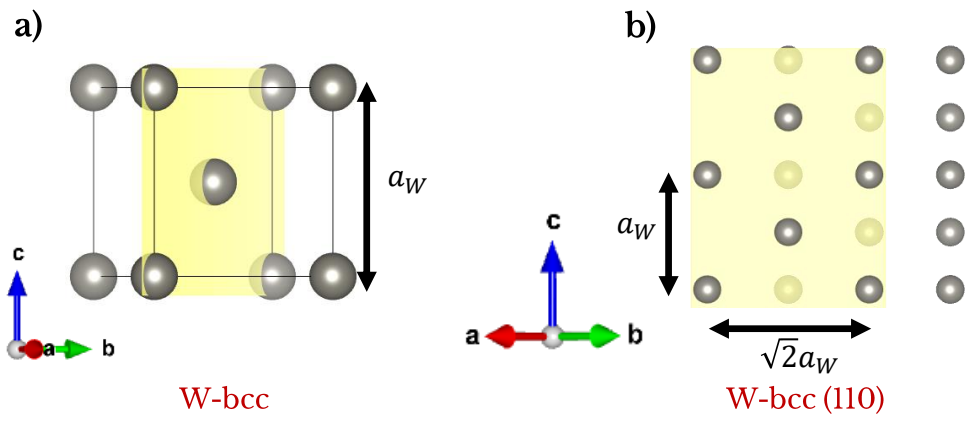

Figure 4.2: **Crystal structure of bcc-W a)** Conventional body-centered cubic Bravais lattice of W-bcc. In yellow is shown the (110) plane. **b)** (110) plane of Tungsten. The coloured arrows represent the reference system chosen.

RHEED and STM show that the W(110) surface is rough, displaying grooves oriented along the W[001] (See Fig. 4.3 **a)**), a common feature for bcc (110) epitaxy grown at low temperature [115; 118; 119]. After the deposition, an annealing at 1100 K for 1 h is performed. The purpose of this annealing is to improve the crystalline quality and to remove the twin crystals, promoting a unique epitaxial relationship.

After annealing, the RHEED diffraction pattern shows a sharp 1×1 pattern (Fig. 4.5 **a)**), revealing that the minority twin has vanished. Furthermore, bright straight lines features are also observed, called *Kikuchi lines*, associated to high-quality surfaces. Atomically-flat terraces of about 150 nm size, separated by monoatomic surface steps are observed by STM, showing a root mean square roughness of about 50 pm.

The high quality of the W(110) layer is confirmed *ex-situ* by in-lab X-ray diffraction (XRD) measurements in the $\theta - 2\theta$ geometry where the out-of-plane wavevector is measured (See Fig. 4.3 **b)**). The out-of-plane lattice parameter does not show a detectable deviation from the bulk lattice parameter. In addition, Kissing fringes with many orders are also observed, confirming the flatness of both interfaces of W(110). The crystalline size shows a value equal to the film thickness.

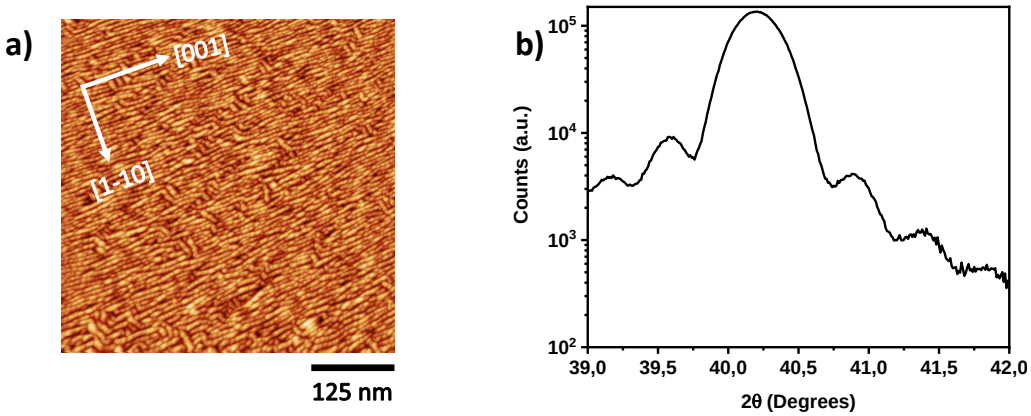

Figure 4.3: **Morphology of as-deposited tungsten studied wit scanning tunneling microscopy and after annealing with x-ray diffraction a)** Tungsten morphology as-deposited with scanning tunneling microscopy. Two types of grooves orientation are observed. The majority is along the W-[001] **b)** x-ray diffraction in the $\theta - 2\theta$ geometry of a bcc-W film grown at 373 K and annealed at 1073 K. The W(110) peak is located at θ =40.1°, with Kissing fringes.

In-plane and out-of-plane scans by GXRD, allows determining the in-plane and out-of-plane lattice parameter. The in-plane lattice parameter is found to be equal to $a = b$ =3.156 Å ± 0.01 Å, while the out-of-plane lattice parameter is found to be c =3.157 Å ± 0.01 Å. These values are slightly lower than the bulk value $a = b = c = 3.165$ Å.

4.2.4 | Cobalt

The bulk cobalt (Co) crystal is a hexagonal crystal system with a hcp Bravais lattice with lattice parameter $a = 2.51$ Å and $c = 4.07$ Å , and space group $P6_3/mmc$ (Figure 4.4). Cobalt is ferromagnetic at room-temperature with a bulk exchange stiffness of $A = 30\,\mathrm{pJ/m}$, spontaneous magnetisation of $M_s = 1.4\,\mathrm{MA/m}$ and a g-Lande factor equal to 2.17.

The growth of Co thin films on W(110) has been widely studied [116; 120; 121; 122]. Cobalt grows quasi-layer-by-layer [18; 116; 122] on W(110) in the so-called Nishiyama-Wasserman orientation, where W[001] ∥ Co[11$\bar{2}$0] (Fig. 4.6 **a)**) [123; 124]. We consider the W(110) framework, being the x-direction parallel to the W[1$\bar{1}$0], and the y-direction parallel to the W[001]. Due to the different symmetries of the two films, two in-plane mismatches need to be considered:

$$\Delta_x = \frac{a_{W,[\bar{1}10]} - a_{Co,[1\bar{1}00]}}{a_{W,[\bar{1}10]}} = 2.98\%, \quad \Delta_y = \frac{a_{W,[001]} - a_{Co,[11\bar{2}0]}}{a_{W,[001]}} = 20.79\%. \tag{4.1}$$

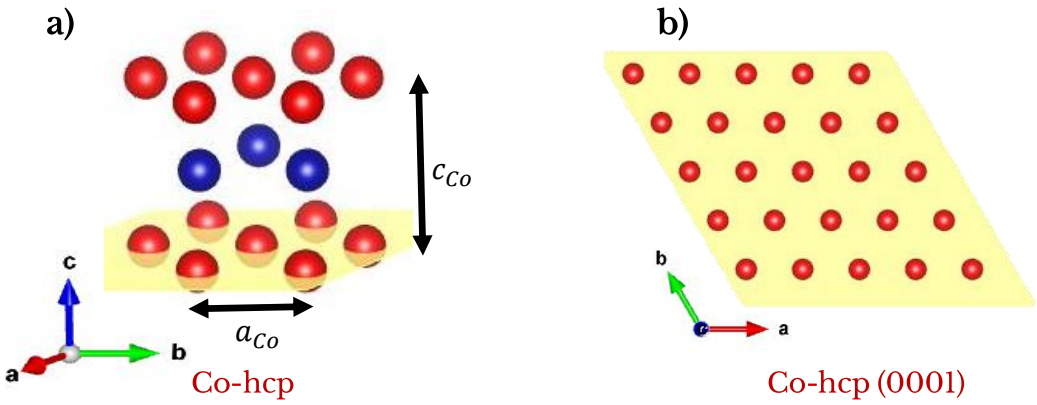

Figure 4.4: **Crystal structure of hcp-Co. a)** Conventional hexagonal close-packed Bravais lattice of Co. Red spheres: Plane A. Blue spheres: Plane B. In yellow is shown the (0001) plane. **b)** (0001) plane of Co. The coloured arrows represent the chosen reference system.

Due to these two in-plane mismatches, three different growth regimes may be observed, depending on the Co ML coverage [2] :

1. Up to 0.7 ML , the hcp-Co grows pseudomorphically on W(110);
2. Above 0.7 ML and up to 10 ML, a reconstruction of the Co structure takes place due to the large lattice mismatch along W[001], where five Co atoms cover four W atoms . This supercell is schematically shown in Fig. 4.6 b) ;
3. Above 10 ML, the elastic energy of the Co layer is too high, and the Co layer relaxes.

While the first two regimes show a strained Co layer with a two-fold symmetry, only Co layers above 2.5 ML show a ferromagnetic order at room-temperature. Therefore, we will focus on Co layers between 2.5 and 10 ML, where the Co layer is ferromagnetic and shows a two-fold symmetry.

Figure 4.5 **a)** shows the RHEED diffraction patterns of W(110) and Co(0001) for 4 ML of Co, with the incoming wavevector perpendicular to the Co $[1\bar{1}00]$ ||W $[1\bar{1}0]$,

[2] We consider 1ML= $\frac{c_{Co}}{2} \approx 2$ Å

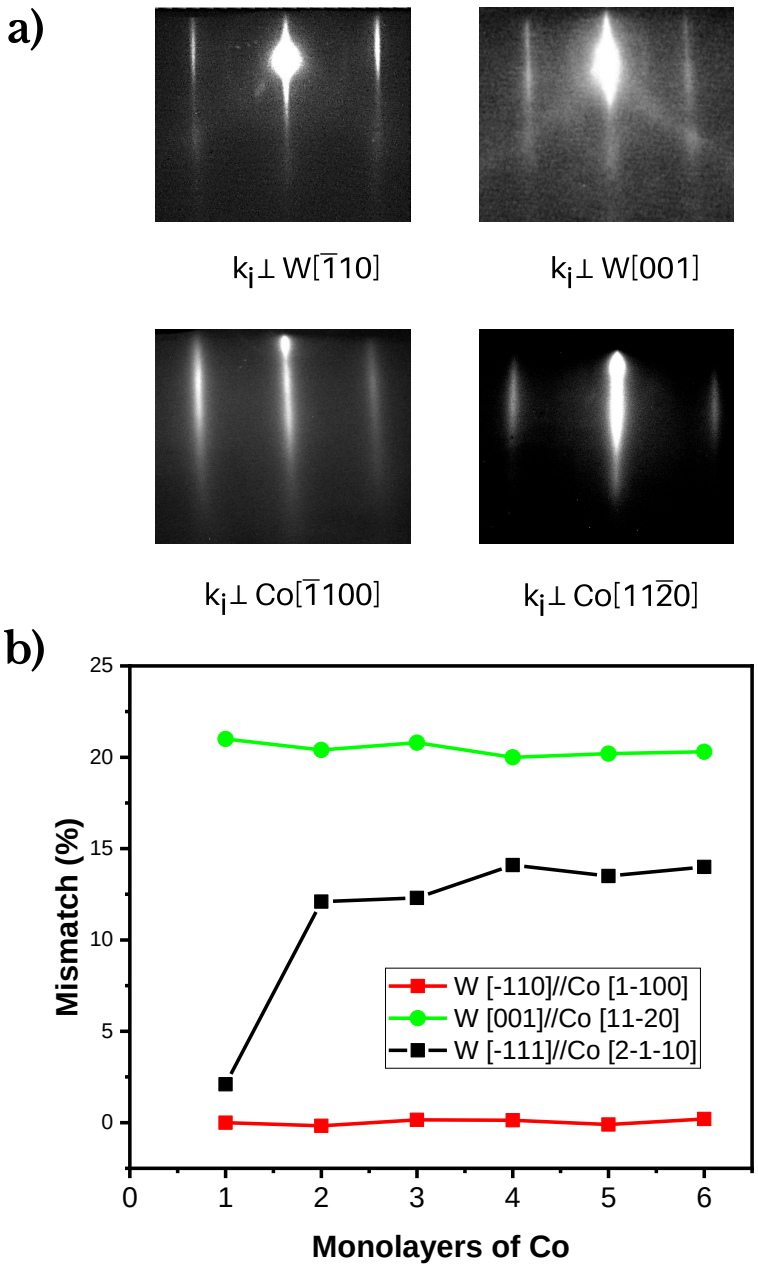

Figure 4.5: **hcp-Co(0001)/bcc-W(110) reflection high energy electron diffraction along the two main in-plane directions. a)** reflection high energy electron diffraction patterns with the incoming wavevector perpendicular to the two main in-plane directions of Co(0001) and W(110) **b)** Cobalt mismatch as function of the number of Co monolayers.

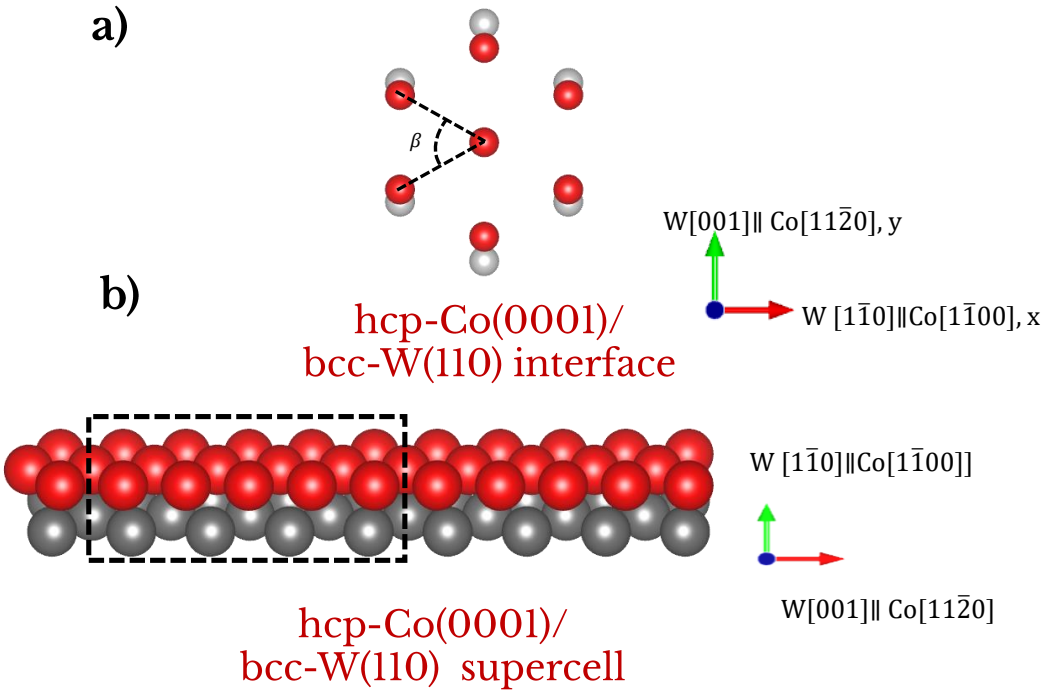

Figure 4.6: **hcp-Co(0001)/bcc-W(110) interface**. **a)** Sketch of the hcp-Co (0001)/bcc-W(110) interface. Red spheres represent Co atoms, while grey spheres represent W atoms. **b)** Cross-section of the Co (0001)/bcc-W(110) interface. The dashed box represents the Co supercell of 5 atoms of Co per 4 of W, along W[001].

and Co [11$\bar{2}$0] || W[001], the two main in-plane crystallographic directions of W(110). When the incoming wavector $\mathbf{k_i}$ is perpendicular to **x** the streak distance is the same for W(110) and Co(0001), and therefore they share the same lattice parameter along this direction. On the other hand, when the incoming wavevector is perpendicular to **y**, the streak distance for W(110) and Co(0001) is different, and therefore the lattice parameters are different along this direction. In summary, the Co(0001) layer is pseudomorphic along W[1$\bar{1}$0], and it is relaxed along W[001]. Figure 4.5 **b)** shows the evolution of the mismatch as a function of the number of Co ML, in a good agreement with the mismatch predicted by Eq. 4.1.

Ex-situ GXRD was performed on four different stacks with different thicknesses of Co and two different compositions of $Au_{1-x}Pt_x$, in order to clarify whether the different composition of the capping layer might induce a relaxation on the Co(0001) layer.

Table 4.1: **Experimental lattice parameters or hcp-Co(0001) and bcc-W(110) found by grazing x-ray diffraction**

	$x = 0$				$x = 0.3$		
	a [Å]	b [Å]	c [Å]		a [Å]	b [Å]	c [Å]
W(110) bulk	*4.476*	*3.165*	*4.476*				
Experimental	4.46(1)	3.156(6)	4.456(7)		4.464(9)	3.155(5)	4.464(9)
Co(0001) bulk	*4.3424*	*2.5071*	*4.0695*				
Experimental							
t_{Co}=8.5 Å	4.455(8)	2.544(4)	4.24(4)	=8.5 Å	4.469(9)	2.543(2)	4.24(7)
=17 Å	4.420(7)	2.529(4)	4.10(4)	=10 Å	4.464(9)	2.545(2)	4.17(3)

- A: fcc-Au(111)/hcp-Co(0001)(10 Å),
- B: fcc-Au(111)/hcp-Co(0001)(16 Å),
- C: fcc-$Au_{0.7}Pt_{0.3}$(111)/hcp-Co(0001)(8.5 Å),
- D: fcc-$Au_{0.7}Pt_{0.3}$(111)/hcp-Co(0001)(10 Å).

In-plane scans of the reciprocal space were performed along Co[$1\bar{1}20$] ∥ W[001], Co[1100] ∥ W[$1\bar{1}0$] and Co[$2\bar{1}\bar{1}0$] ∥ W[$1\bar{1}1$] and their equivalent positions. In addition, an out-of-plane scan along Co[0001] was taken to determine the out-of-plane lattice parameter of the Co layer. The lattice parameters of W(110) and Co(0001) are shown in Table 4.1. The lattice parameters $[a, b, c]$, refer to the lattice parameter along the W[$1\bar{1}0$], W[001] and W[110], respectively.

Between a Co thickness of 8.5 Å and 17 Å, corresponding to 4 ML and 7.8 ML of Co respectively, the Co layer grows strained on W(110), with a lattice parameter reduced by 3% along W[$1\bar{1}0$] and increased by 1% along W[001], with respect the bulk lattice parameter of Co, 2.5071 Å. This is independent of the capping layer. Due to the Co reconstruction, an expansion of the unit cell volume is found to be about $\Delta V/V = 8 \pm 1\%$.

Furthermore, the out-of plane scans confirm that the Co layer is pure hcp. This is in disagreement with the work of Wawro et al. [125], who found by ^{59}Co nuclear magnetic resonance that Co grown on Mo(110), which is structurally and chemically

equivalent to W(110), grows with a mixture of hcp and fcc phases. The disagreement may be explained by the different deposition techniques used in this work (molecular beam epitaxy was used in their case).

Above 17 Å (8 ML), the Co layer relaxes along both in-plane directions. This critical thickness relaxation is found to be slightly lower than in previous experimental results, where it was found to be at 20 Å. This discrepancy may be also explained by the different deposition technique used for our layers (PLD) with respect to the previous works, (molecular beam epitaxy) [116].

4.2.5 | Gold and platinum

The bulk gold (Au) and platinum (Pt) crystals are noble heavy metals with a face-centered cubic (fcc) Bravais lattice with lattice parameter $a_{Au} = 4.08$ Å and $a_{Pt} = 3.92$ Å (Figure 4.7 **a)**). Gold and Pt grow on top of hcp-Co (0001) with the fcc-(111) orientation (Figure 4.7 **b)**). These metals are chosen as capping layers in order to protect Co from oxidation and due to their strong SOC, and therefore large interfacial perpendicular anisotropy and DMI obtained at the interface with Co.

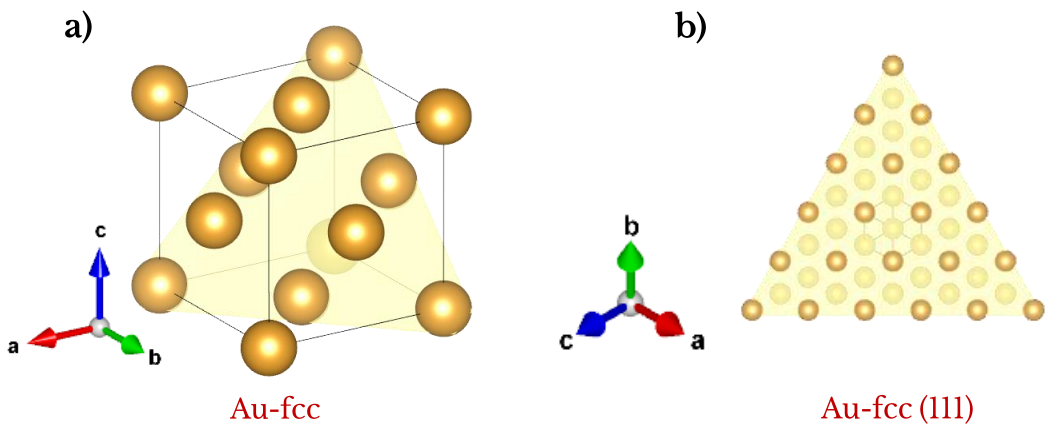

Figure 4.7: **Crystal structure of fcc-Au a)** Conventional face-centered cubic Bravais lattice of Au-fcc. Yellow spheres represent Au atoms. In light yellow is shown the (111) plane. **b)** (111) plane of gold. The coloured arrows represent the chosen reference system.

Either pure metals or solid-solutions with different composition ratio can be deposited. A solid solution is achieved by alternating the deposition of sub-MLs of Au and Pt, depending on the desired composition. Due to the sub-ML thickness of each deposition, the mixture of the two elements at the atomic level is enhanced and allows avoiding the formation of misfit dislocations [111; 117]. In all the range of composition, an α-phase made of fcc-(111) (Au) + (Pt) is found [126], which is likely to result in averaged properties of the two pure metals (crystal lattice constant, interfacial MCA and DMI).

According to the empirical Vegard's law [127; 128], the lattice parameter of a solid solution of two constituents is approximately a weighted mean of the two constituents' lattice parameters:

$$a_{A_{1-x}B_x} = (1-x)a_A + xa_B. \tag{4.2}$$

In order to verify the Vegard's law in our system, different capping layers with fixed composition were deposited. Figure 4.8 shows the derived in-plane lattice parameter of $Au_{1-x}Pt_x$ for different compositions, x. A quasi-linear decrease of the lattice parameter is observed, as expected from Vegard's law behaviour. Yet, the absolute value of the lattice parameter is slightly lower than the bulk unit cell. This is probably due to the fact that Pt layers for this low thickness show a compression of about 2% [129].

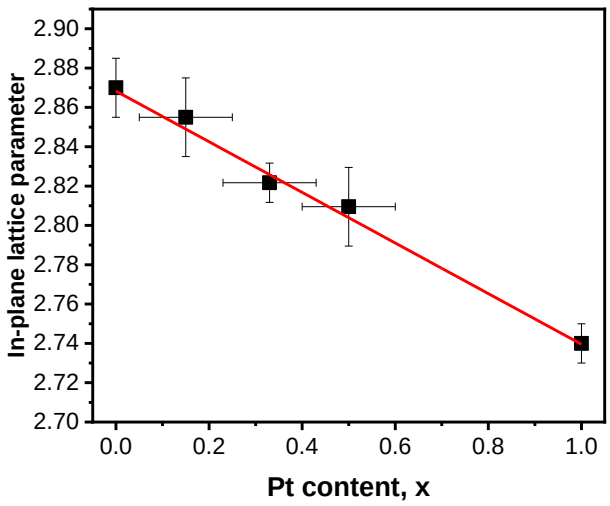

Figure 4.8: **In-plane lattice parameter fcc-$Au_{1-x}Pt_x$ for different compositions.** The derived in-plane lattice parameter are derived from the linear regression of 5 in-plane lattice reflections. The red line represents a linear fit of the experimental data.

In the $\theta - 2\theta$ diffraction pattern, the peaks associated to Au(111) and Pt(111) were not observed, due to the overlapping with the sapphire peaks and the low signal given associated to the low thickness.

From the GXRD experiments, the $[a, b, c]$ lattice constants were found to be equal to $[2.813, 4.864, 2.4]$ Å. The value of a is very close to the one derived by RHEED, showing a compression of 1.5% with respect the bulk value. Considering the lattice parameter found by Bulou et al. [129] for ultra thin films of Pt(111), $a_{Pt} = 2.71$Å, a composition of $x = 0.29 \pm 0.03$ is found, very close to the nominal one of $x = 0.3$.

4.2.6 | Summary

In this section we have described the growth process of the $Au_{1-x}Pt_x/Co/W(110)$ tri-layer stack as well as the in-situ and ex-situ characterisation. The W(110) layer is characterised by STM, RHEED and GXRD showing very high quality. On the other hand, the Co layer, which grows layer-by-layer, creates a supercell on W(110) with the same lattice parameter along the W$[1\bar{1}0]$ direction but relaxed along the W[001], reducing its symmetry to a two-fold symmetry, as observed by GXRD and RHEED. Furthermore, it is observed that the Co relaxes at t_{Co} =1.6 nm. Finally, the in-plane lattice parameter of the $Au_{1-x}Pt_x$ solid solution, is observed to decrease as the Pt content increases, following Vegard's law. In addition, by GXRD the whole unit cell is determined, allowing to extract a volume corresponding very closely to the nominal one.

4.3 | Magnetic characterisation

The magnetic characterisation of the $Au_{1-x}Pt_x/Co/W(110)$ stack is performed by a combination of magneto-optical Kerr effect (MOKE) microscopy in the polar configuration and Brillouin light scattering (BLS). Prior to the presentation of the results, a brief introduction of the BLS working principle is provided

4.3.1 | BLS introduction

The BLS process can be understood as the inelastic scattering between spin-waves (SW)s or magnons and photons. A scheme of this scattering process is depicted in Fig. 4.9. This process is described by the following energy and momentum conservation laws:

$$h\omega_{\text{out}} = h\omega_{\text{i}} \mp h\omega_{\text{SW}}, \tag{4.3}$$

$$\hbar\mathbf{k}_{\text{out}} = \hbar\mathbf{k}_{\text{i}} \mp \hbar\mathbf{k}_{\text{SW}} \tag{4.4}$$

where $\omega_{\text{out}}, \omega_{\text{i}}$ and ω_{SW} are the scattered, the incoming, and the SW frequencies, which carries a wavector $\mathbf{k}$. The negative sign refers to a Stokes process, the creation of a SW, while a positive sign refers to the anti-Stokes process, the annihilation of a SW. Due to the energy and momentum conservation, Eqs. 4.3 and 4.4, the scattered light carries information about the probed SW. The SW wavector is given by

$$k_{\text{SW}} = \frac{4\pi \sin\theta_{\text{inc}}}{\lambda}, \tag{4.5}$$

where θ_{inc} is the angle of incidence and λ=532 nm (green light) the wavelength of the incident light in this experiment.

Two different geometries, schematically shown in Fig. 4.10 are used in this thesis:

- **Damon-Eshbach (DE) or magnetostatic surface waves configuration**. In this configuration, the magnetisation and the SW wave vector are in-plane and mutually perpendicular to each other.
- **Magnetostatic backward volume waves (BVW) configuration** . In this configuration, the magnetisation and the SW wavector are in-plane and parallel/antiparallel to each other.

The influence of the interfacial DMI on the SW spectrum is now well-known, both from theoretical studies [130; 131; 132], and from experimental results [133; 134; 135;

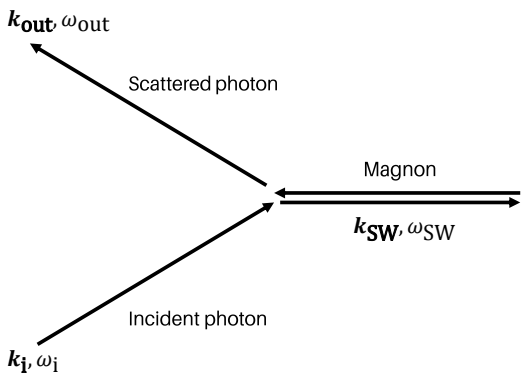

Figure 4.9: **Feynman diagram of the Brillouin light scattering mechanism**

136]. The DMI induces a characteristic non-reciprocity to the SW propagation, such that SW travelling along opposite directions with the same wavevector have different frequencies. In ultrathin films with isotropic DMI, the symmetry of the DMI imposes only Néel-type rotation and therefore the SW must be probed in the DE geometry. Furthermore, this non-reciprocity has also been predicted in systems with bulk DMI, in which it can be experimentally observed by using the BVW geometry (See Fig. 4.10) [131; 137]. In our system, as we will discuss later, the DMI can be decomposed into Néel and Bloch-type depending on the crystallographic direction, and therefore both the DE and the BVW need to be used to probe both types of DMI.

The SW frequency can be separated into a symmetrical and anti-symmetrical component:

$$f_{\text{Stokes}} = f_0 \pm \frac{\Delta f}{2}, \tag{4.6}$$

$$f_{\text{Anti-Stokes}} = f_0 \mp \frac{\Delta f}{2}, \tag{4.7}$$

where $f_0 = \frac{|f_{\text{Stokes}}| + |f_{\text{Anti-Stokes}}|}{2}$ is the resonant frequency in the absence of DMI and $\Delta f = |f_{\text{Stokes}}| - |f_{\text{Anti-Stokes}}|$ is the asymmetry in the resonant frequency induced by the DMI.

Within the Co(0001) framework, characterising the samples studied in this PhD thesis, we define the x- and y-axis as the easy- and hard- in-plane axes, respectively. In this framework the SW frequencies are given by [18]:

$$f_x = f_{0,x} \pm f_{\text{DMI},x}, \tag{4.8a}$$

$$f_y = f_{0,y} \pm f_{\text{DMI},y}, \tag{4.8b}$$

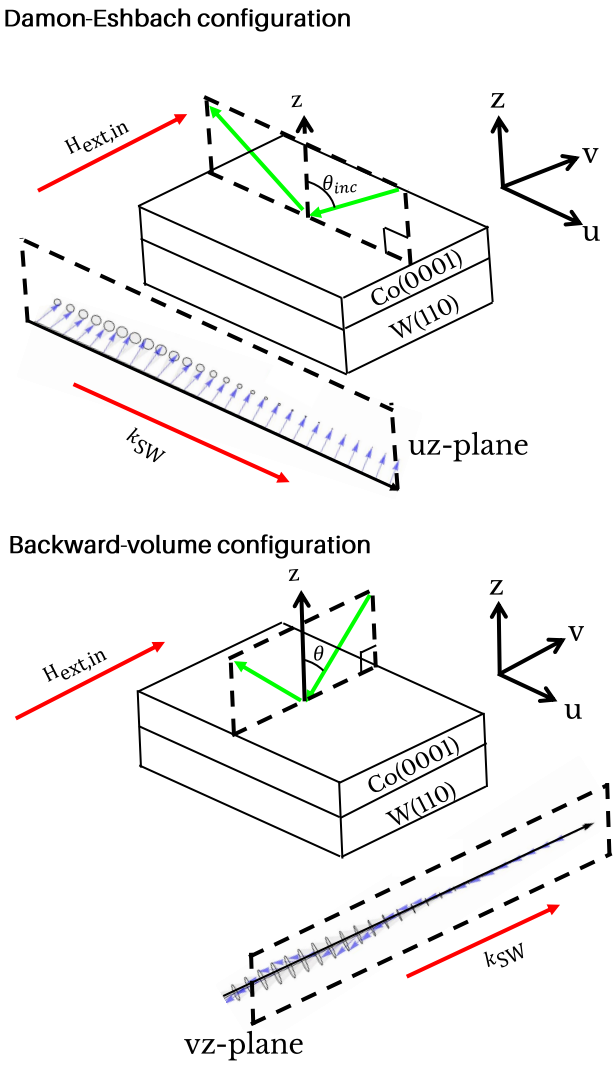

Figure 4.10: **Spin waves propagation geometries. (Top)** Damon-Eshbach configuration. Under a sufficiently large in-plane field to align the magnetisation along **v**, the spin-wave is in-plane propagating along **u**. **(Bottom)** Backward-volume configuration. Under a sufficiently large in-plane field to align the magnetisation along **v**, the spin-wave is in-plane propagating along **v**. Green arrows represent the incident and scattered light.

with

$$f_{0,x} = \frac{\gamma\mu_0}{2\pi}\sqrt{\left(H_{\text{ext,x}} + H_{\text{in}} + Jk_{\text{SW}}^2 + M_{\text{s}}P(k_{\text{SW}})\right)\left(H_{\text{ext,x}} - H_{\text{out}} + H_{\text{in}} + Jk_{\text{SW}}^2 - M_{\text{s}}P(k_{\text{SW}})\right)}, \tag{4.9a}$$

$$f_{0,y} = \frac{\gamma_0}{2\pi}\sqrt{\left(H_{\text{ext,y}} - H_{\text{in}} + Jk_{\text{SW}}^2 + M_{\text{s}}P(k_{\text{SW}})\right)\left(H_{\text{ext,y}} - H_{\text{out}} + Jk_{\text{SW}}^2 - M_{\text{s}}P(k_{\text{SW}})\right)}, \tag{4.9b}$$

$$f_{\text{DMI}} = \frac{\gamma}{\pi M_{\text{s}}} D k_{\text{SW}}, \tag{4.9c}$$

where H_{ext} represents the external in-plane magnetic field, which has to be strong enough to align the magnetisation along the field-direction; M_s is the spontaneous magnetisation, γ is the absolute value of the gyromagnetic ratio $\left(\frac{\gamma}{2\pi}\right) = g \times 13.996\,\mathrm{GHzT}^{-1}$ with g the Lande factor, equal to 2.17 for Co [33]. The SW stifness is represented by $J = \frac{2A}{\mu_0 M_s}$. The out-of-plane and in-plane anisotropy fields are represented by H_{out}, and H_{in}, respectively. Finally, $P(k_{SW}) = 1 - \dfrac{1 - \exp(-|k_{SW}|t_{FM})}{|k_{SW}|t_{FM}}$ is a geometric factor and D represents the DMI constant along the SW propagation direction.

While the symmetric component, f_0 depends on the exchange stiffness, the applied magnetic field, and the anisotropic magnetic fields, as well as on the SW wavector, k_{SW}, the antisymetric component, Δf is directly linked to the DMI constant parallel to the SW propagating plane. Therefore, by measuring the symmetric component the exchange stiffness and the different anisotropies may be derived, while the DMI strength along a particular direction can be measured from the anti-symmetric component by rotating the sample along its normal, i.e. by rotating the propagation plane with respect the field direction.

The measurements are performed at *Laboratoire de Physique des Solides (Orsay)* by André Thiaville, at room temperature, 298 K, where thermally activated spin-waves are probed with a green laser, λ =532 nm. The Stokes and Anti-Stokes peaks of the spectra for different wave-vectors are fitted with a Lorentzian asymmetric function:

$$I(f) = I_0 + \frac{A + C(f - f_0)}{(f - f_0)^2 + B^2}. \tag{4.10}$$

4.3.2 | C_{2v} DMI symmetry

When measuring along intermediate directions, it is convenient to express the DMI constant in terms of a general basis $[u, v] = R_z(\alpha)[x, y]$, where $R_z(\alpha)$ is the rotation matrix around the z-axis (See Fig. 4.11 **a)**). By transforming the magnetisation components into this new basis, $[m_x, m_y, m_z] \longrightarrow [m_u, m_v, m_z]$, the DMI energy density associated to a 1D spin modulation propagating along **u** is given by:

$$E_{DMI} = \mathcal{D}_{Néel} L^u_{uz} + \mathcal{D}_{Bloch} L^u_{vz}, \tag{4.11}$$

with

$$\mathcal{D}_{Néel} = D_x \cos^2\alpha + D_y \sin^2\alpha, \tag{4.12}$$

$$\mathcal{D}_{Bloch} = \left(\frac{D_x - D_y}{2}\right) \sin 2\alpha, \tag{4.13}$$

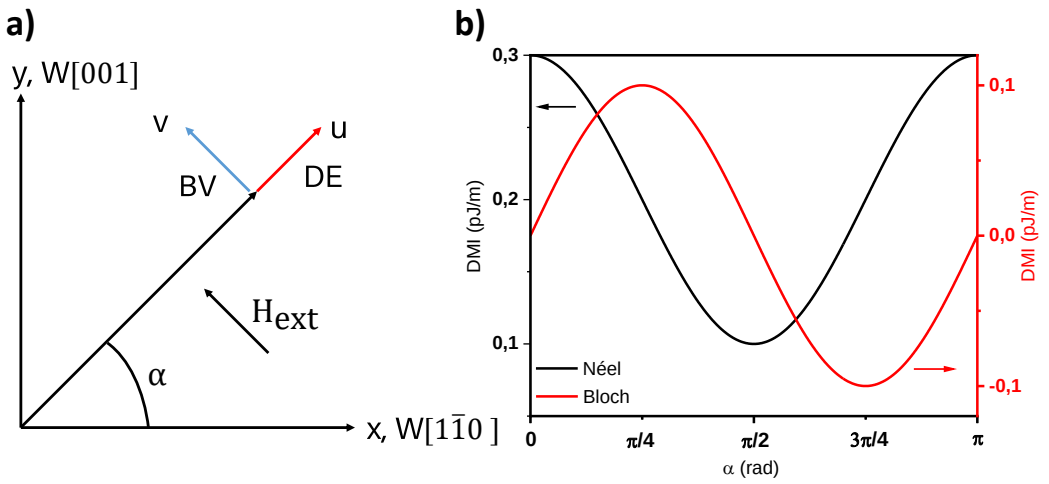

Figure 4.11: **Brillouin light scattering framework W(110) for an anisotropic Dzyaloshinskii–Moriya interaction. a)** Sketch of the W(110) framework used for Brillouin light scattering experiments. When the external in-plane field is applied along **v**, the spin-wave propagates along **u** (**v**) in the Damon-Eshbach (Backward-volume) geometry **b)** In-plane angular dependence of the Néel and Bloch-type Dzyaloshinskii–Moriya interaction. For the plot, $D_y = 3D_x = 0.1\,\mathrm{pJ/m}$.

where D_x and D_y are the DMI constants along the x- and y- directions respectively. Finally, L^u_{uz} and L^u_{vz} are Lifshitz invariants, defined in Chapter 2, promoting rotations along the uz-plane (Néel-type) and vz-pane (Bloch-type).

The competition between the Néel-type and Bloch-type DMI implies that along an intermediate direction, spin spirals (or equivalently DWs) show an intermediate configuration between Néel and Bloch. An intuitive way to visualise the Néel and Bloch DMI type, is to consider the spin spiral plane orientation with respect the modulation direction **u**, as function of the effective DMI fields along the x- and y-axis. This is schematically shown in Fig. 4.12. When the DMI is isotropic, $D_x = D_y$, the two effective fields are identical, and consequently the effective DMI field is fully aligned along the SW modulation direction **u**. Therefore, the angle between the spin spiral plane and the modulation direction is zero, meaning that the spin spiral is purely Néel-type. When the DMI is anisotropic, e.g., ($D_x = 2D_y$) in Fig. 4.12, the two effective fields are different, and therefore the effective DMI field is not completely aligned along the SW modulation direction **u**, being the angle between the effective field and the modulation direction φ_0. Consequently, an effective DMI along **u**, (propagating along the uz-plane) and **v** (propagating along the vz-plane) arises, scaling as $\cos\varphi_0$ and $\sin\varphi_0$, respectively.

This implies that more anisotropic the DMI is, the larger the Bloch DMI component will be, as expected from Eq. 4.13.

Hence, the non-reciprocity of the SW propagation induced by the DMI depends on the propagation direction of the SW. Let's consider that the magnetisation is saturated in-plane along the **v** direction. In the DE configuration, the SW will propagate along the uz-plane, i.e. the non-reciprocity of the SW is due to $\mathcal{D}_{\text{Néel}}$, which is maximum along the two main in-plane directions, $\alpha = 0, 90, 180, 270°$. On the other hand, in the BVW geometry the SW will propagate along the vz-plane, i.e. the non-reciprocity of the SW is due to $\mathcal{D}_{\text{Bloch}}$. This component is non-zero only when the DMI is anisotropic, and its maximum occurs when $\alpha = 45, 135, 225, 315°$, and it vanishes along the two main in-plane directions. A representative graph of the two DMI-type as well as a polar plot as function of the in-plane angular direction α is shown in Fig. 4.11 **b)** and Fig. 4.12.

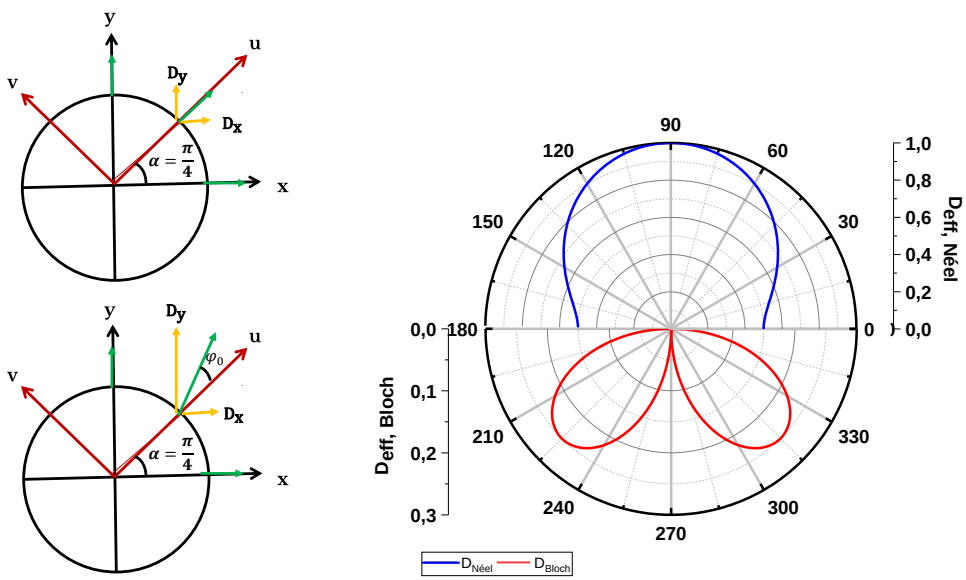

Figure 4.12: **Polar representation of the anisotropic Dzyaloshinskii–Moriya interaction. Left** Polar plot of the magnetisation angle (green arrows) at $\alpha = 0, 45\,°$ and $\alpha = 90°$ when the Dzyaloshinskii–Moriya interaction is isotropic (top) and anisotropic (bottom), with $D_y = 2D_x$. **Right** Polar plot of the Néel (blue line) and Bloch DMI (red line) for $D_y = 2D_x$.

4.3.3 | Spontaneous magnetisation

The spontaneous magnetisation is inferred from vibrating sample magnetometry with superconducting quantum interference devices (VSM-SQUID). The spontaneous magnetisation is found to be independent of the Au-to-Pt content, with a value of M_s= 1.15±0.1 MA/m

4.3.4 | Magnetic exchange

The magnetic exchange is deduced from the curvature of the symmetric component, f_0 *vs* the SW wavector, k_{SW}, (Eq. 4.9). The $Au_{0.58}Pt_{0.42}$/Co/W(110) sample with a cobalt thickness of 0.78 nm was measured in the DE configuration along the two main in-plane directions.

The fitting of f_0 *vs* the SW wavector, k_{SW}, using Eq. 4.9 allows us to measure the SW stiffness and derive the exchange stiffness, J and A respectively (see Table 4.2). The values found along the two directions are close to A=16 pJ/m, in agreement with the typical value of Co ultra-thin films of A=16 pJ/m found by Metaxas et al [138].

Another feature that is interesting to note, is the fact that the magnetic exchange along the hard axis, is slightly larger than along the easy-axis. Starting from an atomistic framework [139], it is possible to show that $A_{EA} < A_{HA}$ as found experimentally. Yet, the value of the error bars does not allow us to conclude unequivocally that this is the case.

Finally, it is not expected that the exchange stiffness varies with the Au-to-Pt-ratio, as the in-plane strain of the Co layer is not modified with the Au-to-Pt content as observed by GXRD. Therefore, we will use the values of A=16 pJ/m found by Metaxas et al [138] for all the concentrations of Pt.

Table 4.2: **Spin-wave stiffness measured by Brillouin light scattering in the Damon-Eshbach configuration for $Au_{0.58}Pt_{0.42}$/Co(0.78 nm)/W(110) along the two in-plane directions.** The derived exchange stiffness using M_s=1.15 MA/m is also shown.

	$x = 0.42$	
	J [pA m]	A [pJ/m]
Easy axis	18±2	13±2
Hard axis	21± 4	15±3

4.3.5 | Magnetic anisotropy

Our system is a double wedge of Co thickness and Au-to-Pt composition. Consequently, we expect a different magnetic behaviour along the two directions of the wedge. This different behaviour is clearly observed in the hysteresis loops collected by MOKE in the polar configuration, under the application of an external out-of-plane magnetic field.

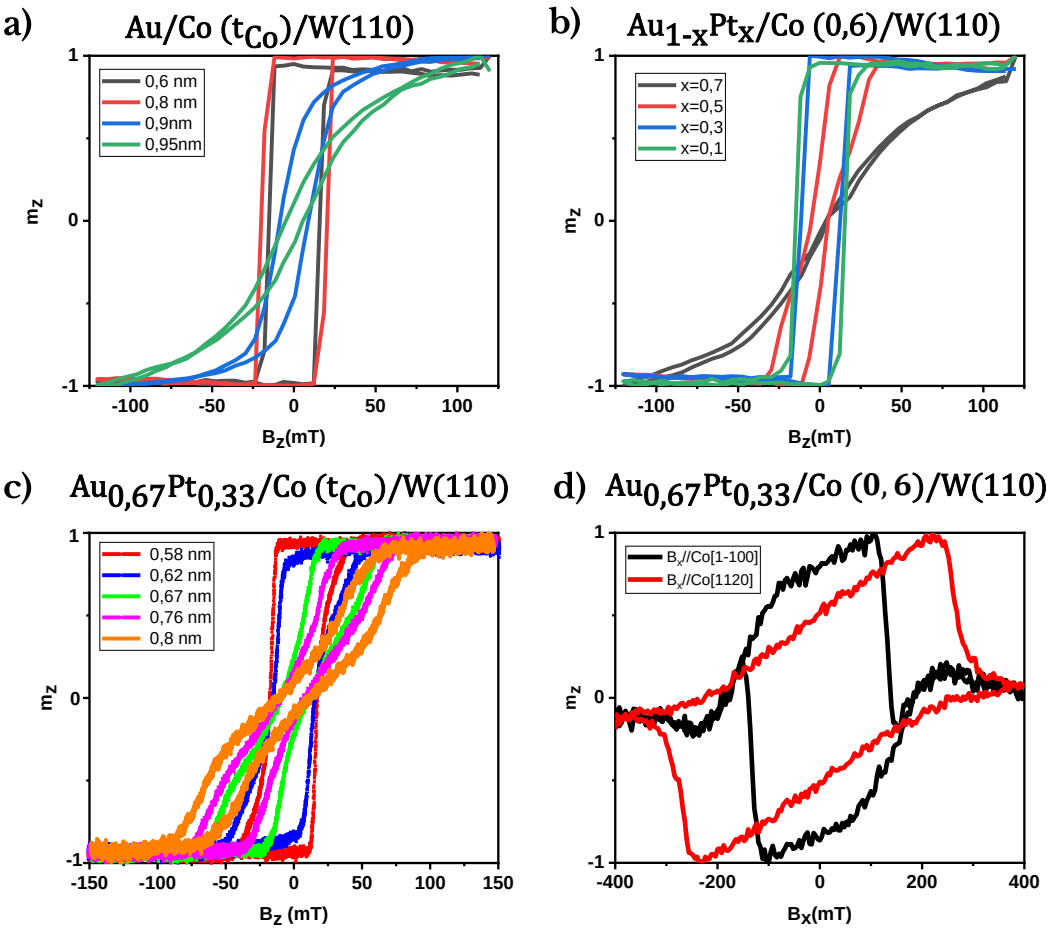

Figure 4.13: **Hysteresis loops taken by polar magneto-optical Kerr effect under the application of an external magnetic field in $Au_{1-x}Pt_x/Co(t_{Co})/W(110)$. a)** For $Au/Co(t_{Co})/W(110)$ as function of the Co thickness, under the application of an out-of-plane magnetic field **b)** for $Au_{1-x}Pt_x/Co(0.6nm)/W(110)$ as function of the Au-to-Pt content, x under the application of an out-of-plane magnetic field. **c)** For $Au_{0.67}Pt_{0.33}/Co(t_{Co})/W(110)$ as function of Co thickness, under the application of an out-of-plane magnetic field. **d)** For $Au_{0.67}Pt_{0.33}/Co(0.6nm)/W(110)$ under the application of an external in-plane magnetic field, B_x along Co[$\bar{1}$100] and Co[11$\bar{2}$0].

Figure 4.13 **a)**, **b)**, **c)** show the hysteresis loops measured for sample positions with different Co thickness and Pt-composition under the application of an external out-of-plane magnetic field. For $Au/Co(t_{Co})/W(110)$ a square hysteresis loop is observed between 0.6-0.8 nm, which indicates that the sample magnetisation is fully saturated at remanence. For thicknesses between 0.9-0.95 nm, the remanence decreases, as we are approaching the spin-reorientation transition due to the decreasing of the MCA. A similar behaviour is observed for a fixed Co thickness $t_{Co} = 0.6$nm with the increasing of the Pt content, x (Fig. 4.13 **b)**). This is an indicative that the interface magnetic anisotropy at the Pt/Co interface is lower than at the Au/Co interface, in line with literature results [39; 140].

Figure 4.13 **c)** shows the hysteresis loops measured at different locations along the wedge, corresponding to different Co thicknesses for $Au_{0.67}Pt_{0.33}/Co(t_{Co})/W(110)$. For t_{Co}=0.58 nm a square hysteresis loop is obtained, which indicates that the sample magnetisation is fully saturated at remanence. With increasing Co thickness, the decrease in the effective anisotropy K_{out} leads to a slanted loop, indicating the presence of a multi-domain state at zero field. The out-of-plane component at zero field decreases as t_{Co} increases from 0.67 nm to 0.8 nm where the magnetisation is close to the spin-reorientation transition, and the remanence is close to zero. This behaviour clearly suggests the interfacial nature of the out-of-plane anisotropy, K_{out}.

The anisotropy fields may be measured either by BLS or by polar MOKE under the application of an in-plane field along the two main in-plane directions. In our MOKE setup we are limited to in-plane fields up to 0.45 T, and therefore, we could not study systematically all the ranges of composition and thickness as for Au/Co(0.65 nm)/W(110) fields of 0.6 T are necessary for saturating the magnetisation along the hard in-plane axis [18]. Yet, for some cases the available in-plane field was strong enough to saturate the magnetisation in-plane. As an example we show the hysteresis loops (Fig. 4.13 **d)**) along the two main in-plane directions for $Au_{0.67}Pt_{0.33}/Co(0.6nm)/W(110)$. The signal is normalised, ± 1 ($m_z = \pm 1$) and 0 ($m_z = 0$). The saturation fields along the two directions are found to be approximately equal to: B_{EA} =0.113 T, and B_{HA} =0.230 T resulting into an interfacial MCA constant, $K_s = 0.6\,mJ/m^2$, and an in-plane magnetic anisotropy, K_{in} =70 kJ/m^3. The different saturation fields along the two in-plane directions, proves the presence of an additional anisotropy within the plane, in addition to the out-of-plane anisotropy.

The anisotropy fields for different content of Pt are derived from BLS measurements in the DE configuration with the external magnetic field aligned along the easy and hard in-plane easy axes. Due to time limitations, we could not measure the whole range

Table 4.3: Experimental anisotropies determined by Brillouin light scattering in the Damon-Eshbach configuration for different Au-to-Pt content in the $Au_{1-x}Pt_x/Co(0.78nm)/W(110)$ stack.

	x=0.2	x=0.42	x=0.6	x=0.8
K_{out} (kJ/m^3)	127±21	28±17 (25)	-106±27	-165±23
K_s(mJ/m^2)	0.75±0.12	0.67±0.1	0.57±0.1	0.52±0.09
K_{in} (kJ/m^3)	68±21	48±17 (54)	62±27	67±23

of SW wavectors along the two in-plane directions for the whole range of Pt content, x. Therefore, we show the results for k_{SW}=20.19 µm^{-1}, as for this wavector, different zones with different Pt content were measured along the two in-plane directions. Figure 4.14 shows the experimental BLS spectrum in the DE geometry for different content of Pt, under an external in-plane field of 0.32 T, applied along the in-plane easy-axis direction, and k_{SW}=20.19 µm^{-1}.

The anisotropy fields H_{in} and H_{out} were derived fitting equations 4.3 and 4.4 using the SW stiffness derived above (Table 4.2). The results are shown in Table 4.3. In parenthesis the values extracted from the resonance frequency ($f_0(k_{SW}) \rightarrow 0$) derived from the whole range of wavectors. The error bars are calculated with the propagation of uncertainty theory [141], considering an error of 0.1MA/m in the spontaneous magnetisation, 0.05Å in the cobalt thickness, and from the error bars found from the fitting of the Stokes and anti-Stokes peaks of the BLS spectrum.

As it can be observed in Fig. 4.15 **a)** the interfacial MCA constant, K_s, decreases monotonously with the Pt content, similarly to the work of Shahbazi et al. [140]. The interfacial anisotropy of the $Au_{1-x}Pt_x$/Co/W(110) stack follows the Vegard's law:

$$K_{s,Au_{1-x}Pt_x/Co} = (1-x)K_{s,Au/Co} + xK_{s,Pt/Co} - K_{s,Co/W(110)}. \tag{4.14}$$

Due to the contribution of the two interfaces to the interfacial anisotropy, in order to determine the interfacial anisotropy $K_{s,Au/Co}$ and $K_{s,Pt/Co}$, we need to substract the contribution of the Co/W(110) interface. According to Fritzsche et al., the interfacial anisotropy of Co(0001)/W(110) ranges between 0.3-0.6 mJ/m^2 [116]. We will consider the most conservative case, 0.3 mJ/m^2. The linear fitting of the subtracted data (dots in Fig. 4.15 **a)**) results into $K_{s,Au/Co} = 1.11 \pm 0.1$ mJ/m^2 and $K_{s,Pt/Co}$ =0.73 ± 0.1 mJ/m^2. These values are in good agreement with those found in the literature [39; 142]. Note however, that our analysis considers the interfacial MCA anisotropy as the only source of MCA, neglecting other possible contributions such as bulk MCA

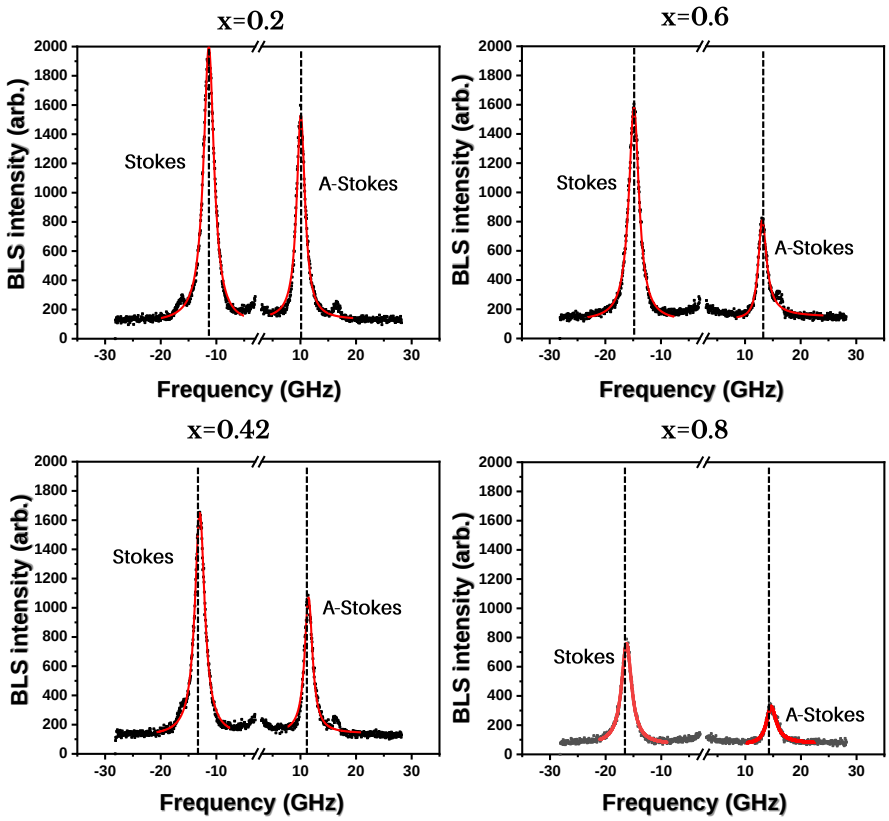

Figure 4.14: **Brillouin light scattering spectrum for the $Au_{1-x}Pt_x$/Co(0.78nm)/W(110) stack as function of the Au-to-Pt content x.** The black squares are experimental data while the solid red line is the fit of the peaks. An in-plane field of 0.32 T is applied along the in-plane easy axis direction, for k_{SW}=20.19 µm^{-1}.

and/or strain-induced anisotropy. It is interesting to note that these values are higher than those found for sputtered samples, stressing the enhancement of the interfacial anisotropy with a high quality interface as expected from Bruno's model [143]

A roughly constant value of K_{in} =61±30 kJ/m^3 is found for the in-plane anisotropy for all the Au-to-Pt compositions (Fig. 4.15 **b)**). This value is in good agreement with the one found by MOKE for a lower Co thickness and similar composition, but it is lower that the one found in literature [116] and in our previous work on Au/Co/W(110) [18]. This discrepancy may be explained by the presence of dislocations and defects as well as roughness, which may reduce the crystal elastic energy and therefore the magnetic in-plane anisotropy [143]. In conclusion, the in-plane anisotropy, which has a

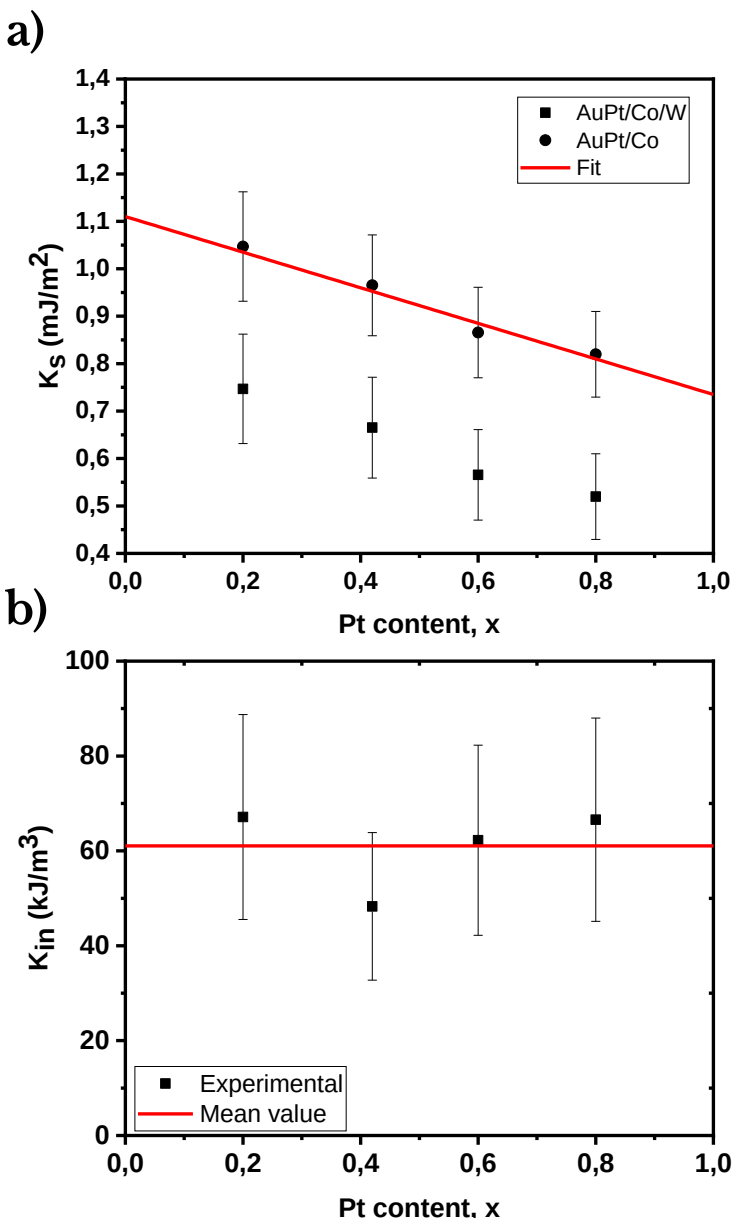

Figure 4.15: **Magnetic anisotropies as function of Pt content determined in the Damon-Eshbach configuration] a)** Interfacial magneto-crystalline anisotropy as function of Pt content: Squares represent the contribution of the two interfaces. Dots represent the contribution of the $Au_{1-x}Pt_x$ interface after substracting the Co/W(110) interface magnetocrystalline anisotropy from [116]. **b)** In-plane magnetic anisotropy, as function of Pt content. A mean value at 61 kJ/m^3 is found.

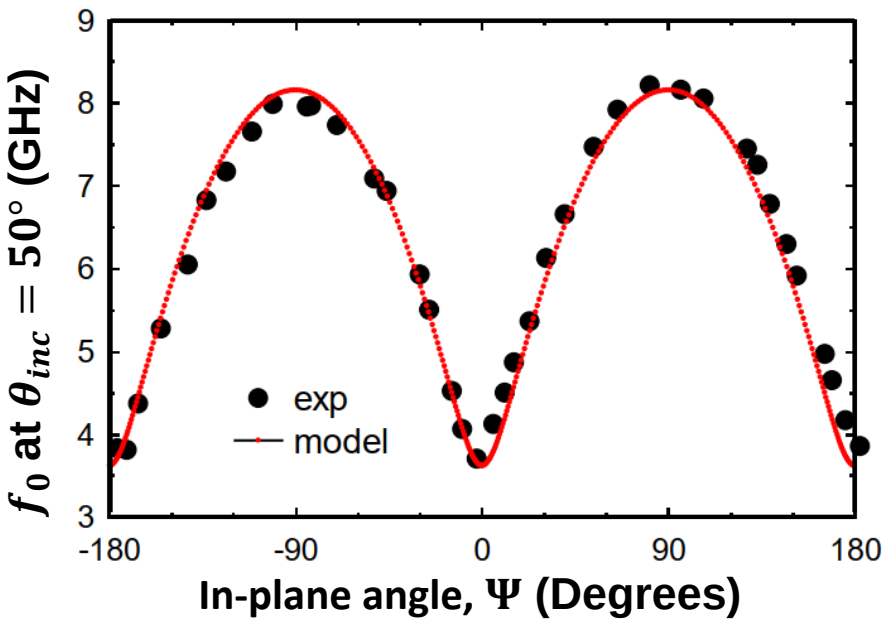

Figure 4.16: **Angular dependence of the symmetric component of the spin-wave frequency in the magnetostatic backward volume waves configuration.**

magnetoelastic origin, is Pt-and thickness-independent[3].

F.E. Neumann's principle (1885) states that *any symmetry of a material must also be possessed by any physical property of the material* [144]. This implies that the two-fold crystal symmetry along the z-axis that our Co layer possesses, must also be reflected in the magnetic properties, such as the magnetic anisotropy. .

Angular-dependence spectra in the BVW configuration were taken for the $Au_{0.58}Pt_{0.42}$/Co(0.78nm)/W(110) stack, keeping fixed the incident angle at 50°, and rotating the sample along its normal, Ψ. The in-plane angular dependence of the symmetric component, f_0 of the SW frequency, shows a clear two-fold symmetry (Fig. 4.16), with maximum and minimum frequencies located along the easy and hard-in plane axes, ($\Psi = 90°$ and $\Psi = 0, \pm 180$ °) respectively. The fit of this spectrum, results into K_{out} =22 kJ/m^3, and K_{in} =57 kJ/m^3, in agreement with the values found in the DE configuration.

A similar in-plane angular SW dispersion have been observed in other systems with a two-fold crystal symmetry such as in Fe(110)/Cu(110) [145] or Co (110)/Cu(110) [146].

[3]Needless to say, this is true only in the regime where the Co layer is strained, below 1.6 nm

4.3.6 | Néel-type DMI

The Néel and -Bloch -type DMI are determined by measuring the anti-symmetric component of the SW frequency,

$$\Delta f = |f_{\text{Stokes}}| - |f_{\text{Anti-Stokes}}| = \frac{2\gamma}{\pi}\frac{D}{M_s}k_{\text{SW}}, \tag{4.15}$$

with $\gamma = \frac{g\mu_B}{\hbar}$, being g the Lande factor, μ_B the Bohr magneton and $\hbar$ the reduced Planck's constant.

The x- and y- component of the DMI, D_x and D_y respectively, are addressed by measuring in the DE configuration, saturating the magnetisation along the two main in-plane directions. Two types of measurements are performed. First, we studied the sample region with $x = 0.42$ and t_{Co}=0.78 nm for different wavectors along the easy and hard axes (Fig. 4.17). Second, we performed our analysis for different content of Pt, for a single incident angle, θ_{inc}=60°, due to time limitations.

Figure 4.17 shows Δf as function of the SW wavector, revealing a positive Δf along both directions, implying a positive DMI i.e. a right-handed chirality along the easy and hard axes. The Δf *vs* k_{SW} shows a monotonous increase with two different slopes, revealing the presence of an anisotropic DMI, in line with previous works in Au/Co/W(110) [18].

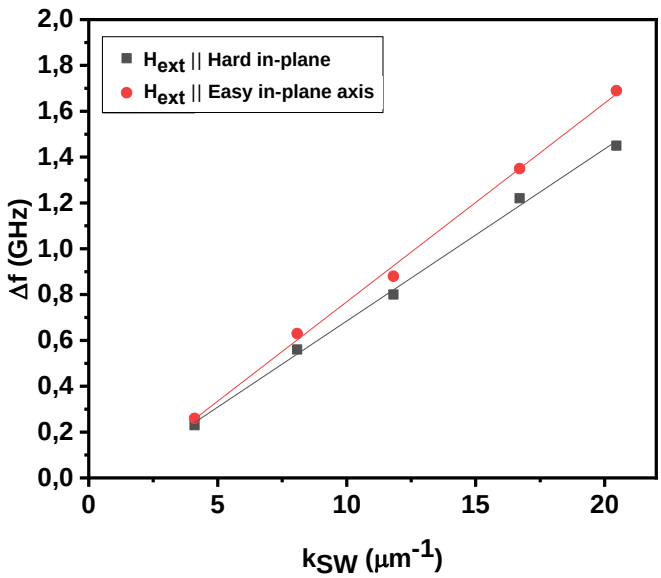

Figure 4.17: **Spin-wave frequency asymmetry as a function of the wavector along the two main in-plane directions measured in the Damon-Eshbach configuration for the $Au_{0.58}Pt_{0.42}$/ Co(0.78nm)/W(110) stack.**

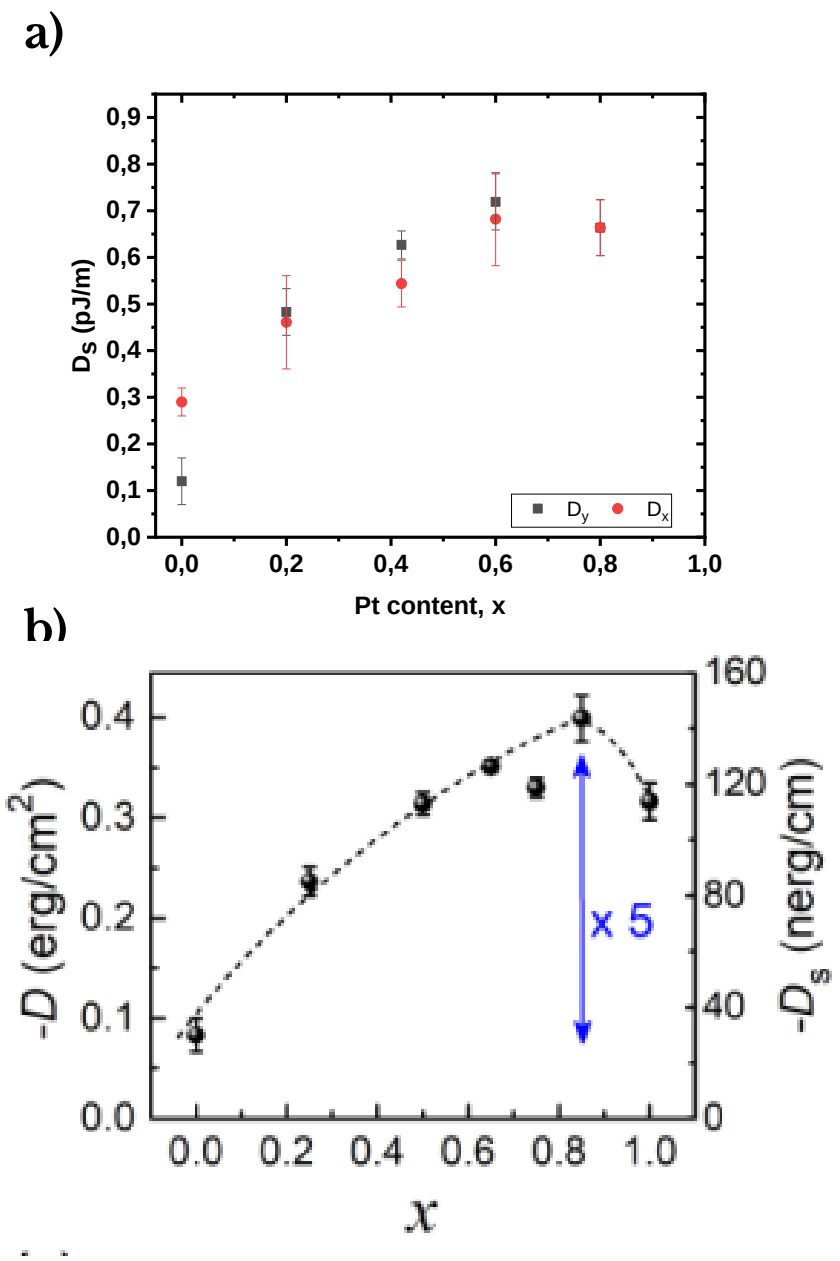

Figure 4.18: **Néel-type Dzyaloshinskii–Moriya interaction as function of the Pt content a)** Interfacial Dzyaloshinskii–Moriya interaction constants in [pJ/m] along the two main in-plane directions as function of the Pt content. The values for x=0, are taken from [18] **b)** Dzyaloshinskii–Moriya interaction constant as function of Pt content in MgO/Co/$Au_{1-x}Pt_x$ trilayers . Taken from [147].

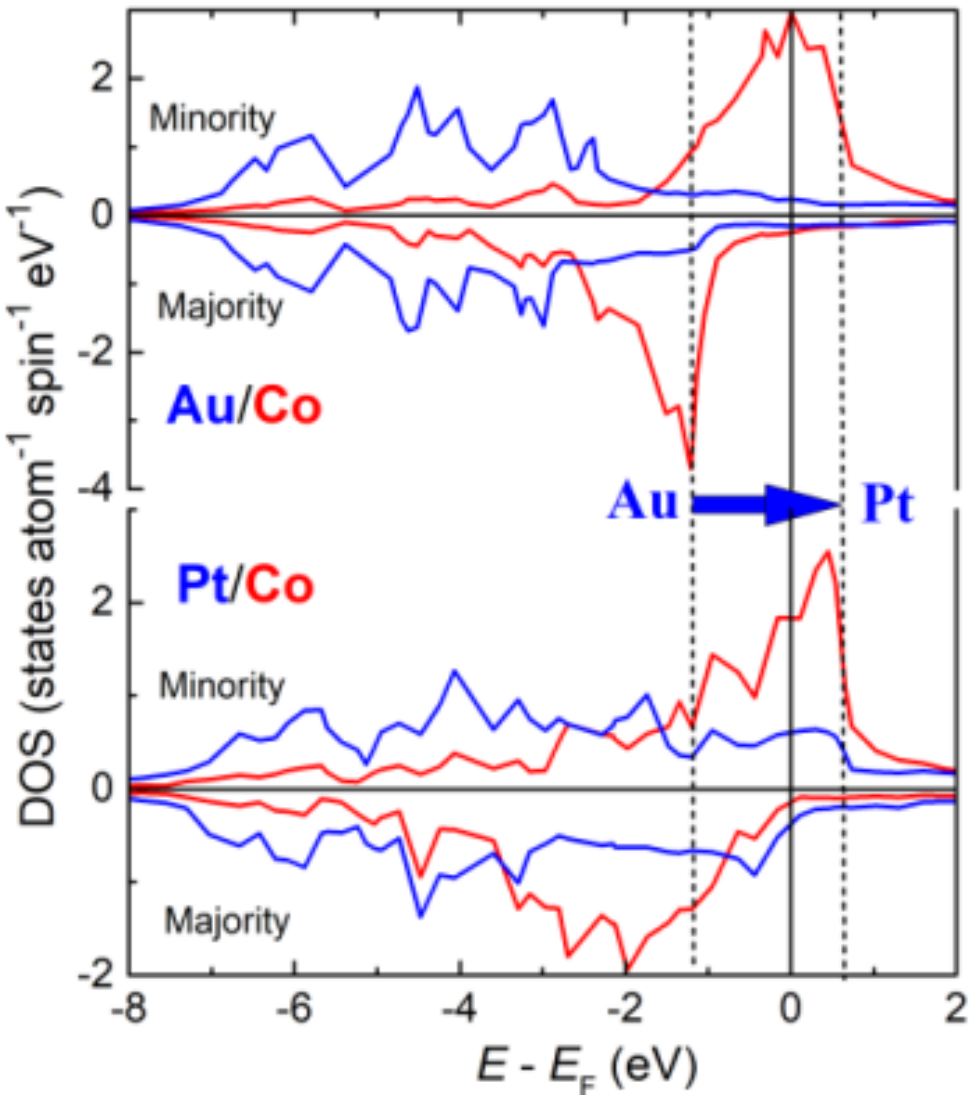

Figure 4.19: **Ab-initio calculations for Au/Co and Pt/Co**. Calculated local density of states for Au/Co (up) and Pt/Co (down) interfaces (blue for the density of states of Au and Pt, red for that of Co), highlighting a substantial shift of the 5d band from below to beyond Fermi energy as a function of the composition. The two dashed lines in refer to the top of the 5d bands of Au and Pt. Taken from [147]

The dependence of the DMI constants along the two main in-plane directions as a function of the Pt content is shown in Fig. 4.18 **a)**. Different features are revealed from the dependence of the DMI on the Pt content. For all the compositions, Δf is positive, implying a positive DMI i.e. a right-handed chirality. The DMI of trilayer systems is the

sum of the contributions from both the top and bottom Co interfaces. As reported by Ma et al, [148] the DMI at the Co/Au interface is negative, as is also the case for Co/Pt, and stronger than that of Co/W, which is positive. Therefore, in both Au/Co/W and Pt/Co/W trilayers the DMI at the two interfaces induces a positive DMI i.e. a right-handed chirality, as found experimentally.

Overall, while increasing the Pt content, the effective DMI strength along both directions increases up to $x = 0.6$, at which it reaches the maximum value, and above this composition, the DMI strength drops. A similar behaviour has been observed by Zhu et al. [147] for sputtered MgO/Co/$Au_{1-x}Pt_x$ trilayers (See Fig. 4.18 **b)**). By means of ab-initio calculations they explain this finding by the linear shift of the *5d* bands of the $Au_{1-x}Pt_x$ and the minority *3d* band of Co while increasing the Pt composition. This results into an enhancement of the *5d-3d* hybridisation mainly due to the shift of the *5d* band of $Au_{1-x}Pt_x$ which is maximum at the composition at which the peak of density of *5d* states is approximately at the Fermi energy of the Co layer. Above this composition, the *5d* band is shifted from the Fermi energy of Co, and the hybridisation is not maximum, resulting into a drop of the DMI. In their case, they observed this maximum at $x = 0.8$, while we observed it at $x = 0.6$. Yet, this difference may be explained by the fact that our Co layer is strained as biaxial strain has revealed to modify the Fermi

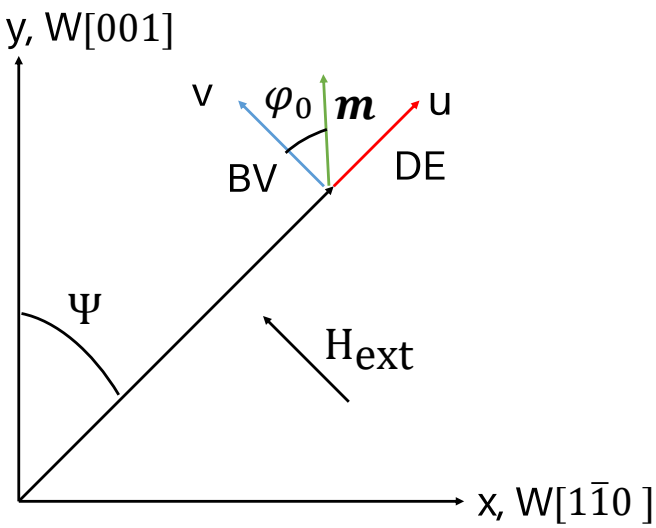

Figure 4.20: **Brillouin light scattering geometry scheme used in the backward-volume configuration on the W(110) plane**. The magnetic field is applied parallel to the spin-wave propagation plane, **v** direction. If the field is not strong enough, an angle φ_0 between the magnetisation and the field direction arises.

energy [149]

Like the DMI strength, the anisotropic DMI also varies with the content of Pt. While for x=0 (Pure Au), the larger DMI is along the easy in-plane axis (x-axis), with a strong anisotropy, the larger value is along the hard in-plane axis (y-axis) for large Pt content. This suggests that the Pt/Co DMI is larger along the hard in-plane axis, than along the easy in-plane axis. Therefore, when increasing the Pt composition, the DMI along the hard in-plane axis increases faster than along the in-plane easy axis, as the DMI strength for Pt/Co is larger than for Au/Co [22]. Yet, above x=0.6, at which the DMI strength is maximum, the DMI becomes isotropic. For the moment we cannot explain the reason of this behaviour.

4.3.7 | Bloch-type DMI

As mentioned before, the Bloch-type DMI only arises when the DMI is anisotropic. In order to probe this DMI component, the measurements need to be sensitive to SW propagating parallel to the magnetisation direction, i.e. along the vz-plane (Fig. 4.10). This is achieved by measuring in the BVW geometry, for the zone with a Pt composition

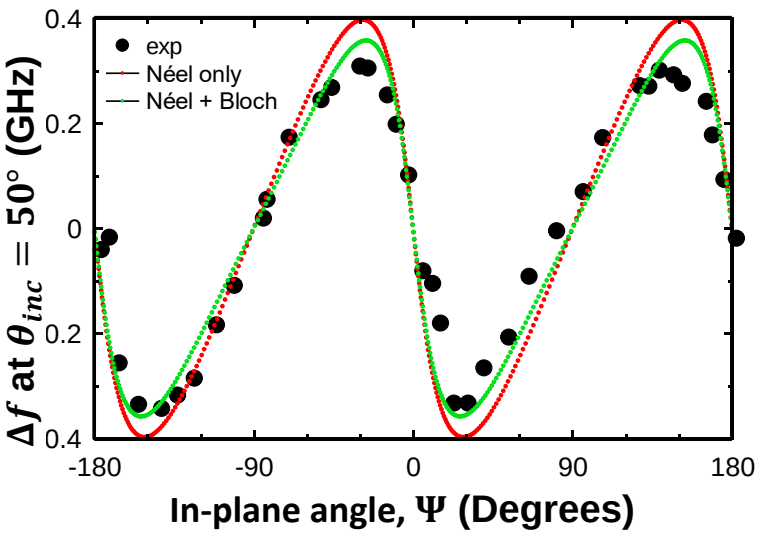

Figure 4.21: **Angular dependence of the spin-wave frequency asymmetry in the magnetostatic backward volume waves configuration**. Dots represent the experimental data, while the red and green solid lines represent the expected analytical dependence when the Néel Dzyaloshinskii–Moriya interaction and the Néel+Bloch-type Dzyaloshinskii–Moriya interaction are considered.

of x=0.42 and a Co thickness of 0.78 nm, which shows the larger anisotropic DMI. The incident angle, θ_{inc} is kept fixed to 50°, while the sample is rotated around its normal,Ψ.

The asymmetric frequency component, Δf of the SW (Eq. 4.15) as a function of Ψ is shown in Fig. 4.21. A non-perfect sinusoidal shape is observed. This is due to the fact that the available in-plane field, $B_{ext,in}$ ≈200 mT is less than twice the anisotropy field, leaving an angle between the magnetisation direction and the field direction, φ_0 (See Fig. 4.20). Consequently, the measured DMI responsible of the Δf, is given by:

$$D = \mathcal{D}_{\text{Néel}} \sin \varphi_0 + \mathcal{D}_{\text{Bloch}} \cos \varphi_0. \tag{4.16}$$

The measured Δf, shows an almost zero frequency when $\Psi = \pm 90°$ (Easy in-plane axis, see Fig. 4.16), and a small, but non-completely zero Δf, when the field is aligned along the hard in-plane axis, Ψ =0°. Furthermore, the maximum asymmetry is observed at $\Psi \approx 30°$. Note that this maximum is not observed exactly at $\Psi = 45°$, as expected, because the in-plane field is not strong enough. Along this direction, the contribution of both DMI types is maximum. In Fig. 4.21, the analytical curve considering either only the Néel- or the Néel- and Bloch-type DMI are shown. When only the Néel-type DMI is considered (red curve), the values at $\Psi \approx 30°$ are about 0.07 GHz higher than the experimental ones. When in addition to the Néel-type DMI, the Bloch-type is considered (green curve) the experimental values at $\Psi \approx \pm 30°$ are well reproduced. In summary, even if small, the maximum Δf observed at $\Psi \approx 30°$ cannot be explained uniquely by the Néel-type DMI, and the Bloch-type DMI is necessary to explain the experimental data.

4.3.8 | Summary

Using Brillouin light scattering (BLS), we have been able to determine the magnetic parameters of the $Au_{1-x}Pt_x$/Co/W(110) stack as function of the Pt content. In particular, we have focused on the x=0.42 composition, where the anisotropic DMI is the largest. For this composition the magnetic exchange is found to be around 16 pJ in agreement with the work of Metaxas et al. [138], and slightly larger along the hard in-plane axis, as expected from an atomistic framework [139]. Yet, the small difference as well as the amplitude of the error bars, do not allow us to determine whether the in-plane magnetic exchange it is really anisotropic.

Furthermore, the interfacial anisotropy is found to follow Vegard's law, decreasing monotonously as the Pt content increases. From the linear fit of the K_s as func-

tion of the Pt content, the pure interfacial MCA anisotropies for Au/Co/W(110) and Pt/Co/W(110) were derived, being in agreement with the literature [39].

On the other hand, the in-plane anisotropy shows a two-fold anisotropy, as expected from the Neuman's principle, but with a value slightly lower than in previous works [18; 116]. This value, fixed around $K_{in} \approx 60\,kJ/m^3$ is independent of the Pt content, consistent with the findings of GXRD where the Co in-plane strain was not modified by the Pt content of the capping layer.

Contrary to the interfacial MCA, the Néel-type DMI does not follow Vegard's law, as it increases non-monotonously up to a maximum at x=0.6, but it drops above. This is in agreement with the results found by [147], explained by the linear variation of the *5d* orbitals of the $Au_{1-x}Pt_x$ capping layer, which results into a variation of the orbital hybridisation as a function of the Pt composition, with its maximum value located around at x=0.8 in their case. We associate this discrepancy to the reduction of the Fermi energy in our Co layer due to the increasing of the unit cell volume. The anisotropy of the Néel-type DMI is also affected by the different composition of AuPt. While for pure Au the largest DMI is along the easy-axis, when introducing a significant content of Pt, the largest DMI is along the hard in-plane axis. This indicates that the DMI induced by the Pt atoms, is perpendicular in direction, but not in sign, with respect to the one given by Au. Finally, by measuring in the BVW geometry, we revealed the presence of the Bloch-type DMI due to the anisotropic Néel-type DMI.

4.4 | Field-driven domain-wall motion

4.4.1 | Introduction

In this section the field-driven DW motion under an out-of-plane magnetic field for different Au-to-Pt compositions of the $Au_{0.1-x}Pt_x/Co(0.6nm)/W(110)$ stacks will be presented.

As largely discussed in Chapter 3, the DW motion in systems with DMI is strongly governed by the $H_{DMI} = \frac{D}{M_s\Delta}$ effective field [61] which, from the results of the BLS measurements is expected to increase with increasing the Pt content of the $Au_{1-x}Pt_x$ capping layer due to the increasing of the DMI micromagnetic constant. Note however that as the MCA constant decreases, the DW parameter increases, leading to a non-linear increase of H_{DMI}. The field-driven DW motion due to an out-of-plane magnetic field, $\mu_0 H_z$ measured by MOKE microscopy for three $Au_{1-x}Pt_x$/Co/W(110) stacks with $x = 0, 0.2$ and 0.33, are compared in Fig. 4.22. The field-driven velocity curves show very different features. These will be compared with the 1D analytical model and 2D micromagnetic simulations using the micromagnetic parameters derived by BLS and presented in Table 4.4.

Table 4.4: **Micromagnetic parameters used for the one-dimensional and two-dimensional simulations calculations.** An exchange stiffness, A=16 pJ/m, a spontaneous magnetisation, M_s=1.15 MA/m, K_{in}=60 kJm^{-3}, a Gilbert damping, $\alpha = 0.3$ and the experimental Co thickness, t_{FM} =0.6 nm have been considered for the three stacks. The Bloch DW parameter is given by $\Delta = \sqrt{\frac{A}{K_{out} - K_{in}}}$. The values for $x = 0$ are taken from [18].

	K_s [mJm^{-2}]	$D_{s,x}$ [pJm^{-1}]	$D_{s,y}$ [pJm^{-1}]	Δ [nm]	$\mu_0 H_{DMI,x}$ [mT]
x=0	0.81	0.29	0.12	5.9	71
x=0.2	0.75	0.46	0.43	6.7	100
x=0.33	0.7	0.57	0.5	7.6	110

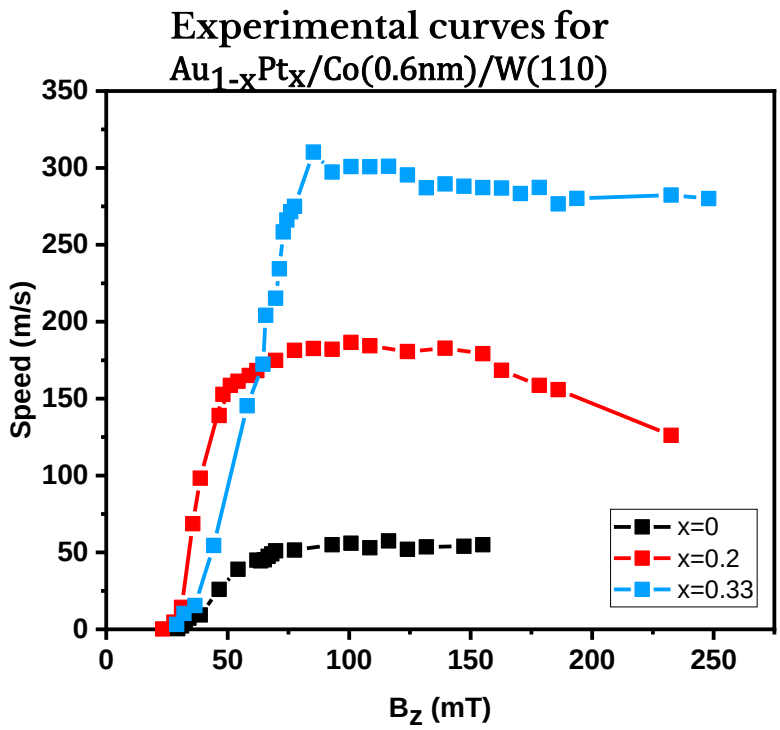

Figure 4.22: **Field-driven domain wall motion for different Au-to-Pt compositions of the $Au_{1-x}Pt_x$/Co(0.6nm)/W(110) stacks**. Blue: x=0.33. Red: x=0.2. Black: x=0.

4.4.2 | Experiments: DW vs B_z

In the following, we will present the experimental field-driven DW motion investigated with magneto-optical Kerr effect (MOKE) in the polar configuration. In order to address the DW dynamics in the flow regime, we have used home-made microcoils, which allow us to apply very strong magnetic fields, up to 600 mT with very short pulses, typically around 20 ns. The technical description of such microcoils is extensively presented in [150; 151].

In a MOKE microscope, samples with different magnetisation with respect to the propagation direction of the linearly polarised light give rise to different Kerr rotations that are recorded as different intensities by the charge-coupled device camera. This difference results into a magnetic contrast in the Kerr images. At the beginning of our measurements, the sample is magnetically saturated either *up* or *down* along the out-of-plane easy-axis. Next, by the application of an opposite magnetic field pulse, a magnetic domain is nucleated. We call a *(down/up)* DW, a DW separating from left to right two domains with *up(down)*(*down(up)*) magnetisation, respectively. Figure 4.23

shows an example of the experimental differential Kerr images obtained for the three stacks. The dark (bright) contrast represents the DW displacement under the application of an out-of-plane magnetic field. The experimental expansion of a bubble domain are compared with the ones predicted by 2D micromagnetic simulations under a $B_z = 100\,\mathrm{mT}$ applied during 8 ns. In line with the micromagnetic simulations, the DW displacements is *isotropic* for Au/Co/W(110) and $Au_{0.8}Pt_{0.2}$/Co/W(110), but anisotropic for $Au_{0.67}Pt_{0.33}$/Co/W(110) where the DW displaces faster along the in-plane easy-axis direction. Note that this anisotropic displacement increases with the strength of the out-of-plane field.

Figures 4.25, 4.26 and 4.27 show the DW velocity *vs* B_z field obtained for the three samples. The DW velocities were obtained as the ratio of the DW displacement along the x-direction (easy axis) to the duration of the B_z field (typically 30 ns). Prior to the discussion of these curves we will introduce the modified 1D model used for our system accounting for an uniaxial in-plane magnetic anisotropy, as well as details on the 2D micromagnetic simulations. We will use both results to discuss the experimental curves.

1D model and 2D micromagnetic simulations

In order to account for the effect of the in-plane anisotropy in the 1D model presented in Chapter 3 3.1.3, we need to modify the $q - \varphi$ model. This can be easily done by noticing that the in-plane anisotropy energy density has the same form as the demagnetising DW anisotropy energy density. Yet, due to the dependence of this term on φ, the DW parameter cannot be considered as a static quantity. Therefore, the equations of motion under an out-of-plane magnetic field H_z, and an in-plane magnetic field, H_x, are given by:

$$\dot{q}(t) = \frac{\gamma_0 \Delta(t)}{\alpha} H_z - \frac{\Delta(t)}{\alpha}\dot{\varphi}(t), \tag{4.17a}$$

$$\dot{\varphi}(t) = \frac{\gamma_0}{1+\alpha^2}\left[H_z - \alpha \sin\varphi(t)\left(\cos\varphi(t)\left(H_{\mathrm{in}} - \frac{2t_{\mathrm{FM}}\ln 2}{\mu_0 M_s \pi \Delta(t)} K_d\right) + \frac{\pi}{2}\left(H_x + \frac{D}{M_s \Delta(t)}\right)\right)\right], \tag{4.17b}$$

$$\dot{\Delta}(t) = \frac{12\gamma}{\alpha M_s \pi^2}\left[\frac{A}{\Delta(t)} - \Delta(t)(K_{\mathrm{out}} - K_{\mathrm{in}}\cos^2\varphi(t)) + \mu_0 M_s \Delta(t)\frac{\pi}{2} H_x \cos\varphi(t))\right], \tag{4.17c}$$

where $H_{\mathrm{in}} = \dfrac{2K_{\mathrm{in}}}{\mu_0 M_s}$ is the effective field associated with the in-plane anisotropy.

Figure 4.24 shows the DW speed at the Walker field, v_W, for a field-driven DW motion along the easy-axis as function of the in-plane anisotropy constant, K_{in}, for two sample compositions, $x = 0$ and $x = 0.33$ using the values of Table 4.4 by solving

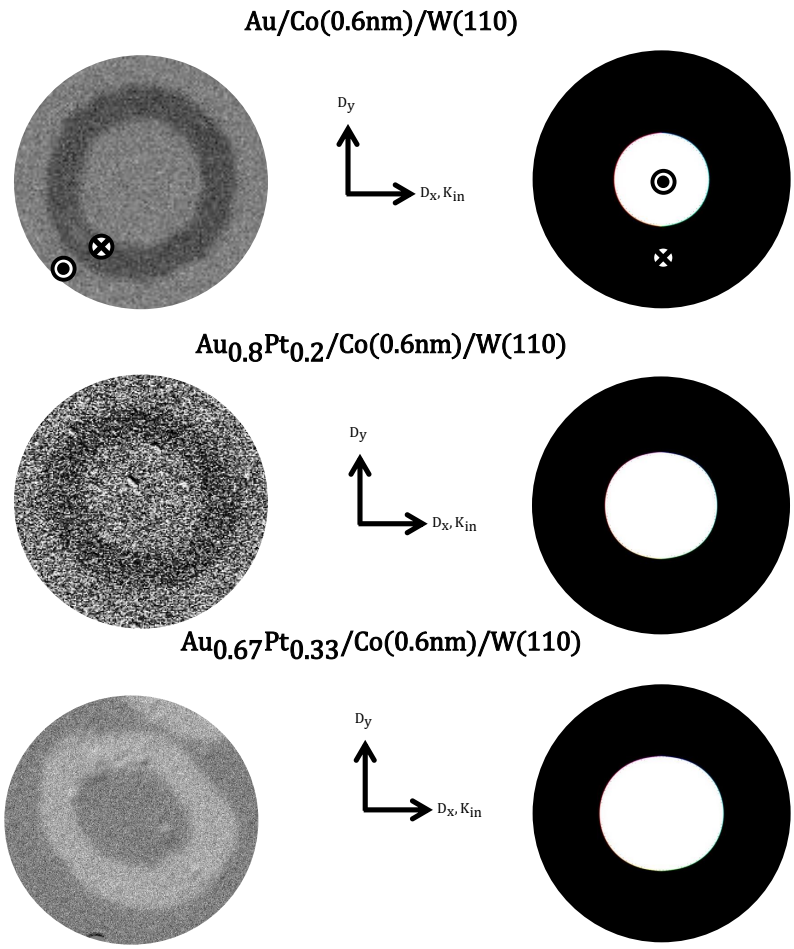

Figure 4.23: **Domain shape for different Au-to-Pt content of the $Au_{1-x}Pt_x$/Co(0.6nm)/W(110) stack.** Left: Differential Kerr images. Right: Final micromagnetic simulated state of a bubble domain expansion obtained after the application of a B_z pulse of strength 100 mT and duration 8 ns. The initial state was an up bubble domain.

numerically Eq. 4.17. Overall, the presence of the in-plane anisotropy increases the Walker field. Consequently, the increasing of the Walker field results into an increasing of the Walker velocity.

Micromagnetic 2D simulations are performed using the software package Mumax^3 [152; 153] in a system of 512 × 512 × 1 rectangular cells of size 2 nm×2 nm× 0.6 nm, with only one cell across the film thickness, so that the magnetisation is assumed to be uniform along this direction as the film thickness is much lower than the exchange length. In the simulations, a Néel DW initialised into the strip is first relaxed and next

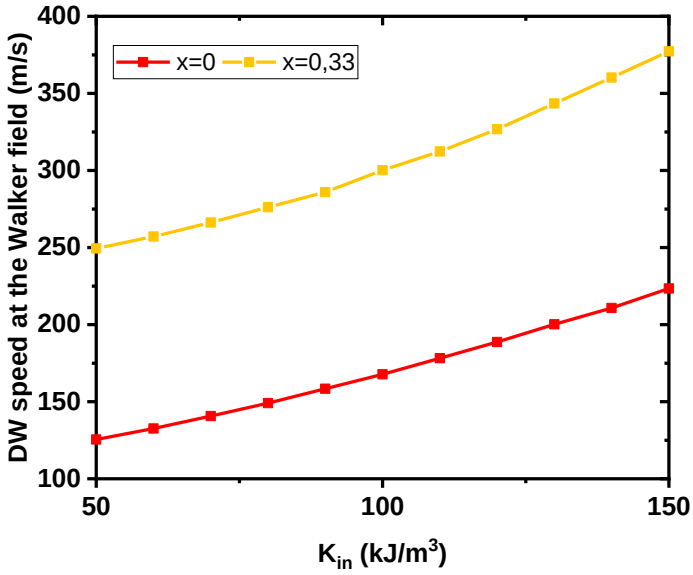

Figure 4.24: **Calculated Walker velocity as function of the in-plane anisotropy.** Two compositions are considered: x=0 and x=0.33.

is driven by the action of a magnetic field normal to the plane, within a 1 µm^2 moving frame window (so as to keep the DW in its center). A 1 µm width is chosen as it allows the establishing 2D effects, mimicking the experimental conditions. For convenience defects and temperature are neglected.

Discussion

The experimental curves shown in Fig. 4.25, 4.26 and 4.27 for Au/Co(0.6nm)/W(110), $Au_{0.8}Pt_{0.2}$/Co(0.6nm)/W(110) and $Au_{0.67}Pt_{0.33}$/Co(0.6nm)/W(110) respectively, show different features. The three Au-to-Pt compositions, show a similar depinning field, about 50 mT, and an increase of the maximum DW velocity as the Pt content increases. The increasing of the maximum velocity is in line with the increase of the $\mu_0 H_{\mathrm{DMI}}$ field.

- **Au/Co(0.6nm)/W(110)**. The experimental data (Fig. 4.25) shows a DW speed saturation at about 55 m/s for large fields. The 1D model and the 2D simulations predict a drop of the DW velocity immediately after the Walker field, which occurs for a B_{W} ≈35 mT. This is below the measured depinning field and cannot be observed. The saturation velocity does not correspond with the expected Walker velocity (predicted to be around 120 m/s), and therefore cannot be associated to the velocity plateau due to 2D effects observed for a systems with large DMI. Indeed, the experimental saturation velocity corresponds very well with

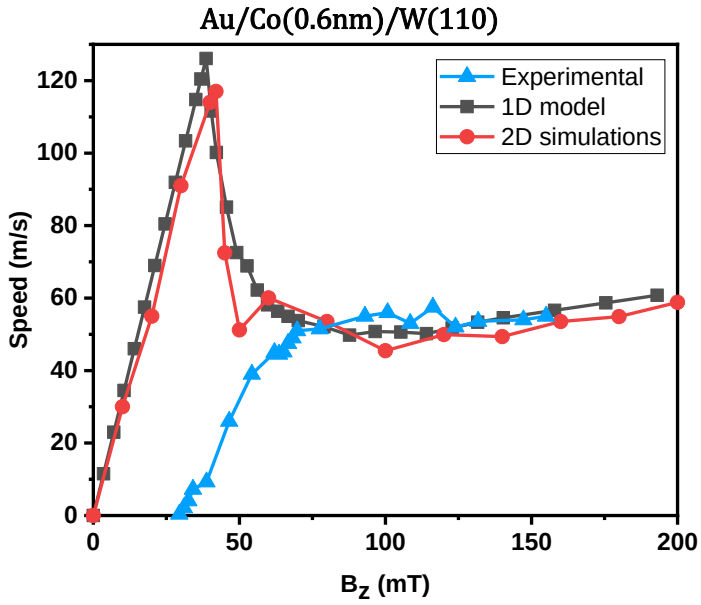

Figure 4.25: **Field-driven domain wall motion for Au/Co(0.6nm)/W(110).** Blue triangles: Experimental data. Black squares: 1D model. Red circles: 2D micromagnetic simulations.

the Slonczewski velocity (i.e. the minimum velocity in the regime with negative mobility). The agreement between the Slonczewski velocity and the experimental velocity indicates that the DMI constant measured with BLS is reliable.

- **$Au_{0.8}Pt_{0.2}$/Co(0.6nm)/W(110).** The experimental data (Fig. 4.26) shows a DW speed saturation of about 175 ms^{-1}. The Walker field found by the 1D model and 2D micromagnetic simulations (around $B_W \approx 45$ mT) is situated below the end of the thermally activated regime, so that the steady flow regime is not observable. However, the measured plateau velocity fits remarkably well with the Walker velocity predicted by the 1D model and the plateau velocity after the Walker field found by 2D micromagnetic simulations (around $v_W \approx 200\,ms^{-1}$) confirming the reliability of the DMI value found by BLS. The small difference between the experimental and calculated velocity may be explained by the error bars in the interfacial MCA constant or the in-plane anisotropy constant. The saturation of the DW velocity is then due to 2D effects, as shown by the results of the micromagnetic simulations. The extension of the experimental velocity plateau is larger than that predicted by micromagnetic simulations. The experimental end of the

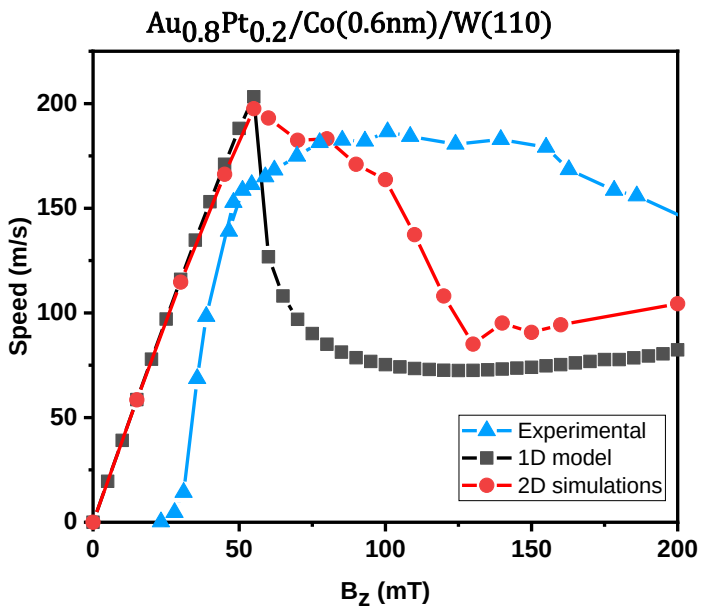

Figure 4.26: **Field-driven domain wall motion for $Au_{0.8}Pt_{0.2}$/Co(0.6nm)/W(110).** Blue triangles: Experimental data. Black squares: 1D model. Red circle: 2D micromagnetic simulations.

plateau is observed at around 150 mT while micromagnetic simulations predict it to be around 100 mT. This difference, already found in [74] may be attributed to the presence of defects, or to a larger value of the damping parameter. Interestingly, a decay on the plateau velocity it is observed for fields larger than 150 mT. Yet, due to the high nucleation for larger fields, we could not confirm if the velocity decays to the one predicted by the 1D model.

- **$Au_{0.67}Pt_{0.33}$/Co(0.6nm)/W(110).** The experimental data show a DW speed saturation about 300 ms^{-1}. The Walker field found by the 1D model and 2D micromagnetic simulations (around $B_W \approx$50 mT) is situated below the end of the thermally activated regime, so that the steady flow regime is not observable. However, as for the previous stack, the measured plateau velocity is in good agreement with the calculated Walker velocity predicted by the 1D model and 2D micromagnetic simulations (around $v_W \approx$250 ms^{-1}), and the presence of a plateau velocity can be explained by 2D effects. The small difference between the experimental and calculated velocity may be explained by the error bars in the interfacial MCA constant or the in-plane anisotropy constant.

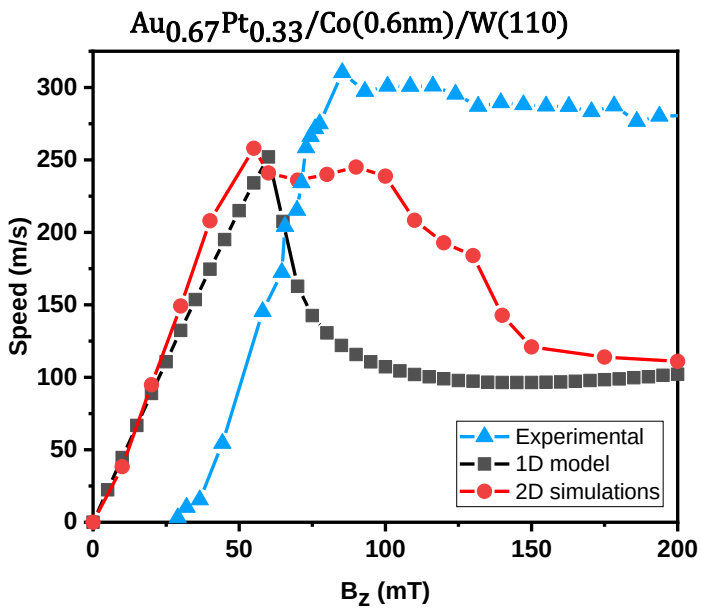

Figure 4.27: **Field-driven domain wall motion for $Au_{0.67}Pt_{0.33}$/Co(0.6nm)/W(110).** Blue triangles: Experimental data. Black squares: 1D model. Red circle: 2D micromagnetic simulations.

In conclusion, the comparison between measured and calculated DW speeds curves validate the correctness of the magnetic parameters (D, K_{in}, K_{out}) measured by BLS. In the sample $x = 0$, Au/Co(0.6nm)/W(110), the weakness of the DMI strength is such that the DMI does not induce 2D effects after the Walker field, and the saturation of the velocity at large field is associated to the negative mobility velocity minimum the so-called Slonczewski velocity . The Walker velocity increases in the samples x=0.2 and x=0.33, $Au_{0.8}Pt_{0.2}$/Co(0.6nm)/W(110) and $Au_{0.67}Pt_{0.33}$/Co(0.6nm)/W(110) respectively, due to the increase of the DMI. In these two samples, 2D effects become visible, as the DW velocity saturates at the Walker velocity calculated by 2D micromagnetic simulations.

4.4.3 | DW motion vs B_z with B_x

Figure 4.28 shows the field-driven DW motion under a fixed out-of-plane field of $B_z \approx 60$ mT, when a static in-plane field is applied along the two main in-plane directions of the Au/Co(0.6nm)/W(110) stack.

The data reveal the right handed chirality of the DW along the two directions, in

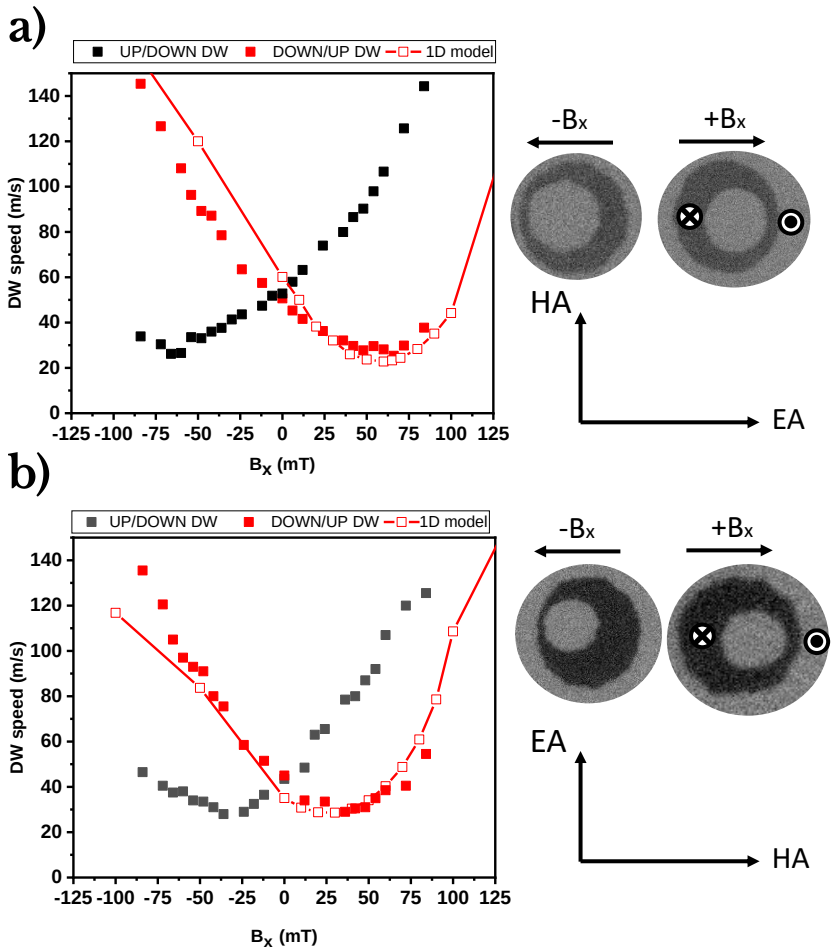

Figure 4.28: **Field-driven domain wall motion for Au/Co(0.6nm)/W(110) under an static in-plane field.** Black squares: Up/down domain wall. Red squares: Down/up domain wall. Empty red squares: one-dimensional model. The domain walls are driven by 20 ns long pulses B_z of 60 mT, under an static in-plane field applied along the **a)** easy and **b)** hard in-plane axis. In the differential Kerr images, the dark contrast represents the displacement of the domain walls during the application of the out-of-plane magnetic field pulse.

agreement with the results of the BLS measurements [18]. Since DWs with their magnetisation parallel to the in-plane field are expected to move faster the direction of the DW magnetisation, and therefore their chirality can be derived from the MOKE images.

For a given in-plane field, a minimum velocity is observed. As discussed in Chapter 3, this minimum velocity occurs when $H_x = -H_{DMI}$. The value of $B_{x,min}$ is different

along the two directions as expected from the presence of the in-plane anisotropy which modifies the DW parameter and the anisotropic DMI. From the fitting of the minimum with a second order polynomial, we derive $B_{\mathrm{min,EA}} = 61\,\mathrm{mT}$ and $B_{\mathrm{min,HA}}$=36 mT which are within 5% agreement with the theoretical value using the values derived by BLS, $B_{\mathrm{min,EA}} = 71\,\mathrm{mT}$ and $B_{\mathrm{min,HA}}$=31 mT.

In Fig. 4.28, the experimental curves are compared with the results of the 1D model, using the magnetic parameters reported in Table 4.28. A remarkable agreement is found between the two curves, calculated and measured curves, validating the validity of our models and of all the experimental magnetic parameters.

Note that we could not carry out the same experiment for the $Au_{0.8}Pt_{0.2}/Co/W(110)$ and $Au_{0.67}Pt_{0.33}/Co/W(110)$ stacks as the smaller MCA leads to the nucleation of a large number of nucleated domains as soon as an in-plane field is applied.

4.4.4 | Summary

Using magneto-optical Kerr microscopy in the polar configuration, we have investigated the field-driven DW motion of the $Au_{1-x}Pt_x/Co/W(110)$ stack.

The field-driven DW motion of the $Au/Co(0.6nm)/W(110)$ reveals an *apparent* saturation velocity, showing a good agreement with the 1D and 2D calculations, revealing that indeed it corresponds with the Slonczewski velocity. The investigation under a static in-plane field along the two main in-plane directions jointly with the 1D model allows us to determine the DMI effective field along the two main in-plane directions, which is in good agreement with that calculated with the values found by BLS [18].

The field-driven DW motion of the $Au_{0.85}Pt_{0.15}/Co/W(110)$ and $Au_{0.67}Pt_{0.33}/Co/W(110)$ reveals a saturation velocity increase with the Pt content. By means of the 1D and 2D model, it is shown that the end of the velocity plateau occurs indeed at a higher field than the end of the thermally activated regime. Furthermore, the maximum velocity predicted by the 1D and 2D calculations using the values of Table 4.4 found by BLS fits remarkably well with the experimental one.

5

Magnetic textures: $Au_{1-x}Pt_x$/Co/W(110)

Contents

5.1 Imaging the domain and domain wall structure **96**
5.1.1 XMCD 96
5.1.2 PEEM 97
5.1.3 XMCD-PEEM 98
5.2 Stripe domains in $Au_{1-x}Pt_x$/Co(t_{Co})/W(110) **100**
5.2.1 One-dimensional model 100
5.2.2 Observation by Kerr and XMCD-PEEM 104
5.2.3 Summary 110
5.3 Skyrmions **111**
5.3.1 Introduction 111
5.3.2 Observation by XMCD-PEEM 111
5.3.3 Why an elliptical shape? 112
5.4 Merons **118**
5.4.1 Introduction 118
5.4.2 Observation by XMCD-PEEM 120
5.4.3 Stabilisation of merons 124

5.1 | Imaging the domain and domain wall structure

The domain and DW internal structure in our $Au_{1-x}Pt_x/Co/W(110)$ stack were studied by x-ray magnetic circular dichroism coupled with photoemission electron microscopy. Due to the specificity of this technique we will review it in the next subsection.

5.1.1 | XMCD

X-ray magnetic circular dichroism (XMCD) is the difference between the absorption of left and right circularly polarised x-ray photons by a magnetic material. The incoming x-rays, whose energy is tuned to an absorption edge of the studied material, is absorbed by the magnetic material, inducing an electronic transition from the core level to the valence band. Hence, the variation of the x-ray energy induces different electronic transitions and consequently different elements and magnetic properties can be probed. XMCD experiments are performed with synchrotron radiation as it produces a monochromatic soft x-ray light with a high brilliance whose polarisation can be tuned between left, right or linear.

Figure 5.1 represents schematically the photon absorption process. The photon is

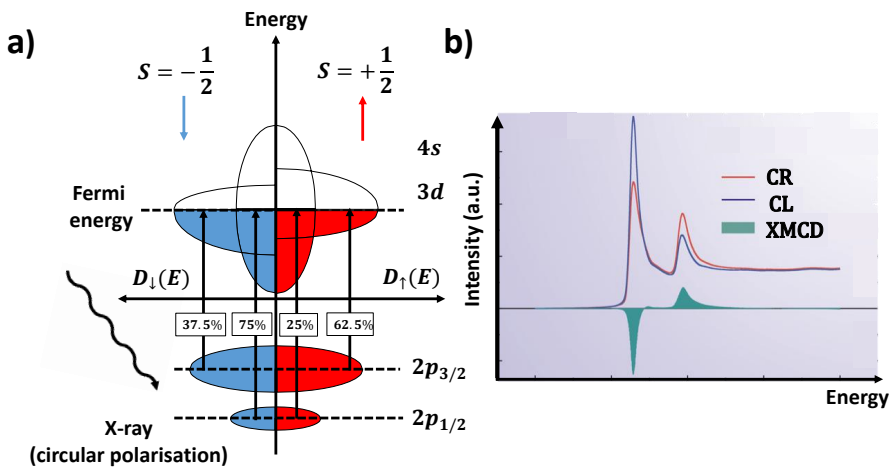

Figure 5.1: **X-ray magnetic circular dichroism working principle**. **a)** Electronic transitions induced by the absorption of an x-ray photon with circular polarisation at L_3 and L_2 edges, corresponding respectively to $2p_{3/2} \longrightarrow 3d$ and $2p_{1/2} \longrightarrow 3d$ electronic transitions, for a ferromagnetic transition metal. **b)** Typical absorption and x-ray magnetic circular dichroism spectrum for a ferromagnetic transition metal.

absorbed by an atom, leading to the transition of an electron from a core level to an empty state (just above the Fermi level when the energy of the absorbed photon is just above the binding energy for the electron). For circularly polarised photons, their angular momentum is also transferred to the atom upon absorption (angular momentum conservation). Through the SOC, the probability to excite spin-up or -down polarised electrons is different at the L_3 and L_2 edge. In ferromagnetic materials such as Co, magnetism is caused by the uneven occupation of the $3d$ and $4s$ spin-up and spin-down electronic bands [33]. Hence, the absorption of the x-ray photon for a given electronic transition is different for a given polarisation. In particular for $3d$ metals, the absorption edges exhibiting the largest XMCD are the L_3 and L_2, corresponding respectively to $2p_{3/2} \longrightarrow 3d$ and $2p_{1/2} \longrightarrow 3d$ electronic transitions. It can be shown that at the L_3 and L_2 edges, a photon with left-circular polarisation excites 62.5% and 25% *up* spin electrons and 37.5% and 75% *down* spin electrons respectively [154]. For the right circular polarisation, the photon carries an opposite angular momentum and the absorption probabilities are opposite to those of the left-circular case. For Co, the L_3 and L_2 energies are respectively 779 eV and 794 eV. Figure 5.1 **b)**, shows an example of XMCD absorption process. The XMCD spectrum is calculated as the difference between the absorption of left and right circular polarisation for a particular absorption edge, and allows to determine the magnetisation direction of the sample.

5.1.2 | PEEM

Photoemission electron microscopy (PEEM) working principle is based on the collection of the secondary electrons generated by an initial Auger process: First, the x-ray photon is absorbed by the magnetic material, exciting an electron from the core level to an excited state (e.g. $2p_{3/2} \longrightarrow 3d$ for the L_3 edge). This creates an empty state which is filled by an electron from an intermediate state, located between the core energy level and the Fermi energy. Due to energy conservation, an electron from the same intermediate state is excited above the Fermi energy, creating a cascade of low-energy electrons, some of which have enough kinetic energy to escape from the sample and be processed by the different electron-optic components before reaching an electron-sensitive screen. Since all the secondary electrons of a given area are collected simultaneously, and originate from a shallow layer, this is a full-field technique with surface sensitivity.

5.1.3 | XMCD-PEEM

When combining both XMCD and PEEM, an hybrid technique arises: X-ray magnetic circular dichroism photoemission electron microscopy (XMCD-PEEM). The combination of XMCD and PEEM allows the reconstruction of the local spin density and, for a magnetic material, an image of the local magnetisation [9; 155]. A sketch of the XMCD-PEEM microscopy is shown in Fig. 5.2.

Due to surface-sensitivity of XMCD-PEEM, if thick capping layers are present, it may be impossible to the secondary electrons from the magnetic layer to escape, reducing significantly the obtained intensity. Conversely, if the sample is not capped but a thick oxidation layer has formed, this can reduce the magnetic contrast dramatically.

During the preparation of the nanopatterned structures, the etching process was calibrated in order to remove all the titanium (used as a hard mask) on top of the nanopatterned structures and to leave a continuous film of tungsten in order to ensure an electrical conduction between the nanopatterned structures. A mistake in the calibration may result in a remaining titanium layer (reducing the XMCD signal), or the removal of all the tungsten layer, causing the sample charging as the sapphire substrate is insulating.

Technical details

All the results shown in this manuscript were performed at the *Nanospectroscopy* beamline at *Elettra Sincrotrone Trieste* using an *ELMITEC PEEM-LEEM* microscopy. with the help of the beamline staff: Andrea Locatelli, Tevfik Onur and Francesca Genuzio.

The incident x-ray beam is set at grazing incidence, 16°. In this geometry the magnetic contrast is mainly sensitive to the in-plane magnetisation component but also weakly sensitive to the out-of-plane component. In our system with perpendicular magnetisation, where Néel DWs and Bloch DWs are present, we expect to have the largest contrast for a Néel DW as in this case the internal magnetisation is parallel to the incoming beam.

Given an incident x-ray beam pointing along the direction $\mathbf{u}$, with unit vector, $\mathbf{u_B}$ (defined for the angles θ_B and φ_B), the magnetic contrast may be expressed as:

$$C \propto \mathbf{m} \cdot \mathbf{u_B} = \cos(\varphi - \varphi_B)\cos\theta_B \sin\theta - \sin\theta_B \cos\theta, \tag{5.1}$$

where θ, φ are the magnetisation angles and I_0 is the maximum of the intensity. This contrast contains a symmetric term (in x), and an anti-symmetric term maximised when $\varphi_B = \varphi$, which is about four times larger than the contrast measured in saturated out-of-plane magnetised regions (the symmetric term).

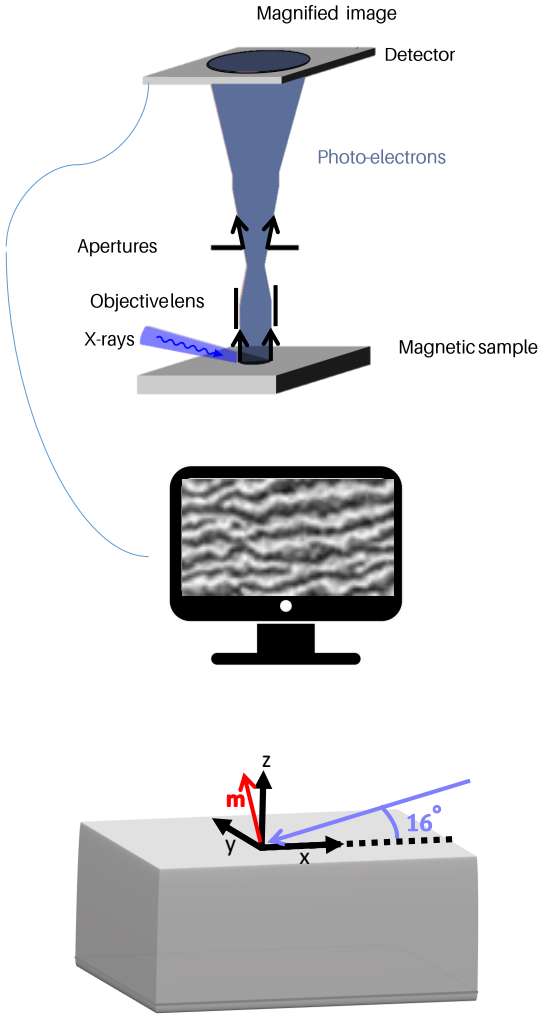

Figure 5.2: **X-ray photo-emission electron microscope**. The X-ray beam impinges the sample at a grazing angle of 16° on the sample surface as shown in the bottom image. The emitted photo-electrons are processed by the different electron-optic components before reaching an electron-sensitive screen.

5.2 | Stripe domains in $Au_{1-x}Pt_x/Co(t_{Co})/W(110)$

In this section the magnetisation configuration observed by MOKE microscopy and XMCD-PEEM are shown as well as a discussion of the results in terms of the 1D model and micromagnetic simulations

5.2.1 | One-dimensional model

In this subsection, we discuss phenomenologically the configuration expected for a DW along the in-plane easy and hard axes, and the predictions of a 1D micromagnetic model in the case of perpendicular magnetic anisotropy. Part of the work presented in this subsection and in the next one about elliptical skyrmions is part of a published article in *New journal of Physics, 2021*[156].

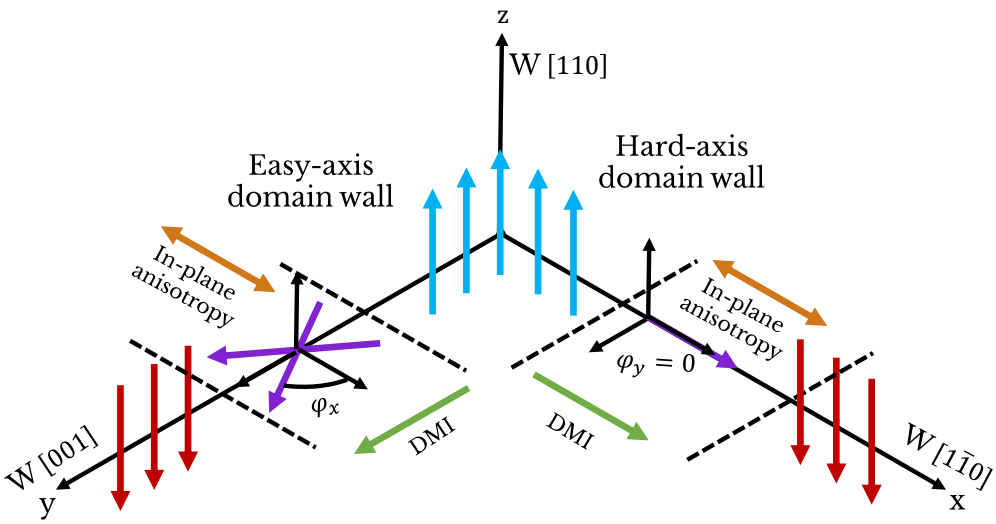

Figure 5.3: **Micromagnetic W(110) framework framework**. Sketch of the possible configurations for domain walls oriented along the in-plane easy axis and the in-plane hard axis.. Red, blue and purple arrows: magnetisation direction. Orange arrows: effective in-plane anisotropy field direction. Green arrows: effective DMI field direction. Adapted from [156].

In thin film systems with reduced symmetry the competition between the DMI and the MCA is expected to induce an anisotropic magnetic configuration of the DWs [157]. We can expect that for DWs oriented along the W[001] (in-plane hard axis, y) direction,

both the in-plane anisotropy and the DMI are promoting a Néel configuration, which is chiral because of the DMI (Fig. 5.3). For DWs oriented along the W[$\bar{1}$10] (in-plane easy axis, x) direction, the DMI is promoting a chiral Néel configuration while the in-plane anisotropy promotes a non-chiral Bloch configuration (Fig. 5.3), leading to an intermediate angle φ (or π - φ), between a Bloch DW and a Néel DW[157], with φ depending on the relative strength of K_{in} and D. In the phenomenological sketch of Fig. 5.3 both the DMI and magnetic anisotropy are represented as effective in-plane fields.

Considering a Bloch profile as an ansatz [61], we can express the DW areal density of energy along the two directions x and y as:

$$\sigma_x = \frac{2A}{\Delta} + 2\Delta\left(K_{\text{out}} - K_{\text{in}}\cos^2\varphi\right) + \frac{2t_{\text{FM}}\ln 2}{\pi}\frac{\mu_0 M_{\text{s}}^2}{2}\sin^2\varphi - \pi D_y \sin\varphi, \tag{5.2a}$$

$$\sigma_y = \frac{2A}{\Delta} + 2\Delta\left(K_{\text{out}} - K_{\text{in}}\cos^2\varphi\right) + \frac{2t_{\text{FM}}\ln 2}{\pi}\frac{\mu_0 M_{\text{s}}^2}{2}\cos^2\varphi - \pi D_x \cos\varphi. \tag{5.2b}$$

The minimisation of Eq. 5.2 with respect Δ, leads to

$$\Delta(\varphi) = \sqrt{\frac{A}{K_{\text{out}} - K_{\text{in}}\cos^2\varphi}} = \Delta_0\Delta_\varphi, \tag{5.3}$$

where $\Delta_0 = \sqrt{\frac{A}{K_{\text{out}}}}$ is the DW parameter of a Bloch DW, $\Delta_\varphi = \sqrt{\frac{1}{1-\kappa\cos^2(\varphi)}}$ and $\kappa = \frac{K_{\text{in}}}{K_{\text{out}}}$. Therefore, the normalised DW energy may be expressed as:

$$\tilde{\sigma_x} = \frac{\sigma_x}{2\sqrt{AK_{\text{out}}}} = \frac{1}{\Delta_\varphi} + \Delta_\varphi\left(1 - \kappa\cos^2\varphi\right) + \delta_{\text{d}}\sin^2\varphi - d_{0,y}\sin\varphi, \tag{5.4a}$$

$$\tilde{\sigma_y} = \frac{\sigma_y}{2\sqrt{AK_{\text{out}}}} = \frac{1}{\Delta_\varphi} + \Delta_\varphi\left(1 - \kappa\cos^2\varphi\right) + \delta_{\text{d}}\cos^2\varphi - d_{0,x}\cos\varphi, \tag{5.4b}$$

where $\delta_{\text{d}} = \frac{t_{\text{FM}}\ln 2}{\pi}\frac{\mu_0 M_{\text{s}}^2}{2A}\Delta_0$ and $d_{0,i} = \frac{\pi D_i}{2\sqrt{AK_{\text{out}}}}$. Physically, d_0 can be seen also as $d_0 = \frac{2D}{D_{\text{c}}}$, being D_{c} the critical DMI at which the DW energy becomes negative, promoting the formation of spin-spirals [61]. On the other hand κ describes the aspect ratio between the in-plane anisotropy and the out-of-plane anisotropy. Note that by definition, κ needs to be lower than 1 as otherwise the magnetisation lies in-plane, and d_0 must be lower than 2.0.

Equation 5.4 is a dimensionless equation, with $\kappa, \delta_{\text{d}}$ and d_0 as magnetic parameters and φ as a variable. The numerical minimisation of Eq. 5.4, with $\delta_{\text{d}} = 0.07$[1] leads to the

[1]This value is chosen considering t_{FM} =0.6 nm, M_{s} =1.15 MA/m, Δ_0 =6 nm and A =16 pJ/m

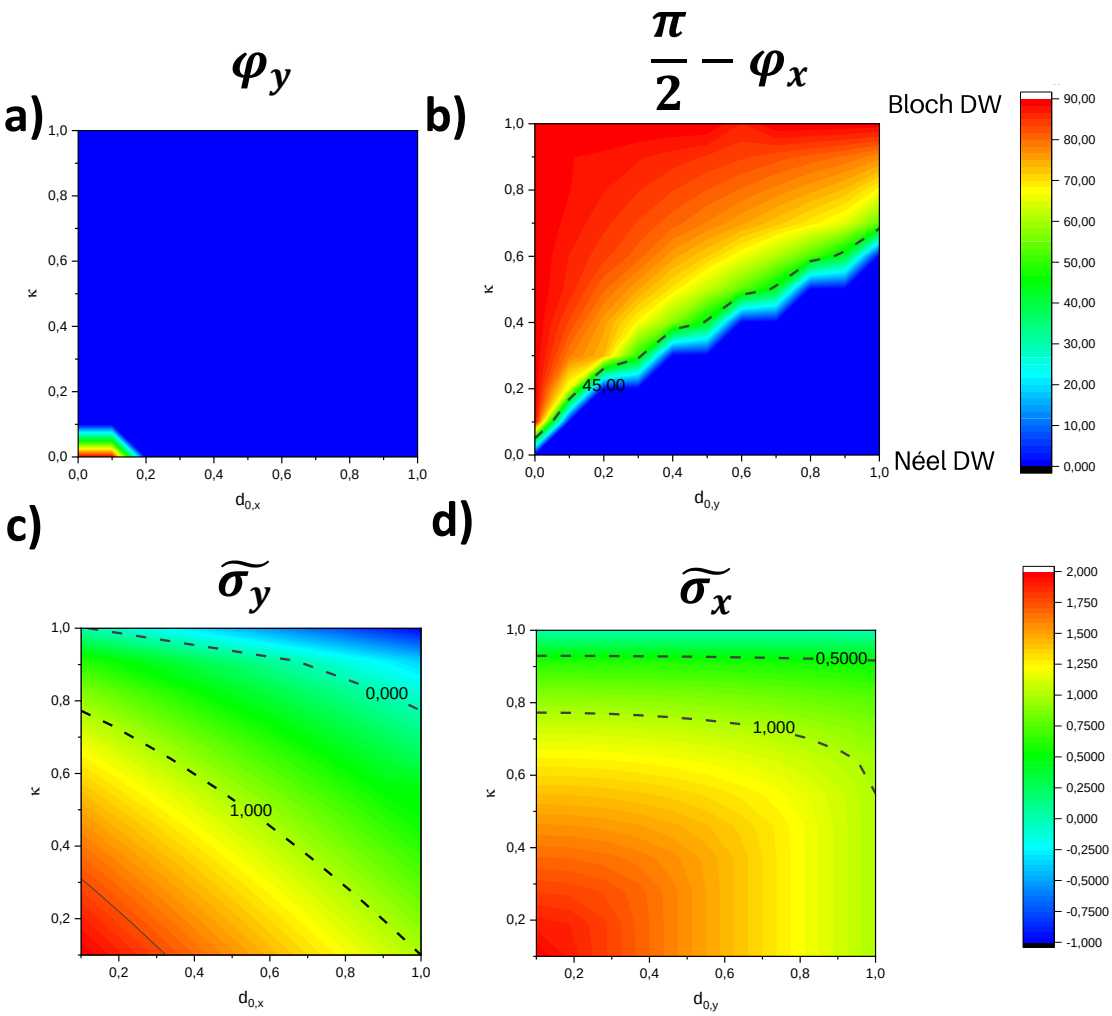

Figure 5.4: **Phase diagram** *vs* κ **and** d_0. Domain wall internal magnetisation along the easy **a)** and hard **b)** in-plane axis. Colour map: Red: 90°, Bloch DW) ; Dark blue: 0°, Néel DW). Normalised domain wall energy along the easy **a)** and hard **b)** in-plane axes. Colour map: Red: 2.0; Dark blue: -1.0.

$[d_0, \kappa]$ phase diagram shown in Fig. 5.4. The step size for $\Delta\kappa$ and Δd_0 has been set to 0.1.

Figures 5.4 **a)** and **b)** shows the internal magnetisation angle along the two main in-plane directions while Fig. 5.4 **c)** and **d)** shows the normalised DW energy along the two in-plane directions. It is necessary to clarify that the step discontinuous line

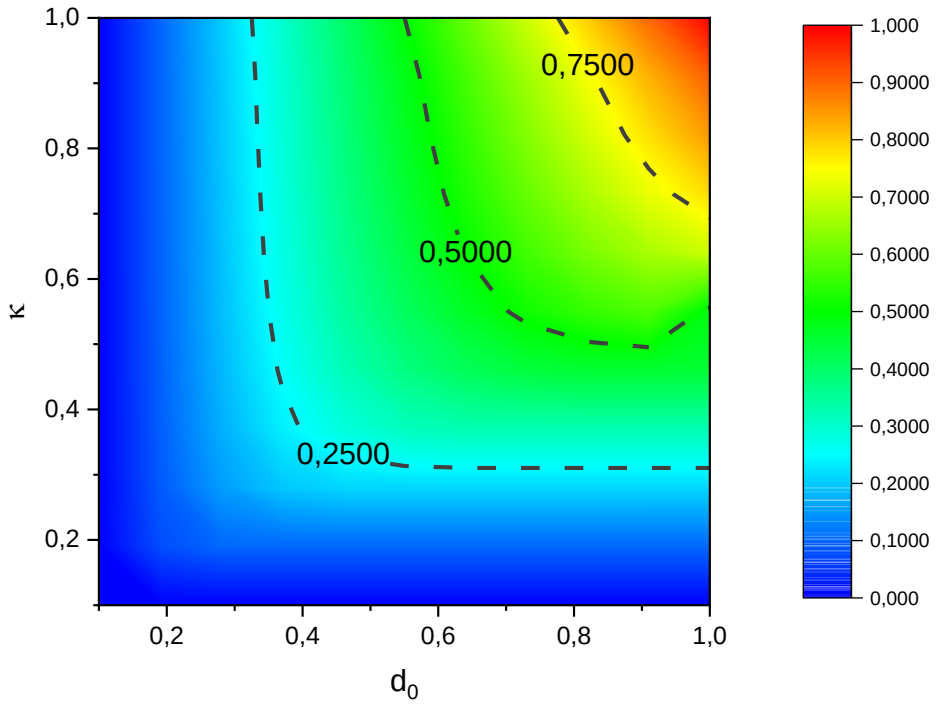

Figure 5.5: **Anisotropic domain wall energy.** Phase diagram showing the evolution of the normalised domain wall energy difference, $\widetilde{\sigma_x} - \widetilde{\sigma_y}$.

observed in Fig. 5.4 **a)** and **b)** at the transition between dark and light blue regions, is an artefact associated to the fact that the continuous transition from a Néel-Bloch configuration to a Néel configuration (for a fixed κ) occurs for values of d_0 lower than the step size, $\Delta d_0 = 0.1$.

Two limiting cases take place in the absence of DMI, $d_0 = 0$ or in the absence of the in-plane anisotropy $\kappa = 0$. In the absence of the DMI, we obtain a classical case when a magnetic film with perpendicular anisotropy can support Bloch DWs, $\varphi = 90°$ along the two directions. In the absence of the in-plane anisotropy, a minimum DMI strength is needed to overcome the demagnetising DW energy, about $d_0 \approx 0.1$. Finally, when the two interactions are present two very different behaviours are observed along the two directions. Along the x-direction the DW is always Néel for any combination of κ and d_0, while along the y-direction the magnetisation changes from Bloch, (κ much larger than d_0) to Néel when κ is much lower than d_0. Intermediate configurations are found for intermediate values of κ and d_0.

The normalised DW energy decreases as d_0 and/or κ increases (Figures 5.4 **c) d)**). Yet, the rate at which it decreases is different, as the energy decreases faster when in-

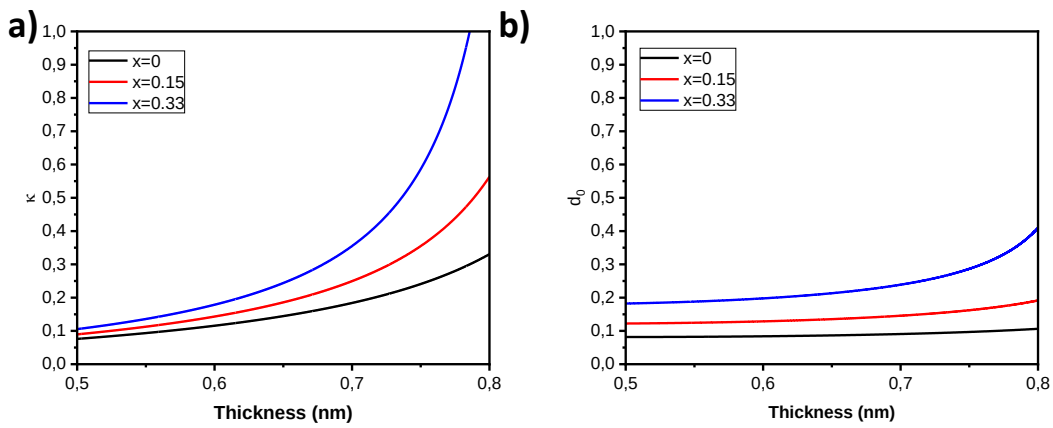

Figure 5.6: Calculated variation of κ and d_0 as function of the cobalt thickness for different platinum compositions.

creasing κ rather than d_0. The most significant difference occurs when increasing simultaneously κ and d_0, as in this case the energy along x, decreases significantly faster than along the y-direction.

Finally, we can reproduce the difference in the normalised DW energy between the two directions as a function of κ and d_0 (Fig. 5.5) [2]. It is clearly observed that when increasing the two parameters simultaneously, the difference increases. In order to increase κ and d_0 one can either tune K_s and D_s e.g., changing the Au-to-Pt content, or tuning the Co thickness due to the interfacial nature of the DMI and the MCA. Figure 5.6 shows the calculated thickness dependence of these two parameters for different Pt content using the values of Table 4.4. As it can be observed, when increasing the Pt content, both κ and d_0 increases. In addition, when approaching the spin-reorientation transition, $K_{out} \approx 0$, κ increases rapidly while d_0 also increases but less abruptly.

5.2.2 | Observation by Kerr and XMCD-PEEM

The domain and internal DW structure of the $Au_{1-x}Pt_x/Co(t_{Co})/W(110)$ stacks was investigated at Institut Néel by MOKE microscope and at the synchrotron by XMCD-PEEM.

Two samples are investigated in this section: First, the sample with a double wedge of Au-to-Pt composition and Co thickness, $Au_{1-x}Pt_x/Co(t_{Co})/W(110)$ (sample A), which was characterised by BLS (see Chapter 4), and a sample with a single wedge of Co thickness with a fixed composition of Pt, $Au_{0.67}Pt_{0.33}/Co(t_{Co})/W(110)$(sample B). Sample B

[2] We have considered for simplicity that $d_{0,x} = d_{0,y}$

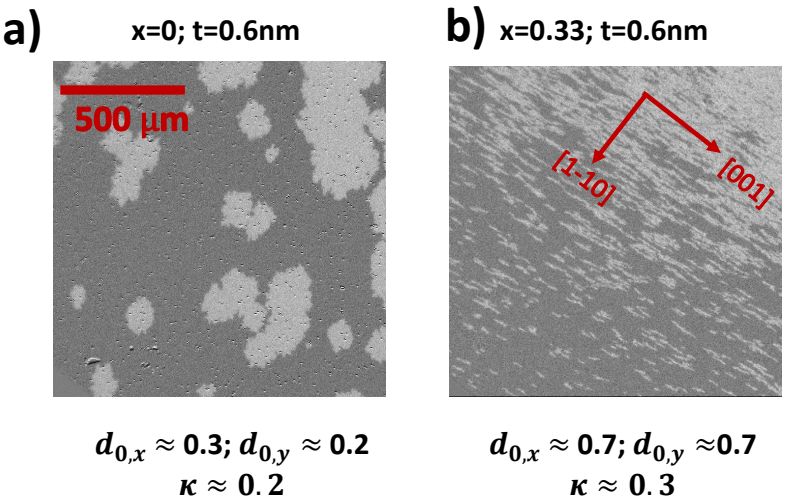

Figure 5.7: **Differential Kerr images showing reversed domains for different compositions of Au-to-Pt, $Au_{1-x}Pt_x$ (Sample A).**

was also characterised with BLS in the DE configuration by *Hans Nembach, NIST (Colorado)*. A k_{SW} =16.7 µm^{-1} with H_{ext} = ±0.6 T was used. The derived magnetic parameters for sample B are shown in Table 5.1

Figure 5.7 shows the different domain shapes obtained after saturating the magnetisation along the +**z** direction. A background image is taken and substracted from all the subsequent images. Next, an opposite magnetic field lower than the coercivity along −**z**, resulting into the nucleation of magnetic domains. Two different Au-to-Pt compositions, Au/Co(0.6nm)/W(110) and $Au_{0.67}Pt_{0.33}$/Co(0.6nm)/W(110) in sample A are studied. In the absence of Pt, Au/Co(0.6nm)/W(110), the domains are round and not significant sign of anisotropy is observed. On the other hand, when introducing Pt, $Au_{0.67}Pt_{0.33}$/Co(0.6nm)/W(110), a clear anisotropy in the domain shape is found, being the domains aligned along the hard in-plane axis. This elliptical shape may be understood considering the phase diagram shown in Fig. 5.5. For Au/Co(0.6nm)/W(110)

Table 5.1: **Micromagnetic parameters derived from BLS measurements in $Au_{0.67}Pt_{0.33}$/Co(0.8nm)/W(110).** An exchange stiffness of A =16 pJ/m and a spontaneous magnetisation of M_s =1.15 MA/m is considered [156].

	$D_{s,x}$ [pJm^{-1}]	$D_{s,y}$ [pJm^{-1}]	K_u [kJm^{-3}]	K_{in} [kJm^{-3}]
Sample B	0.74 ±0.1	0.79±0.1	970 ±100	94 ±9

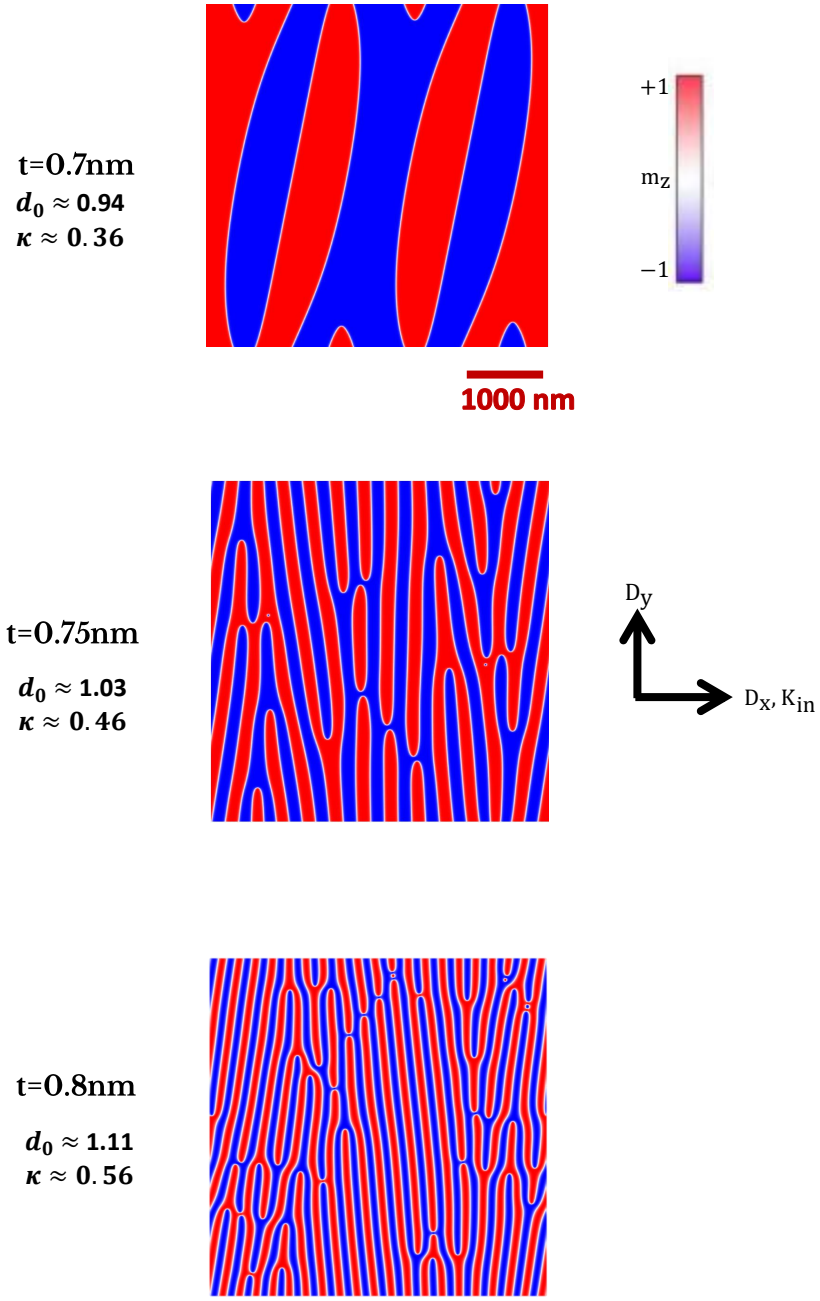

Figure 5.8: **Micromagnetic simulations of self-organised stripe domains** 4096 nm^2 magnetic configuration for different thickness using the values of Table 5.1. As observed in Fig. 5.9 the stripe periodicity also decreases as the thickness decreases. Colour code: Red $m_z = +1$, blue $m_z = -1$.

, we are located in the dark blue region, where the difference in the DW energy between the two directions is almost zero. On the other hand, for $Au_{0.67}Pt_{0.33}/Co(0.6nm)/W(110)$ we are in the light-blue-green zone, where the difference in energy between the two directions is about 0.25. As a consequence of the significantly lower DW energy of the DWs oriented along the W[001], y-axis, the stripe domains are almost uniquely oriented along it.

Micromagnetic 2D simulations are performed using the software package Mumax^3 [152; 153] in a system of 2048 $\times$ 2048 $\times$ 1 rectangular cells of size 2 nm$\times$2 nm$\times$ t_{FM} nm, with only one cell across the film thickness, so that the magnetisation is assumed to be uniform along this direction as the film thickness is much lower than the exchange length. The magnetic parameters of Table 5.1 are used. A 200 nm diameter bubble domain it is relaxed at zero field, resulting in this particular domain pattern. For convenience defects and temperature are neglected. As observed by MOKE, self-organised stripe domains aligned along the y-axis (hard in-plane axis) are stabilised using the values of Table 5.1 for different thicknesses of Co (Fig. 5.8).

The domain configuration for Co thicknesses between 0.6-0.75 nm and $Au_{0.67}Pt_{0.33}/Co(t_{Co})/W(110)$ (sample B) is also investigated by XMCD-PEEM (Fig. 5.9 and 5.10). The images were recorded at room temperature at zero magnetic field, with the incoming x-ray beam parallel to the two main in-plane axis of W(110).

Figure 5.9 **a)- c)** shows the XMCD-PEEM images when the x-ray beam is parallel to the W[001] direction. As expected from the 1D model and the 2D micromagnetic simulations, and already observed by MOKE, the stripe domains are almost uniquely oriented close to the W[001] direction. The stripe domain width sharply decreases with increasing the Co thickness, whose width is determined by the competition between the dipolar energy and the domain wall energy. The experimental points in Fig. 5.9 **d)** are fitted with an exponential decay, in agreement with theoretical models by Kashuba and Pokrovsky [158], without considering DMI, and by Meier et al. [159] who considered the DMI in a 2D spacing model.

The images in Fig. 5.9 do not show any extra magnetic contrast at the DW. Dark and bright gray contrast corresponds to the magnetisation pointing up and down, respectively, perpendicular to the film plane. Two possible explanations are possible for explaining the absence of at the DW: 1) The magnetisation within the DW is not completely aligned along the x-ray beam direction i.e. it is not completely Néel. 2) The spatial resolution, which in the *ELMITEC-PEEM* is about 20 nm in ideal conditions is lower than the DW width.

According to the 1D model we derive that $\pi\Delta_x = 46\pm10$ nm and $\varphi_x = 34°$. Hence,

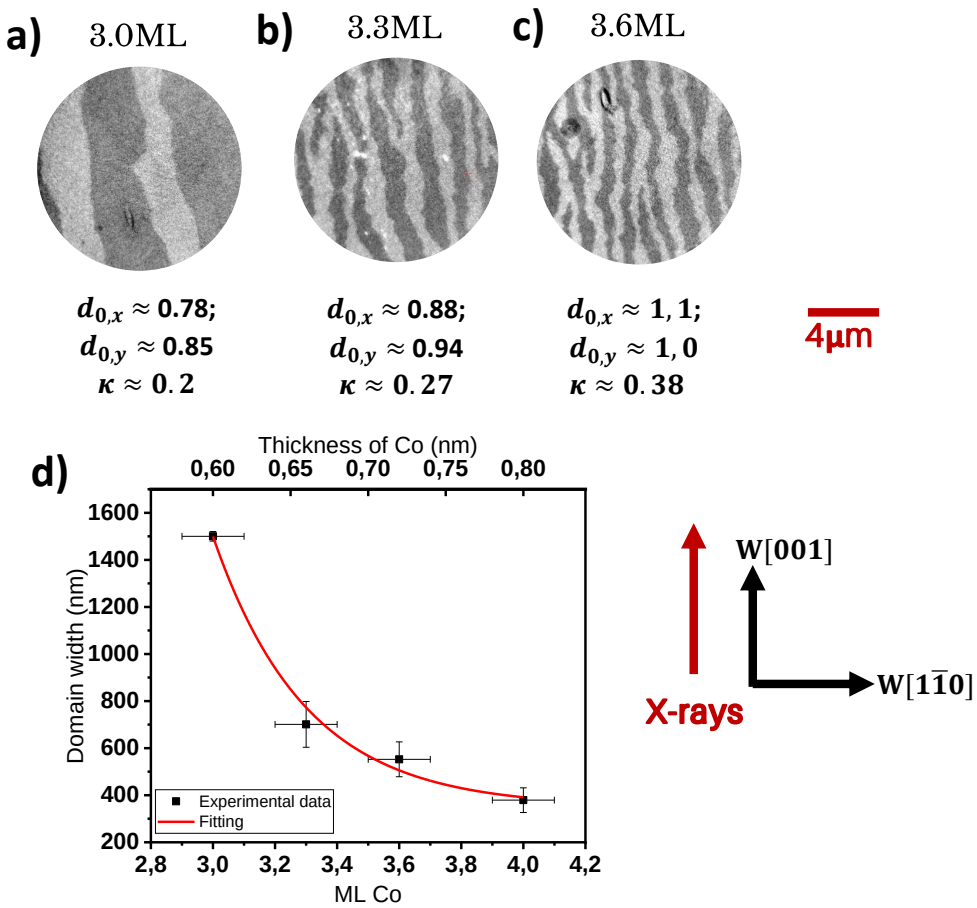

Figure 5.9: **X-ray magnetic circular dichroism photoemission electron microscopy images for $Au_{0.67}Pt_{0.33}/Co(t_{Co})/W(110)$ taken with the projection of the x-ray beam on the sample surface parallel to the** W[001] **for different thicknesses of Co. a)-c)** 5 µm^2 diameter x-ray magnetic circular dichroism photoemission electron microscopy images images for different Co thicknesses. **d)** The stripe domain width decreases exponentially with the cobalt thickness which was determined from the position in mm on the wedge and the known thickness gradient. The raw data is fitted with an exponential decay function. Modified from [156].

the spatial resolution is larger than the DW width, and therefore enough to image it. Indeed, since from the 1D model the magnetisation in the center of the DW is expected to be mainly parallel to the easy-axis (Fig. 5.3), therefore perpendicular to the incoming x-ray beam the expected magnetic contrast is between the contrast of the two domains,

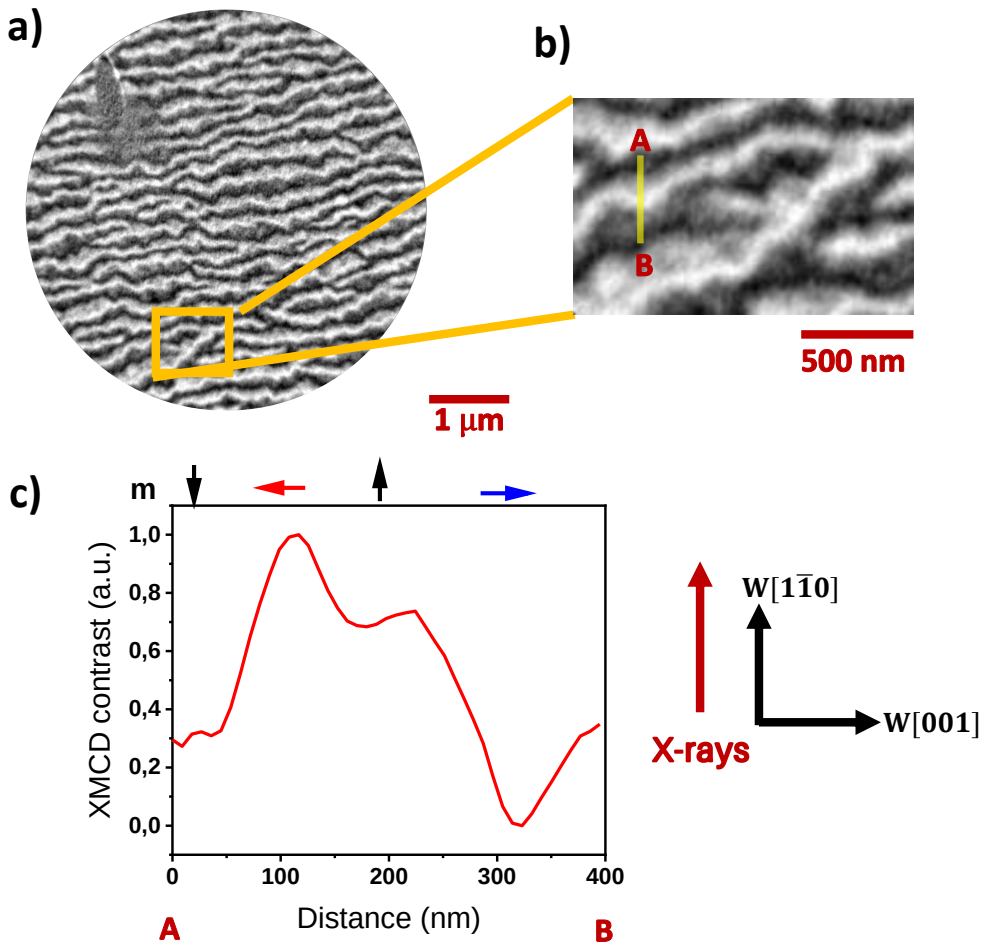

Figure 5.10: **X-ray magnetic circular dichroism photoemission electron microscopy image for $Au_{0.67}Pt_{0.33}$/Co(0.8nm)/W(110) taken with the projection of the x-ray beam on the sample surface parallel to the W[$\bar{1}$10] direction.** **a)** $5\times5\,\mu m^2$ diameter X-ray magnetic circular dichroism photoemission electron microscopy image **b)** $1.5\times1.5\,\mu m^2$ zoom of a part of image **a)** **c)** Line scan of the magnetic contrast along the W [$\bar{1}$10] direction perpendicular to the domain wall direction along the yellow line in **b)**. Modified from [156].

and therefore indiscernible. In order to verify the predictions of the 1D model, we rotated the sample by 90° so that the image in Fig. 5.10 **a)** was taken with the x-ray beam oriented along the W [$\bar{1}$10], for a Co thickness of about 0.8 nm. A clear extra DW contrast is now observed indicating that the in-plane component of the magnetisation is perpendicular to the DW direction. Furthermore, the DW contrast alternates between

black and white, indicating that the DWs are chiral Néel DW. A line scan along the beam direction (Fig.5.10 **b)-c)**) allows confirming the right-hand chirality of the DWs parallel to W[001]. The observed right-hand chirality is in agreement with the sign of the DMI determined with BLS. In addition, the fitting of the raw data with Eq. 5.1) allows to derive a DW width of $\pi\Delta_y = 52 \pm 5$ nm, in good agreement with the results expected by the 1D model ($\pi\Delta_y = 59 \pm 5$ nm). Note that the magnetisation direction for DWs oriented along the in-plane easy axis could not be determined since DW oriented along this direction are rare and always very short.

5.2.3 | Summary

To summarise, polar MOKE microscope revealed that the domains are round for Au/Co(0.6nm)/W(110) while they become anisotropic $Au_{0.67}Pt_{0.33}$/Co/W(110), as a consequence of the increase in the anisotropy in the DW energy. In agreement with the 1D model XMCD-PEEM images reveal a strongly anisotropic domain configuration for $Au_{0.67}Pt_{0.33}$/Co/W(110), with a dominant orientation of stripe domains and DWs along the in-plane hard magnetisation axis, W[001] direction. The XMCD-PEEM images for $Au_{0.67}Pt_{0.33}$/Co(0.8nm)/W(110) reveal that these DW have chiral Néel structure. The small number and short length of DWs oriented along the W[$\bar{1}$10] direction did not allow confirming the dominant Bloch configuration expected for such DW. However, the strongly anisotropic domain structure is consistent with the expected difference in energy of DWs oriented along W[001] and W[$\bar{1}$10]. Note that such a strong anisotropy of the DW orientation was not observed in the Fe/Ni/W(110) system of reference [157], as in his case the DMI is one order of magnitude smaller than in this sample, similar to the Au/Co(0.6nm)/W(110) stack.

5.3 | Skyrmions

5.3.1 | Introduction

Skyrmion bubbles can be stabilised in thin films starting from a stripe domain phase and applying a perpendicular magnetic field [160; 161] or by the confinement in nanodots with the proper lateral size [9; 16].

In our system a non-circular shape to the magnetic skyrmion may be expected due to the anisotropic DMI and the in-plane anisotropy. In this section, we will show the results of XMCD-PEEM measurements revealing that the skyrmions have indeed a non-circular shape. This non-circular shape will be discussed with the support of the 1D model described previously, and 2D micromagnetic simulations. Indeed, these results will allow us to predict the evolution of the skyrmion ellipticity as function of the Au-to-Pt composition.

5.3.2 | Observation by XMCD-PEEM

We investigated the magnetic field-induced skyrmion bubbles in the sample discussed in the previous section, $Au_{0.67}Pt_{0.33}/Co(0.8nm)/W(110)$ (Sample B). We studied a region close to the spin reorientation transition (about 0.8 nm of Co), where K_{out} is small and the presence of metastable skyrmion bubbles is favored.

Figure 5.11 shows the XMCD-PEEM images taken with the x-ray beam parallel to the W[$\bar{1}$10] direction, under the application of different out-of plane magnetic fields. Upon increasing the magnetic field strength, the width of the domains having their magnetisation anti-parallel to the field decreases in order to decrease the Zeeman energy (Fig. 5.11 **c)**). Interestingly, the images show a non uniform contrast of the magnetic background under B_z=11.7 mT. A close look reveals that the magnetisation shows a modulation which cannot be explained in terms of minimisation of the dipolar or the exchange interaction. This phenomenon is so far unexplained.

For an applied field of B_z =11.7 mT, elliptical skyrmion bubbles are observed (Fig. 5.11 **c)**). Larger applied fields cause the annihilation of the remaining bubbles and domains. Line scans of the magnetic contrast along the major and minor axes of the skyrmion bubbles give a $R_y = 66$ nm and $R_x = 23$ nm, where R_x and R_y denote the skyrmion radius along the easy and hard in-plane axes respectively.

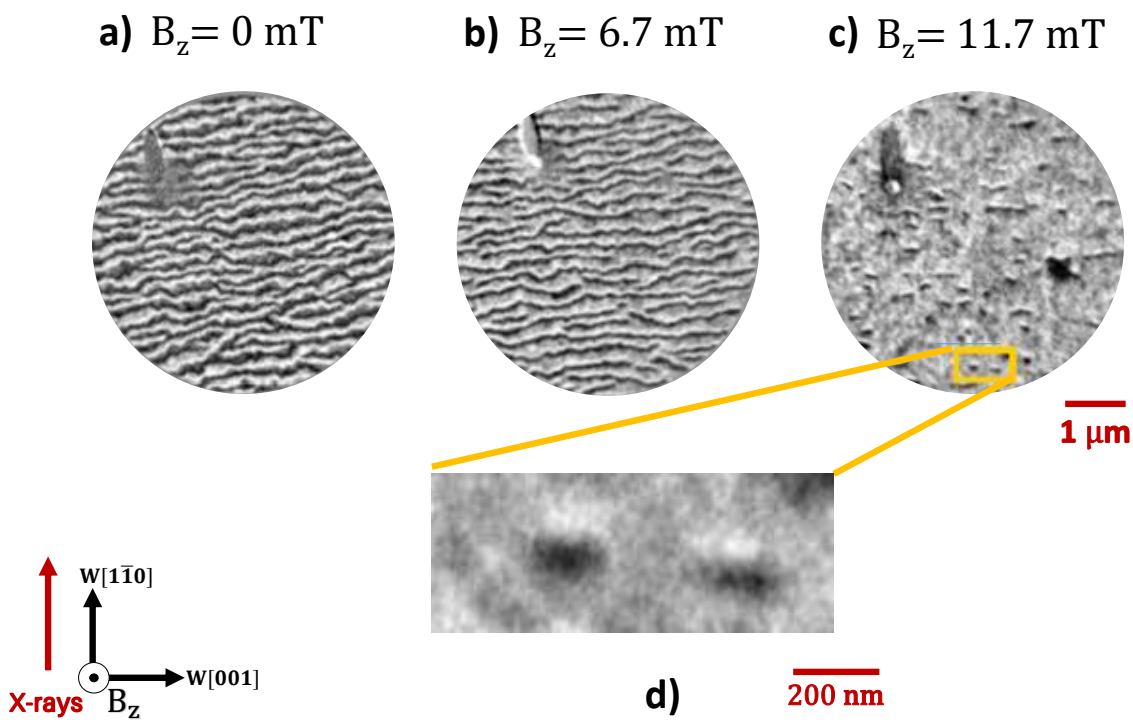

Figure 5.11: **Elliptical skyrmion observed with x-ray magnetic circular dichroism photoemission electron microscopy in $Au_{0.67}Pt_{0.33}$/Co(0.8nm)/W(110).** The images are taken with the x-rays along W[$\bar{1}$10] for different perpendicularly applied magnetic fields. When a perpendicular magnetic field equal to 11.7 mT is applied elliptical skyrmion bubbles are observed. From [156].

5.3.3 | Why an elliptical shape?

This elliptical shape of the skyrmion bubbles can be explained phenomenologically by the anisotropy of the DW energy as discussed in the previous section. For a given surface area, the total DW energy depends on the shape of the skyrmion bubble, while the surface dipolar energy and the Zeeman energy are more or less constant. The total DW energy, i.e. the DW energy density multiplied by its length, can be minimised by increasing the DW length along the in-plane hard axis and decreasing its DW length along the in-plane easy axis, leading to an elliptical skyrmion shape.

In our system, due to the anisotropic magnetic interactions, the DMI and the in-plane anisotropy may induce an anisotropy on the DW energy density. While both magnetic interactions by themselves induce an anisotropy on the DW energy density, the resulting elliptical skyrmion show some differences. This is indeed clearly observed

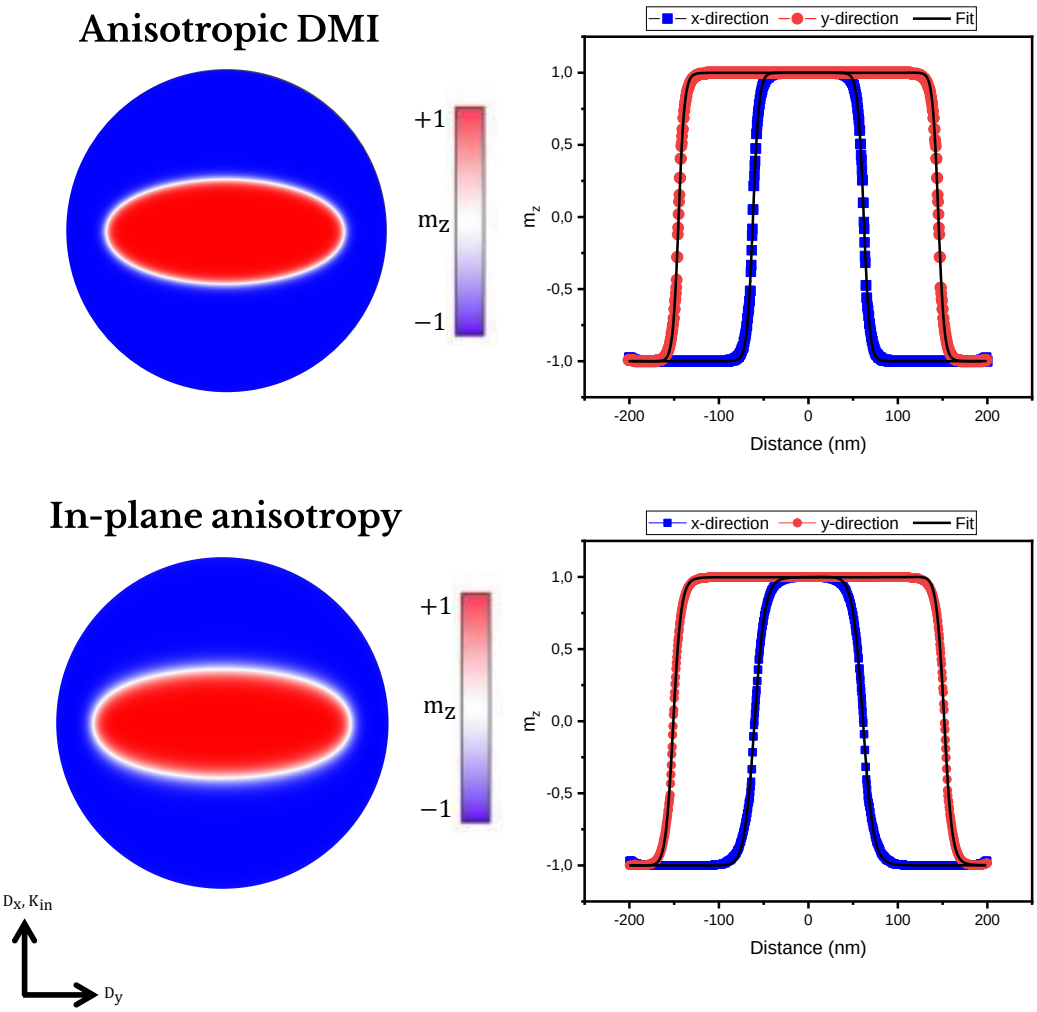

Figure 5.12: **Micromagnetic stabilised elliptical skyrmion.** Due due to an anisotropic DMI: ($D_y/D_x = 0.75$) with D_x=1.5 kJ/m^3 and K_{in} =0 mJ/m^2, or an in-plane anisotropy ($D_y/D_x = 1$) with D_x=1.5 mJ/m^2 and K_{in} =136 kJ/m^3. A =16 pJ/m, M_s =1.15 MA/m, K_u =1031 kJ/m^3 are used for the two cases.

in Fig. 5.12 where micromagnetic simulations are performed for either anisotropic DMI or an in-plane anisotropy along the x-axis.

The eager reader could wonder if the analytical model presented in Chapter 3 by Bernand et al. [7] could be used for our system. This model relies on the circular symmetry which in our system is broken because the anisotropic DMI and the in-plane anisotropy. Nevertheless, the model could be modified by accounting for an average

Table 5.2: **Micromagnetic parameters of an elliptical Néel skyrmion of radius R and wall (between the skyrmion core and the outer domain) width Δ in a two-dimensional film for:**
Anisotropic DMI: $(D_y/D_x = 0.75)$ with D_x=1.5 mJ/m^2 and K_{in} =0 J/m^3.
In-plane anisotropy: $(D_y/D_x = 1)$ with D_x=1.5 mJ/m^2 and K_{in} =136 kJ/m^3.

	R_x [nm]	R_y [nm]	Δ_x [nm]	Δ_y [nm]
Anisotropic DMI	61.7	145.1	7.5	7.5
In.plane anisotropy	60.5	151.4	11.4	8.4

DW energy density, $\overline{\sigma} = \frac{1}{2\pi}\int_0^{2\pi}\sigma(\varphi,\alpha)d\alpha$. Hence the resulting skyrmion radius derived from this model is an effective radius, defined as $R_{eff} = \sqrt{\frac{S}{\pi}}$, being S the skyrmion area, defined as the zone between the core and $m_z = 0$. While this model could account for an effective information of the the skyrmion shape, it would not allow us to study the radius along the two main in-plane directions. Because of this, we decided to perform 2D micromagnetic simulations.

Micromagnetic 2D simulations were performed using the software package Mumax^3 [152; 153] in a system of 410 × 410 × 1 rectangular cells of size 1 nm×1 nm×0.6 nm, with only one cell across the film thickness, so that the magnetisation is assumed to be uniform along this direction as the film thickness is much lower than the exchange length. A magnetic Néel skyrmion is set in the center of the 400 nm diameter dot and allowed to relax. Unless that otherwise said, A =16 pJ/m, M_s =1.15 MA/m, K_u =1031 kJ/m^3, and $\alpha = 0.3$ are used. Additionally, a DMI constant, either isotropic or anisotropic, and/or an in-plane anisotropy along the x-direction, can be introduced as well. For convenience, all the simulations were performed at T = 0 K, although temperature should play a significant role on the skyrmion stabilisation.

Figure 5.12 shows the stabilised elliptical skyrmion in a 400 nm circular dot and the radial distribution of $m_z = \cos\theta(r)$ along the two main in-plane directions. An in-plane anisotropy with an isotropic DMI or an anisotropic DMI without in-plane anisotropy are considered (Values in the caption of Table 5.2). The skyrmion radius, R and DW parameter Δ obtained from the fitting of the m_z profile using a 360° DW ansatz [162] are summarised in Table 5.2.

When only an anisotropic DMI is considered, $(D_y/D_x = 0.75)$, the largest radius is along the y-direction, the direction with the lower DMI, i.e. larger DW energy density. Moreover, the DW parameter is isotropic because the DMI does not affect the DW ansatz and hence its width as predicted by [16; 61; 163].

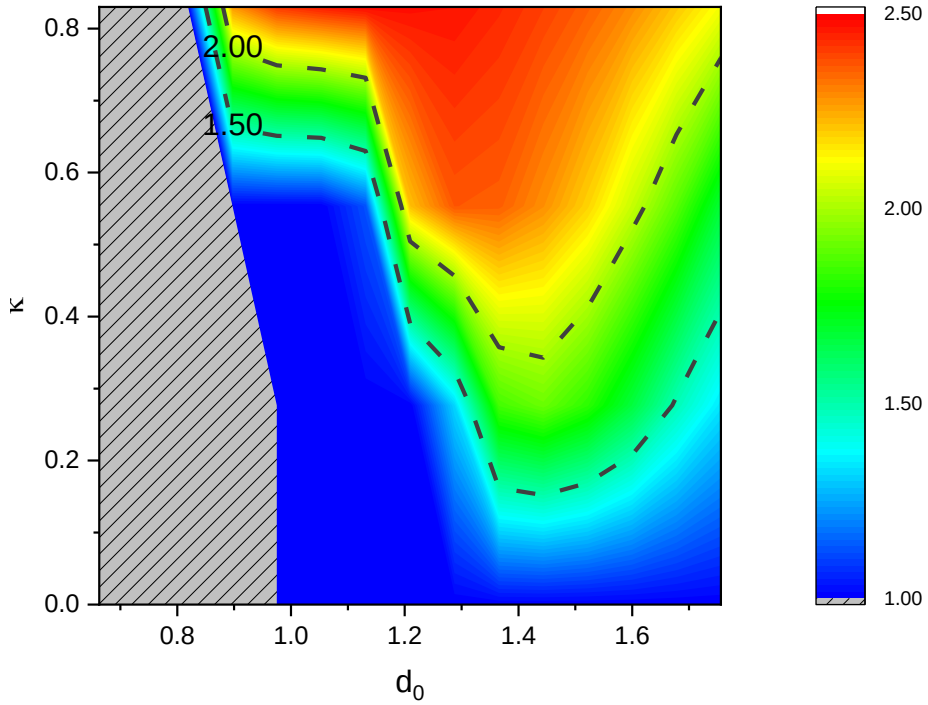

Figure 5.13: **Skyrmion ellipticity phase diagram.** Phase diagram showing the evolution of the skyrmion ellipticity R_y/R_x. The grey zone with lines represents the zone where a magnetic skyrmion is not stable.

When the DMI is isotropic, but an in-plane anisotropy along the x-axis is introduced, the largest radius is along the y-axis. Yet, the DW parameter Δ is different along both main in-plane directions, being wider along the easy-axis.

While we have observed an elliptical shape due to the anisotropic interactions in $Au_{0.67}Pt_{0.33}$/Co(0.8nm)/W(110), in Au/Co(0.9nm)/W(110) where the DMI is largely anisotropic, the magnetic domains shown in Fig. 5.7, as well as the Néel skyrmions are *apparently* isotropic [139]. Hence, in order to understand the role of the in-plane anisotropy on the skyrmion shape, we performed a series of micromagnetic simulations, studying the elliptical shape of a Néel skyrmion stabilised in a 400 nm dot varying $\kappa = \frac{K_{\text{in}}}{K_{\text{out}}}$ and $d_0 = \frac{\pi D}{2\sqrt{AK_{\text{out}}}} = \frac{D}{D_{\text{min}}}$. The simulations were carried out considering steps of 0.10.1 mJ/m^2 in D which is considered isotropic, and 10 kJ/m^3 in K_{in} fixing the value of K_{out} to 0.2 MJ/m^3. Similarly as done in Fig. 5.12, the m_z radial component along both main in-plane directions is fitted with a 360° DW ansatz [162]. The resulting $[d_0, \kappa]$ phase diagram displays the skyrmion ellipticity defined as the aspect ratio be-

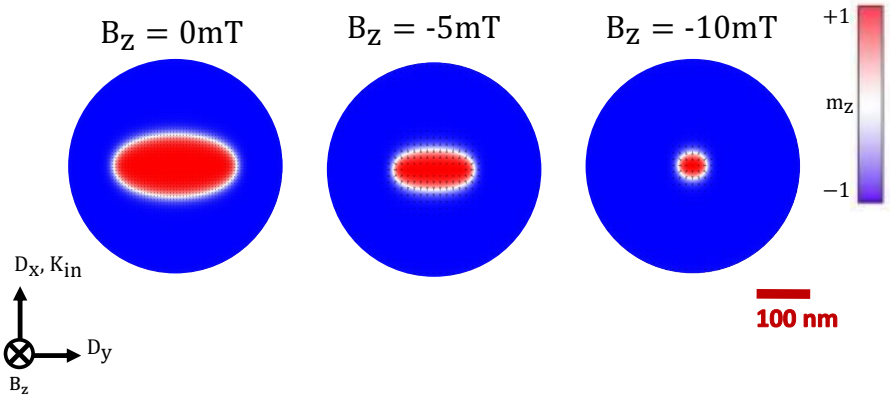

Figure 5.14: **Micromagnetic stabilised elliptical skyrmion for $Au_{0.67}Pt_{0.33}$/Co(0.8nm)/W(110).** Micromagnetic simulations using the experimental values of the magnetic parameters reported in table 5.1 under an external perpendicular magnetic fields of $B_z = 0\,\mathrm{mT}$, $B_z = -5\,\mathrm{mT}$ and $B_z = -10\,\mathrm{mT}$. From [156].

tween the skyrmion radius along the y- and x- directions, R_y/R_x[3] (Fig. 5.13). Note that the observed step lines are an artefact due to the fact that the step size for some values e.g. $d_0 = 1.2$ is too large to have a smooth transition.

For a small DMI value, ($d_0 < 1$), either with or without an in-plane anisotropy, a skyrmion bubble cannot be stabilised and therefore a uniform ferromagnetic state is obtained. This region corresponds with the dark blue zone. Using a larger DMI value, a circular skyrmion bubble can be stabilised. Note that $d_{0,\mathrm{min}}$ is lower than 1 as in a continuous thin film, due to the non-local demagnetising energy [7].

By adding a non-zero in-plane anisotropy, ($\kappa \neq 0$) the energy density of DWs oriented along the hard in-plane axis is reduced, allowing the stabilisation of a skyrmion with a small ellipticity for a small d_0 value. The ellipticity increases upon increasing the DMI, d_0, and/or the in-plane anisotropy, κ. Note that at $d_0 \approx 1.4$, the ellipticity reaches its maximum and for larger values it gets reduced. This is due to the fact that along the y-axis the radius, R_y ≈190 nm cannot increase more due to edge repulsion but it can increase along the x-axis, with the ellipticity, therefore reducing. This behaviour should not be observed in a continuous thin film. Experimentally, in $Au_{0.67}Pt_{0.33}$/Co(0.8nm)/W(110), we are located at $d_0 = 1.1$ and $\kappa \approx 0.8$, where the ellipticity is about 1.75, similar to the value found experimentally (1.81).

[3]Mathematically, R_y and R_x are known as the semi-major axis and semi-minor axis respectively, when $R_y > R_x$

For Au/Co(0.9nm)/W(110) we are located at $d_0 = 0.4$ and $\kappa \approx 0.5$, and therefore skyrmions should not be stable. The discrepancy may be explained considering the reduction of the nucleation energy due to pinning site [164]. Nevertheless, such low d_0 is not strong enough to induce a strong ellipticity, and therefore the skyrmion shape is circular.

Finally, we study the elliptical skyrmion bubble stabilised in a 400 nm diameter dot defect-free at 0 K, with the experimental values of the magnetic parameters in Table 5.1 with t_{Co}=0.8 nm). The resulting skyrmions are shown in Fig. 5.14. The best agreement with the experiment is found for an applied magnetic field $B_z = 5$ mT, giving $R_y = 65$ nm and $R_x = 36$ nm. The magnetic field is smaller than in the experiment ($B_z = 11.7$ mT). Nevertheless, due to the strong sensitivity of the skyrmion size to the magnetic parameters, we can consider the agreement satisfying. Furthermore, the experimental elliptical skyrmions are observed in a continuous film, while the simulations are carried out in a circular dot, where the dipolar effects are modified. These results are consistent with our experimental findings with XMCD-PEEM discussed previously.

5.4 | Merons

5.4.1 | Introduction

In addition to the study of skyrmions in perpendicularly magnetised systems in the spintronics community, there has also been a large effort on searching for alternative topological structures. One of such textures is the so-called meron which is described as a magnetic vortex and topologically equivalent to one-half of a skyrmion $\mathcal{Q} = \pm 1/2$.

As already described in Chapter 3, in magnetism, 2D textures such as skyrmions or merons, may have an associated topological charge that is a measure of the local winding of $\mathbf{m}(x, y)$ in the space. Following [89], the topological charge of 2D magnetic textures is given by:

$$\mathcal{Q} = \frac{1}{4\pi} \iint \mathbf{m} \cdot \left(\frac{\partial \mathbf{m}}{\partial x} \times \frac{\partial \mathbf{m}}{\partial y} \right) \mathrm{dxdy}, \tag{5.5}$$

where $\mathbf{m}(x, y)$ is the normalised magnetisation vector, a function of $\mathbb{R}^2$ which evolves in the unit sphere $\mathbb{S}^2$. This expression, may be represented in a more convenient way by making the transformation to polar coordinates (r, Ψ):

$$\mathcal{Q} = \mathcal{P} \cdot \mathcal{V}, \tag{5.6}$$

where $\mathcal{P}$ is the polarity and $\mathcal{V}$ the vorticity functions defined as;

$$\mathcal{P} = \frac{[-\cos\theta]_{r=0}^{r=\infty}}{2} = \frac{[m_z(r=0) - m_z(r=\infty)]}{2}, \tag{5.7}$$

$$\mathcal{V} = \frac{[\phi(\Psi)]_{\Psi=0}^{\Psi=2\pi}}{2\pi}. \tag{5.8}$$

The meron and skyrmion topology is determined by the vorticity ($\mathcal{V}$), which describes the in-plane magnetisation rotational direction and the polarity ($\mathcal{P}$), which describes the out-of-plane core magnetisation.

An important difference between merons and skyrmions occurs on the magnetisation peripheral: in merons the magnetisation aligns in-plane while that of skyrmions point toward out-of-plane directions. Furthermore, the magnetic skyrmions [4] core represents a large part of the texture, while for the magnetic meron the core is small (Figure 5.15).

The results presented hereafter are part of an article in preparation.

[4] Only for skyrmion bubbles. Not for **DMI-skyrmions!** (**DMI-skyrmions!**)

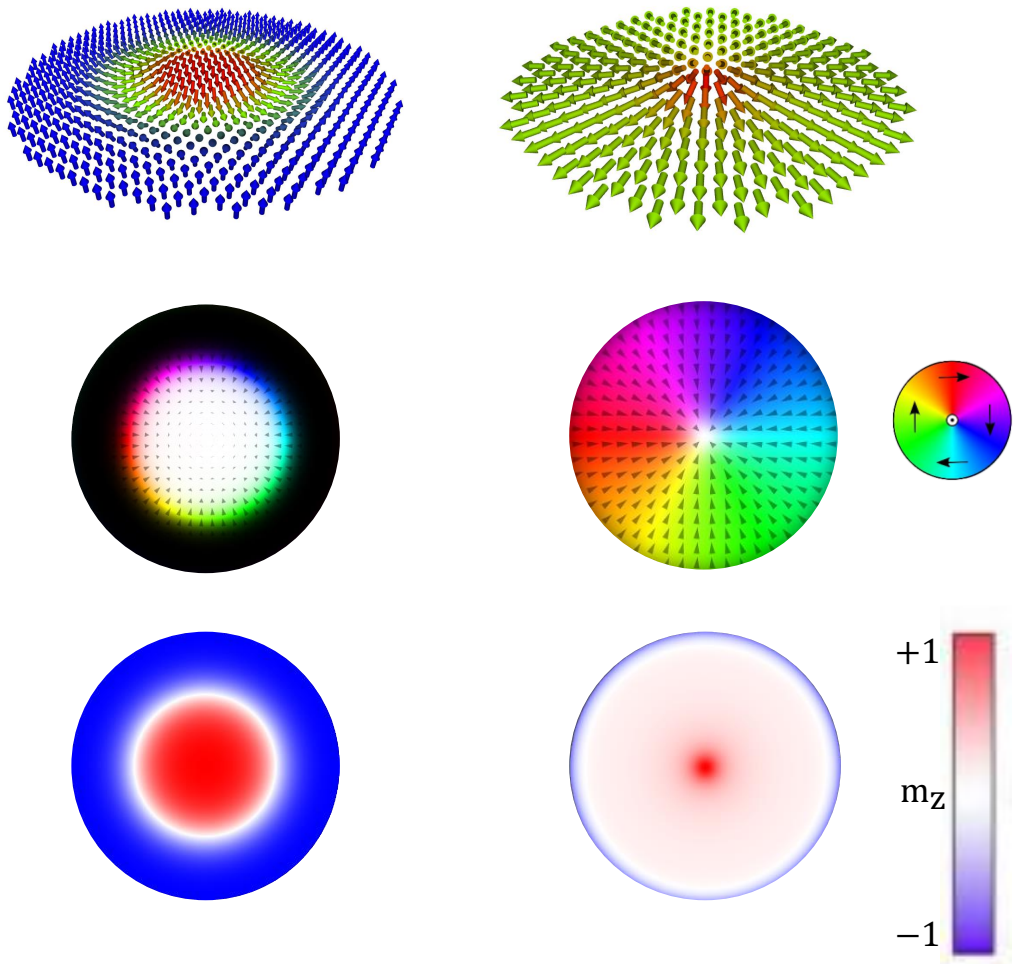

Figure 5.15: **Schematic representation of a Néel Skyrmion (left) and a Meron (right). Top:** Artistic representation. **Middle:** Magnetisation distribution. White and black represents the magnetisation pointing *up* and *down* out-of-the plane. The wheel represents the color code for in-plane magnetisation direction, red meaning magnetisation along positive x-direction and green meaning magnetisation along positive y direction. **Bottom:** Spatial z-component of the normalised magnetisation. Red means out-of-plane magnetisation *up* and blue *down*.

5.4.2 | Observation by XMCD-PEEM

Magnetic merons were observed by XMCD-PEEM in $Au_{0.58}Pt_{0.42}/Co(0.75nm)/W(110)$ within nanostructures fabricated by electron beam lithography and ion beam etching. A scanning electron microscopy image of the nanostructures are shown in Fig. 5.16. The magnetic properties of this sample were characterised by BLS and MOKE, within an unpatterned sample zone next to the region where merons were observed. The magnetic parameters are presented in Table 5.3.

Table 5.3: **Magnetic parameters extracted from VSM and BLS measurements for $Au_{0.58}Pt_{0.42}$ /Co(0.75nm)/W(110).**

A[pJ/m]	M_s[MAm^{-1}]	K_u [kJm^{-3}]	K_{in} [kJm^{-3}]	$D_{s,x}$ [pJm^{-1}]	$D_{s,y}$ [pJm^{-1}]
15±3	1.15±0.1	893±30	52 ±17	0.56±0.05	0.66±0.03

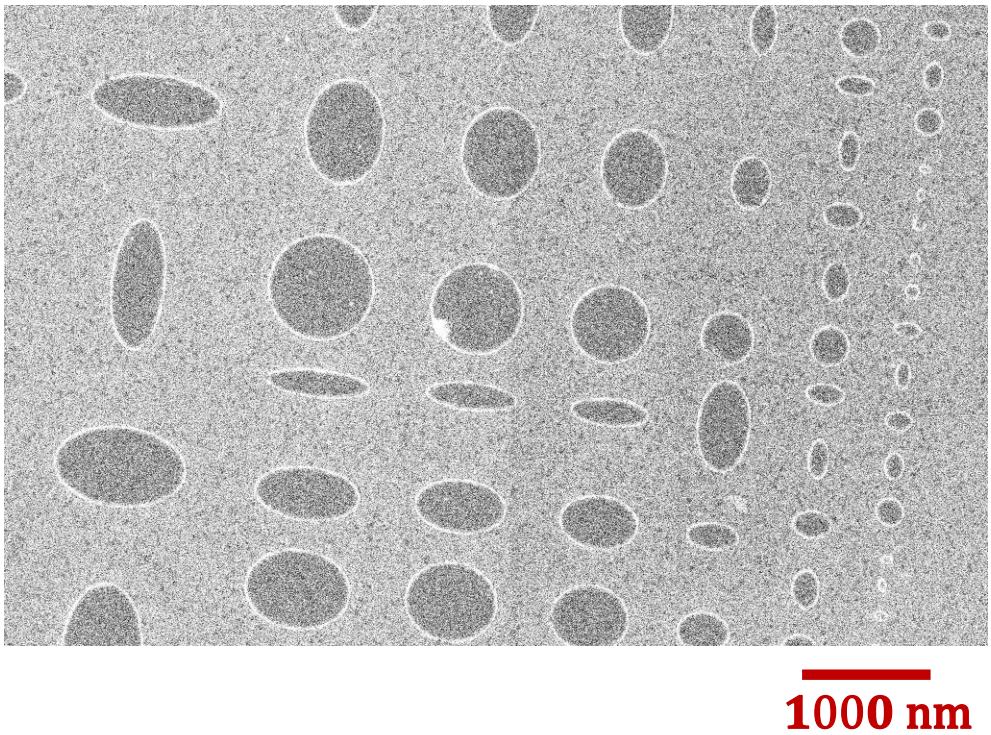

Figure 5.16: **Scanning electron microscopy image of the nanostructures in the $Au_{0.58}Pt_{0.42}$/Co/W(110) stack.**

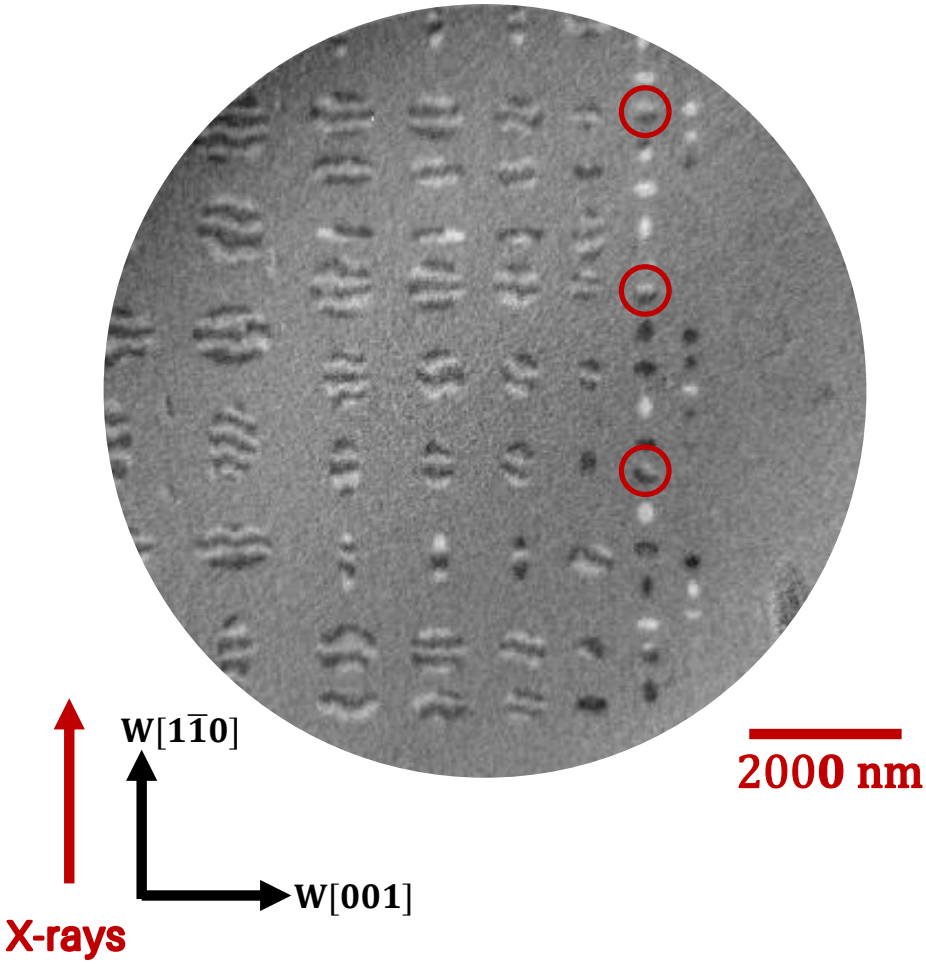

Figure 5.17: **X-ray magnetic circular dichroism photoemission electron microscopy-image for $Au_{0.58}Pt_{0.42}$/Co(0.75nm)/W(110) with the projection of the x-ray beam on the sample surface parallel to the W[$\bar{1}$10] direction.** Field-of view 10 µm. Red circles indicate magnetic merons.

Figure 5.17 shows a 10×10 µm^2 XMCD-PEEM image obtained with the x-rays along the W [$\bar{1}$10] direction, under no external field. Since x-rays are at grazing incidence. a large contrast occurs when the magnetisation lies in-plane. As it can be observed, different magnetic configurations are observed depending on the dot size.

In the micron diameter dots, stripe domains aligned along the W[001] direction are observed, similarly to the ones observed in continuous films of $Au_{0.67}Pt_{0.33}$/Co(0.8nm)/W(110), as discussed previously. On the other hand, in the smallest dots, either a black or a white contrast is observed, revealing that the magneti-

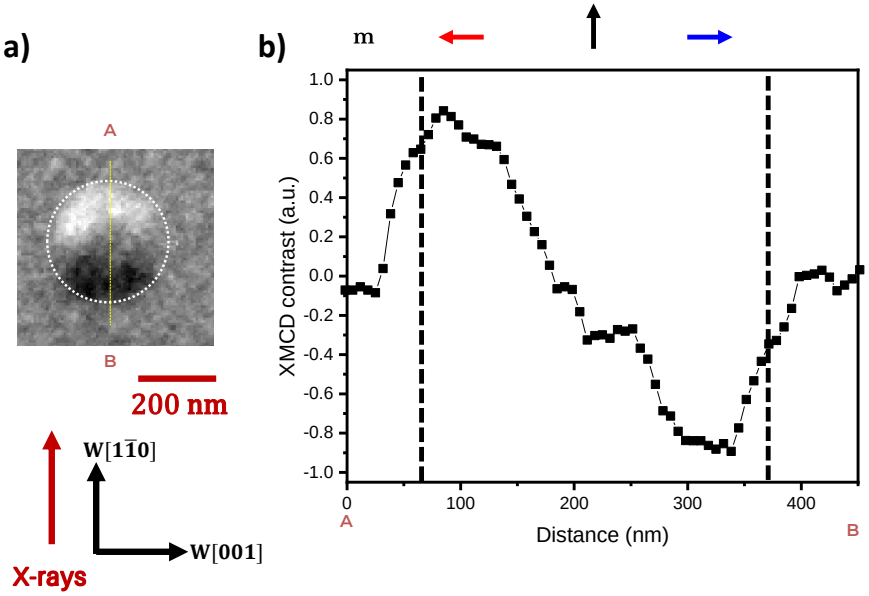

Figure 5.18: **Magnetic meron observed at room temperature and zero external magnetic field. a)** X-ray magnetic circular dichroism photoemission electron microscopy image of a 300 nm circular dot (white dashed lines) with the projection of the x-ray beam on the sample surface parallel to the W[$\bar{1}$10] direction **b)** Normalised XMCD contrast, between +1 and -1. Line scan of the magnetic contrast along the W[$\bar{1}$10] along the yellow line in **a)**. The black dashed lines represent the dot borders.

sation in these dots lies in-plane. Finally, in the dots with an average size between 300 nm and 400 nm, white/black contrast is observed (Red circles in Fig. 5.17).

Figure 5.18 **a)** shows a bubble domain in a 300 nm dot under no external field. Since x-rays impinge the sample at grazing incidence, a large contrast occurs when the magnetisation lies in-plane. Therefore, the magnetisation at top and bottom edges is in-plane (up/down, black/white contrast), while in the centre the magnetisation is out of plane (grey contrast). A linescan (from A to B in [Fig. 5.18 **a)**]) along the beam direction [Fig. 5.18 **b)**], shows a white-(bright grey)-black contrast, which corresponds to a right-handed meron profile.

Next, we studied the field-response of magnetic merons. Figure 5.19 shows the XMCD-PEEM images obtained during the application of an out-of-plane magnetic field. Three different geometries were studied: a 400 nm diameter circular dot (Fig. 5.19 top); a 300 nm diameter circular dot (Fig. 5.19 middle); a 325 nm effective diameter elliptical dot, elongated along the easy in-plane axis (Fig. 5.19 bottom).

At B_z =0 mT, a magnetic meron is stabilised in the 300 nm diameter circular dot

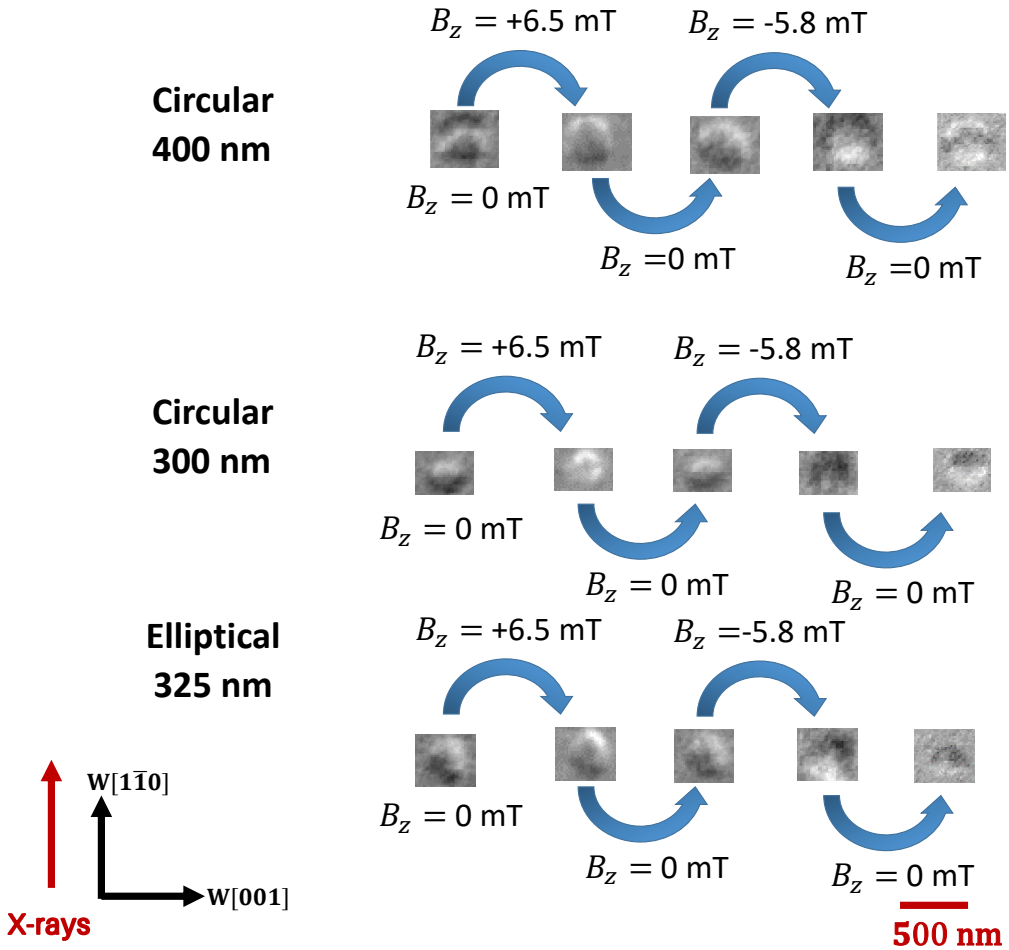

Figure 5.19: **Magnetic response of magnetic merons observed by x-ray magnetic circular dichroism photoemission electron microscopy for different dot sizes under an out-of plane magnetic field.**

and the 325 nm effective diameter elliptical dot while a stripe domain is stabilised in a 400 nm diameter circular dot. When a positive out-of plane field, B_z =6.44 mT is applied, the magnetic meron in the 300 nm diameter circular dot has disappeared while the one in the 325 nm effective diameter elliptical dot still remains. Finally, in the 400 nm diameter circular dot the stripe domain has transformed into a meron due to the increasing Zeeman energy induced by the positive field, which increases the grey contrast. Finally when the magnetic field is removed, the initial state is recovered in the 325 nm diameter elliptical dot and 300 nm circular dot, while in the case of the 400 nm

dot the meron state remains, suggesting that this is a metastable state.

Next, we applied a negative out-of plane magnetic field. The magnetic merons in the 400 nm diameter circular dot and the 325 nm diameter elliptical dot have switched their contrast, showing a white and black contrast at the top and bottom edges, respectively. Consequently, their polarisation has switched and therefore their topological charge has changed sign. Furthermore, the magnetic meron in the 300 nm diameter circular dot has annihilated. Finally, when the magnetic field is removed, the magnetic meron in the 400 nm diameter circular dot transforms into stripe domains, as in the initial state, but with opposite magnetisation at the top and bottom edges. The magnetic configuration in the 300 nm diameter circular dot and the 325 nm effective diameter elliptical dot transforms into a magnetic meron, as in the initial state, but with opposite magnetisation at the top and bottom edges.

In the following, we will proceed to discuss the stabilisation of magnetic merons with the help of micromagnetic simulations.

5.4.3 | Stabilisation of merons

While the stabilisation of magnetic skyrmions has been extensively investigated, this is not the case for magnetic merons.

Micromagnetic simulations

Micromagnetic 2D simulations were performed using the software package Mumax^3 [152; 153] in a system of 410 × 410 × 1 rectangular cells of size 1 nm×1 nm×0.8 nm, with only one cell across the film thickness, so that the magnetisation is assumed to be uniform along this direction as the film thickness is much lower than the exchange length. A magnetic meron, is used as initial state and allowed to relax in a 300 nm diameter nanodot. Unless otherwise said, A =16 pJ/m, M_s =1.15 MA/m, and α = 0.3 are used. Additionally, a DMI constant, either isotropic or anisotropic, and/or an in-plane anisotropy along the x-direction, can be introduced as well. For convenience, all the simulations were performed at T = 0 K, although temperature should play a significant role on the meron stabilisation. The topological charge of the dot is obtained as a direct output of Mumax^3. Two topological charges are computed by Mumax^3: The mathematical expression based on the spatial derivatives of the magnetisation (Eq. 5.5) and a lattice-based or geometrical approach for computing $\mathcal{Q}$ that does not require to rely on spatial derivatives [165]. Nevertheless, no significant difference between the two approaches are found (the largest difference between them being of 1%).

Stabilisation in systems with in-plane magnetisation

Figure 5.20 shows the topological charge phase diagram as function of the DMI strength,D and the uniaxial anisotropy, K_u. For each $[K_u, D]$ position, we have performed simulations for three different initial magnetisation configurations: in-plane uniform state, a magnetic meron, and a Néel skyrmion. A similar study has been performed by Siracusano et al. [166].

As it can be observed, when the DMI is not present, a collinear state is stabilised, either in-plane or out-of-plane depending on the strength of the out-of-plane anisotropy (Figure 5.20 **i)** or **vi)**).

For materials with in-plane magnetisation the DMI interaction is equivalent to an out-of-plane shape anisotropy. Consequently, depending on the strength of the uniaxial anisotropy and the DMI, different magnetic configurations can be found in nanodisks. When the DMI is low and the dipolar energy is much higher than the out-of-plane anisotropy energy, the minimisation of the dipolar energy is the main mechanism leading to the stabilisation of a circular vortex or a uniform in-plane magnetised state, with a topological charge equal to 0 and $\mathcal{Q} = \pm 1/2$ respectively. When increasing the DMI, the exchange and the DMI are the dominant interactions, stabilising therefore a collinear in-plane state with an out-of-plane tilting in the edges due to the DMI. Finally, when the DMI overcomes the dipolar and the exchange interactions, the DMI acts as a shape anisotropy stabilising a radial vortex. Finally, it must be noticed how when increasing either the DMI or the uniaxial anisotropy, leads to an increase of the tilting at the edges, increasing consequently the computed topological charge. Some representative states for different $[K_u, D]$ combinations are shown in Fig. 5.20.

Experimentally, radial vortexs have been observed by Karakas et al. [167] in $CoFeB/Pt$ multilayers, where the magnetisation lies in-plane $K_{\text{out}} \approx -50\,\text{kJ/m}^3$ and $D \approx 0.7\,\text{mJ/m}^2$, in agreement with the phase diagram shown above.

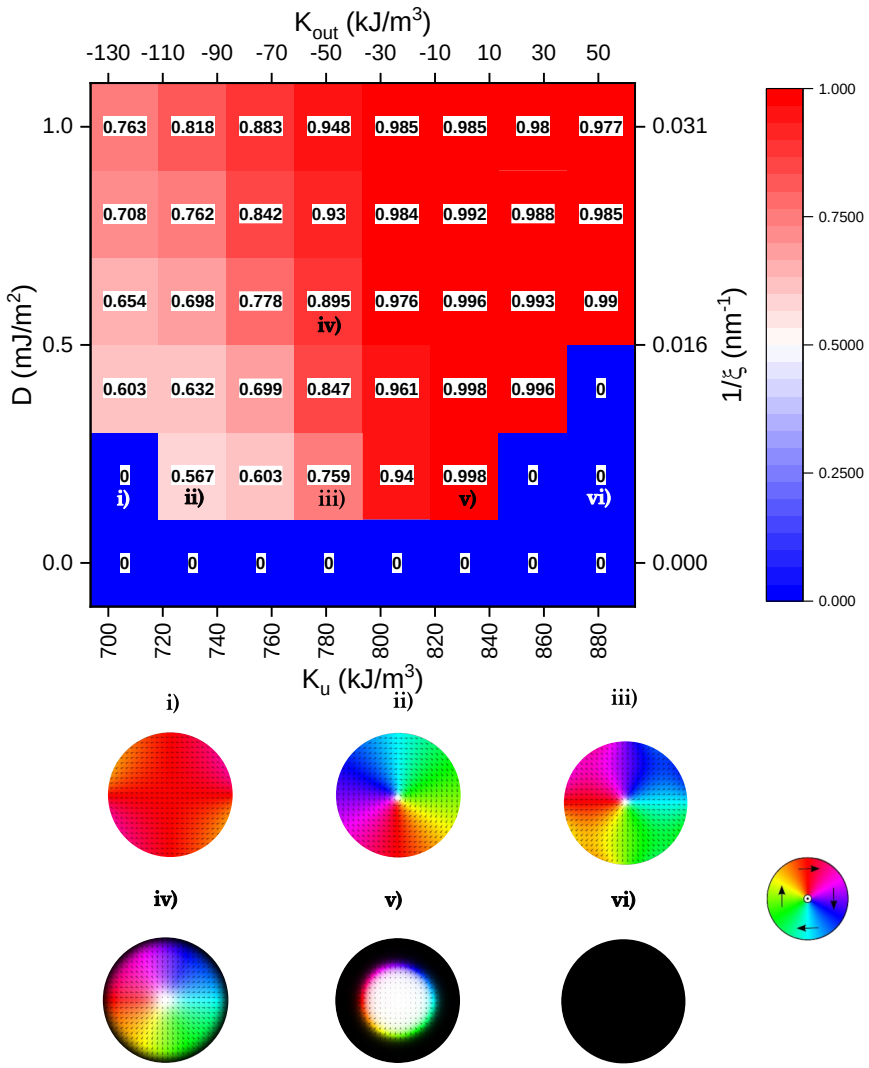

Figure 5.20: **Topological charge phase diagram in a 400nm diameter dot.** Computed topological charge as function of the DMI constant, D and the uniaxial anisotropy, K_u. Some representative magnetic configurations for different combinations in the phase diagram (labelled as i)-vi)). The colour code is the same as in Fig. 5.15.

Stabilisation in systems with out-of-plane magnetisation

In perpendicularly magnetised systems, a magnetic meron can be stabilised under specific conditions. Given the energy functional (Eq. 3.2), the Euler-Lagrange equations leads to the following boundary condition [16]:

$$\sin\theta(x) = \frac{\Delta}{\xi}, \tag{5.9}$$

where $\xi = \frac{2A}{D}$ is the cycloid length and Δ is the DW parameter defined as $\Delta = \sqrt{\frac{A}{K_{\text{out}}}}$. In order to have a magnetic meron, $\sin\theta(x) = 1$ in the periphery, which will occur then when $\xi \approx \Delta$. Note that Eq. 5.9 considers the dipolar energy as a local approximation. Micromagnetic simulations accounting for the full dipolar energy [16] reveals that the tilting at the border for the same Δ/ξ factor is indeed lower than the one predicted by Eq. 5.9.

Figure 5.21 shows the magnetic configurations for ξ =64 nm and different values of Δ, for a dot size of 400 nm. A magnetic configuration similar to the radial vortex stabilised in in-plane systems is observed. Nevertheless, we are in a perpendicularly magnetised system. It can be observed that as the DW parameter decreases (due to an increase of the out-of-plane anisotropy) i.e. Δ/ξ decreases, the core region increases until stabilising a magnetic Néel skyrmion. It is necessary to stress the fact that the $|m_z|$ component at the dot border is not zero but it is different from unity for Δ =64 nm.

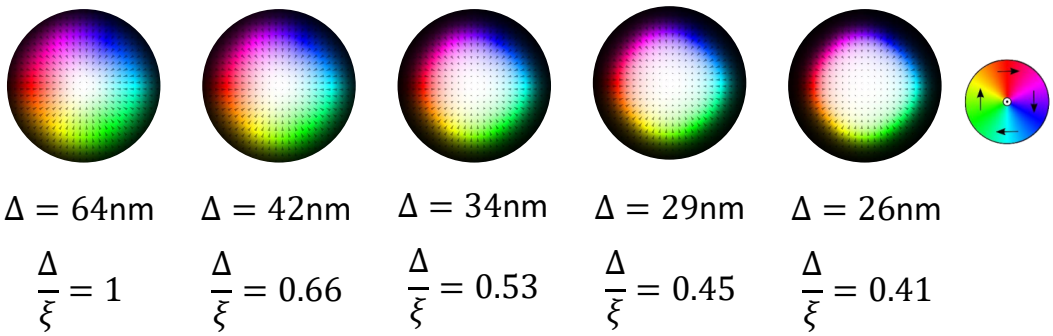

Figure 5.21: **Stabilised magnetic states for a fix spin cycloid length for different domain wall parameters.** Black means magnetisation into the plane and white means magnetisation out of the plane. The wheel represents the color code for in-plane magnetisation direction, red meaning magnetisation along positive x-direction and green meaning magnetisation along positive y direction. The spin cycloid length has been fixed to ξ= 64 nm.

Therefore, the polarity of such texture $\mathcal{P} \neq 1$, leading to a non-integer topological charge $\mathcal{Q}$. While for Δ <42 nm the $|m_z|$ component at the dot border is one, and therefore a magnetic skyrmion is stabilised.

Discussion on experimental results

Let's discuss now our experimental results. First, we need to determine whether the magnetisation is out-of-plane or in-plane. This, is inferred from the hysteresis loop obtained by polar MOKE as function of an out-of-plane magnetic field, which shows a S-shape with a not-maximum remanence. This is coherent with the micromagnetic parameters derived by BLS, where the effective out-of-plane anisotropy is close to zero. Therefore, the magnetisation in this region is perpendicular to the plane (out-of-plane).

Next, we need to examine the values of Δ and ξ. As the DW parameter Δ and the DMI are anisotropic, the boundary conditions are also anisotropic. For simplicity, we consider only the in-plane easy and hard axes, x and y respectively in Fig. 5.3). The results of Δ, ξ and Δ/ξ along the two directions are shown in Table 5.4. As observed, along the x-direction we fulfill the boundary condition while along the y-direction, no. Therefore we may expect an elliptical magnetic meron.

Figure 5.22 shows the magnetic configuration predicted by micromagnetic simulations using the experimental values (Table 5.3). For a 200 nm circular dot size, a uniform in-plane state, with the magnetisation along the easy in-plane axis, x-direction is found. For a 300 nm circular dot size, a magnetic meron with an elliptical core due to the anisotropic energies, with a topological charge equal to $\mathcal{Q} = 0.82$ is stabilised. Note that the computed topological charge is the sum of the whole dot, i.e. the magnetic meron and the edges. From the magnetic configuration in **b)** we can simulate the expected XMCD-PEEM contrast using Eq. 5.1 leading to Fig. 5.22 **c)** which is similar to the experimental one, Fig. 5.18.

Finally, for a 400 nm circular dot size (not shown in Fig. 5.22) a two-domain state is stabilised, which under the application of B_z =15 mT can be transformed into a magnetic meron, revealing that for this size the magnetic meron is *metastable*. These results

Table 5.4: **Derived domain wall parameter and cycloid length along the two main in-plane axes for $Au_{0.58}Pt_{0.42}$ /Co(0.75nm)/W(110).**

Δ_x [nm]	Δ_y [nm]	ξ_x [nm]	ξ_y [nm]	Δ_x/ξ_x	Δ_y/ξ_y
17±3	39±5	43±5	36 ±5	0.4±0.1	1.1±0.1

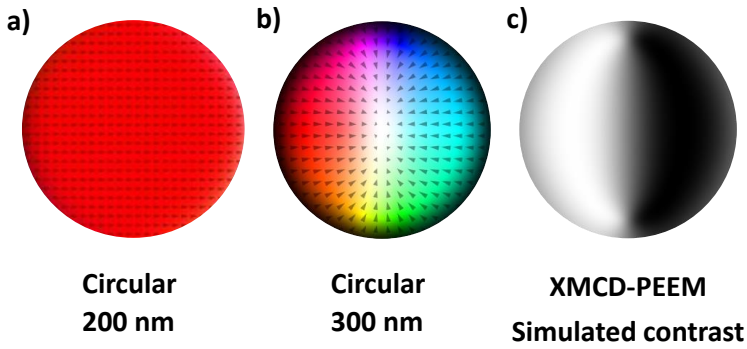

Figure 5.22: **Stabilised magnetic states with experimental values.**The colour code for **a)** and **b)** is the same as for Fig. 5.21. **c)** X-ray magnetic circular dichroism photoemission electron microscopy simulated contrast using Eq. 5.1 of the magnetic configuration **b)**. Experimental values are taken from Table 5.3.

are in line with the field-response of magnetic merons observed experimentally, Fig. 5.19.

To summarise, we have shown that while sharing similar magnetic configurations, radial vortexs and merons are stabilised in very different situations. Radial vortexs are stabilised in systems with an in-plane magnetisation with a DMI sufficiently large to overcome the exchange and dipolar interactions which promotes a collinear in-plane state. On the other hand, magnetic merons may be stabilised in perpendicularly magnetised films when the boundary conditions induced by the DMI allow it. This occur when the DW parameter, Δ is comparable to the cycloid length, $\xi = \frac{2A}{D}$. Experimentally, the values derived by BLS for the $Au_{0.58}Pt_{0.42}$ /Co(0.75nm)/W(110) stack, show that along the easy in-plane axis, we fulfill this condition, while it is not the case along the hard in-plane axis, leading consequently to the stabilisation of an elliptical meron.

6

Conclusions

The main aim of this PhD has been to study the relationship of the symmetry of the crystallographic structure and of the magnetic symmetry, in particular the one of the Dzyaloshinskii-Moriya interaction (DMI), on the stabilisation of different chiral magnetic textures in epitaxial magnetic thin films of $Au_{1-x}Pt_x/Co(t_{Co})/W(110)$.

In chapter 2 the main energies involved on the stabilisation of the different magnetic configurations have been introduced. A particular emphasis has been given to the magnetocrystalline anisotropy (MCA) in thin films, and the interfacial DMI symmetry, that is responsible for the stabilisation of different chiral magnetic textures in our stack due to the broken inversion symmetry and the large spin-orbit coupling.

In chapter 3 the different magnetic textures found in our system has been introduced. The one-dimensional model for the description of the statics and dynamics of chiral Néel domain walls (DWs) has been presented. Moreover, two-dimensional textures such as a skyrmions, anti-skyrmions and magnetic merons have been also introduced.

In Chapter 4, the characterisation of the crystallographic structure and the magnetic parameters as well as the field-driven dynamics of DWs is shown.

The crystal structure and symmetry was investigated by scanning tunneling microscopy, reflection high energy electron diffraction, and grazing X-ray diffraction (GXRD). The W(110) layer shows a very high quality in line with previous works [18; 111]. On the other hand, the Co(0001) layer, which grows layer-by-layer, creates a supercell on W(110) with the same lattice parameter along the $W[1\bar{1}0]$ direction, reducing its symmetry to a C_{2v} symmetry. Finally, the in-plane lattice parameter of the $Au_{1-x}Pt_x$ solid solution, is observed to decrease as the Pt content increases, following Vegard's law, but without modifying the Co strain, and therefore preserving the two-fold symmetry.

The magnetic parameters of the $Au_{1-x}Pt_x/Co/W(110)$ stack as function of the Pt content were investigated mainly with Brillouin light scattering (BLS). The interfacial anisotropy is found to follow Vegard's law, decreasing monotonously as the Pt content increases. On the other hand, the in-plane anisotropy is two-fold, as expected from the Neuman's principle, but with a value, K_{in} ≈60 kJ/m^3, slightly lower than in previous works [18; 116] in the same system. This value, is independent of the Pt content, consistent with the findings of GXRD where the Co in-plane strain was not modified by the Pt content of the capping layer.

Contrary to the interfacial MCA, the Néel-type DMI does not follow Vegard's law, as it increases non-monotonously with the Pt content up to a maximum value for x=0.6, but it drops above. This is in agreement with the results found by [147], explained by the linear variation of the *5d* orbitals of the $Au_{1-x}Pt_x$ capping layer, which results into a variation of the orbital hybridisation as a function of the Pt composition, with its maximum value located around at x=0.8 in their case. We associate this discrepancy to the reduction of the Fermi energy in our Co layer due to the Co strain. The anisotropy of the Néel-type DMI is also affected by the different composition of $Au_{1-x}Pt_x$. While for only Au, Au/Co/W(110), the largest DMI is along the easy-axis, when introducing a significant content of Pt, the largest DMI is along the hard in-plane axis. This indicates that the DMI induced by the Pt atoms, is perpendicular in direction, but not in sign, with respect to the one given by Au. Finally, by measuring in the BVW geometry, we have revealed the presence of the Bloch-type DMI due to the anisotropic Néel-type DMI.

Using the magnetic parameters determined by BLS, we have studied the field-driven DW motion for three different Pt content on the $Au_{1-x}Pt_x/Co(0.6)/W(110)$: x=0,x=0.15 and x=0.33. In the three cases we have combined 2D micromagnetic simulations with a 1D analytical model to understand the experimental curves. Overall a relatively good agreement between the experimental curves and the micromagnetic simulations and analytical model is found.

In Chapter 5, the different magnetic configurations stabilised in the $Au_{1-x}Pt_x/Co(t_{Co})/W(110)$ stack as function of the Co thickness and Au-to-Pt content have been investigated by MOKE microscopy and XMCD-PEEM.

For $Au/Co(t_{Co})/W(110)$ the magnetic domains show a circular shape, without any sign of anisotropy independently of the Co thickness. On the other hand, for $Au_{0.67}Pt_{0.33}/Co(t_{Co})/W(110)$ self organised stripe domains aligned along the hard in-plane axis, reducing his size as the Co thickness increases are observed. Such behaviour is explained by micromagnetic simulations and an analytical model, showing that as

the Pt content increases the anisotropy in the DW energy increases.

X-ray magnetic circular dichroism photoemission electron microscopy XMCD-PEEM shows that DWs oriented along the hard in-plane axis have a Néel internal structure. On the other hand, DWs oriented along the easy in-plane axis could not be characterised due to their short length and limited number,

The application of a weak perpendicular magnetic field leads to the transformation of the magnetic stripe domains into skyrmion bubbles with an elliptical shape and a size of about 100 nm. This elliptical shape can be explained in terms of the increase of the DW anisotropy energy as the Pt content increases, giving rise to circular skyrmion for $Au/Co(t_{Co})/W(110)$, and an elliptical skyrmion for $Au_{0.67}Pt_{0.33}/Co(t_{Co})/W(110)$. This is consistent with the results of micromagnetic simulations, where the ellipticity of the skyrmion, R_y/R_x is found to vary roughly as the DW anisotropy energy difference.

Finally, when increasing the Pt content, up to a point where the DW paramater Δ is equal the cycloid length, we observe that magnetic merons, equivalent to half-skyrmions, are observed in magnetic nanodots of 300 nm under no external magnetic field. Such textures are found to be extremely sensitive to different magnetic parameters such as the DMI, the magnetic anisotropy or the dot size, in line with the experimental observations and micromagnetic simulations. When an out-of-plane magnetic field, antiparallel to the meron core is applied, the magnetic meron switches its core polarity and therefore its topological charge.

We can therefore summarise the main outcomes of this work:

1. Observation of the Bloch-type DMI by BLS, only present in ultrathin films when the DMI is anisotropic

2. Observation of elliptical skyrmions by XMCD-PEEM, as well as understanding of their elliptical shape by means of micromagnetic simulations.

3. Observation of magnetic merons by XMCD-PEEM in magnetic nanodots, as well as the switching of their topological charge by the application of an out-of-plane magnetic field.

6.1 | Future Work

First, the study of the Néel- and Bloch-type DMI will be studied for a Au/Co/W(110) stack strained and relaxed. We expect to conclude either if the anisotropic DMI is coming from the interface symmetry C_{2v} in both cases, or it has his origin on the magnetic

symmetry, C_{2v} and C_{3v} for the strained and relaxed stack respectively. On the other hand, we expect also that the Bloch-type DMI in this system will be larger as the Néel-type DMI is lower in this system [18].

Second, we aim to substitute the W(110) buffer layer. Two approaches are possible, either changing the bcc-(110) or by using a solid solution which allow us to tune the lattice parameter of the W(110).

The first approach has the inconvenience of the limited number of heavy metals showing a two-fold symmetry, with a mismatch compatible with Co or Fe. Preliminary studies on Mo(110), reveal indeed a similar in-plane anisotropy and same chirality along the two main in-plane directions as the Au/Co interface dominates over the Co/Mo(110).

The last approach has the advantage of keeping the chemical nature of the interface relatively fixed, and just changing his crystal structure. This can be achieved by depositing an ultra-thin layer of W(110) on $V_{1-x}Nb_x(110)$ which allows to tune the lattice parameter of W(110). This has already been explored by Fruchart et al., by PLD [117]. This would allow to tune the Co(0001) lattice parameter and therefore the crystal strain. This would allow to tune the in-plane anisotropy, and the variation of the DMI chirality and strength due to the oscillatory behaviour of this interaction with the distance between the magnetic atoms as predicted by the Fert-Levy model. Indeed, such behaviour has been already observed in Co/Pt mulilayers under an external strain, resulting into the induction of an anisotropic DMI which evolves as function of the strain strength [168].

Finally, a XMCD-PEEM experiment is planned in June, 2021 for studying the magnetic meron along different in-plane directions in order to confirm his radial-type configuration.

References

[1] Ioan Mihai Miron, Gilles Gaudin, Stéphane Auffret, Bernard Rodmacq, Alain Schuhl, Stefania Pizzini, Jan Vogel, and Pietro Gambardella. Current-driven spin torque induced by the rashba effect in a ferromagnetic metal layer. *Nature materials*, 9(3):230–234, 2010.

[2] Ioan Mihai Miron, Thomas Moore, Helga Szambolics, Liliana Daniela Buda-Prejbeanu, Stéphane Auffret, Bernard Rodmacq, Stefania Pizzini, Jan Vogel, Marlio Bonfim, Alain Schuhl, et al. Fast current-induced domain-wall motion controlled by the rashba effect. *Nature materials*, 10(6):419–423, 2011.

[3] Kevin Garello, Ioan Mihai Miron, Can Onur Avci, Frank Freimuth, Yuriy Mokrousov, Stefan Blügel, Stéphane Auffret, Olivier Boulle, Gilles Gaudin, and Pietro Gambardella. Symmetry and magnitude of spin–orbit torques in ferromagnetic heterostructures. *Nature nanotechnology*, 8(8):587–593, 2013.

[4] Stuart Parkin and See-Hun Yang. Memory on the racetrack. *Nature nanotechnology*, 10(3):195–198, 2015.

[5] Stuart SP Parkin, Masamitsu Hayashi, and Luc Thomas. Magnetic domain-wall racetrack memory. *Science*, 320(5873):190–194, 2008.

[6] Albert Fert, Vincent Cros, and João Sampaio. Skyrmions on the track. *Nature nanotechnology*, 8(3):152–156, 2013.

[7] Anne Bernand-Mantel, Lorenzo Camosi, Alexis Wartelle, Nicolas Rougemaille, Michaël Darques, and Laurent Ranno. The skyrmion-bubble transition in a ferromagnetic thin film. *SciPost Phys*, 4(5):027, 2018.

[8] William Legrand, Nathan Ronceray, Nicolas Reyren, Davide Maccariello, Vincent Cros, and Albert Fert. Modeling the shape of axisymmetric skyrmions in magnetic multilayers. *Physical Review Applied*, 10(6):064042, 2018.

[9] Olivier Boulle, Jan Vogel, Hongxin Yang, Stefania Pizzini, Dayane de Souza Chaves, Andrea Locatelli, Tevfik Onur Menteş, Alessandro Sala, Liliana D Buda-Prejbeanu, Olivier Klein, et al. Room-temperature chiral magnetic skyrmions in ultrathin magnetic nanostructures. *Nature nanotechnology*, 11(5):449, 2016.

[10] Constance Moreau-Luchaire, Christoforos Moutafis, Nicolas Reyren, João Sampaio, CAF Vaz, N Van Horne, Karim Bouzehouane, K Garcia, C Deranlot, P Warnicke, et al. Additive interfacial chiral interaction in multilayers for stabilization of small individual skyrmions at room temperature. *Nature nanotechnology*, 11(5):444–448, 2016.

[11] Albert Fert, Nicolas Reyren, and Vincent Cros. Magnetic skyrmions: advances in physics and potential applications. *Nature Reviews Materials*, 2(7):1–15, 2017.

[12] Xichao Zhang, Motohiko Ezawa, and Yan Zhou. Magnetic skyrmion logic gates: conversion, duplication and merging of skyrmions. *Scientific reports*, 5(1):1–8, 2015.

[13] I Dzyaloshinsky. A thermodynamic theory of "weak" ferromagnetism of antiferromagnetics. *Journal of Physics and Chemistry of Solids*, 4(4):241–255, 1958.

[14] Tôru Moriya. Anisotropic superexchange interaction and weak ferromagnetism. *Physical Review*, 120(1):91, 1960.

[15] A Thiaville, Y Nakatani, J Miltat, and Y Suzuki. Micromagnetic understanding of current-driven domain wall motion in patterned nanowires. *EPL (Europhysics Letters)*, 69(6):990, 2005.

[16] S Rohart and A Thiaville. Skyrmion confinement in ultrathin film nanostructures in the presence of dzyaloshinskii-moriya interaction. *Physical Review B*, 88(18):184422, 2013.

[17] Markus Hoffmann, Bernd Zimmermann, Gideon P Müller, Daniel Schürhoff, Nikolai S Kiselev, Christof Melcher, and Stefan Blügel. Antiskyrmions stabilized at interfaces by anisotropic dzyaloshinskii-moriya interactions. *Nature communications*, 8(1):1–9, 2017.

[18] Lorenzo Camosi, Stanislas Rohart, Olivier Fruchart, Stefania Pizzini, Mohamed Belmeguenai, Yves Roussigné, Andreï Stashkevich, Salim Mourad Cherif, Laurent Ranno, Maurizio De Santis, et al. Anisotropic dzyaloshinskii-moriya interaction in ultrathin epitaxial au/co/w (110). *Physical Review B*, 95(21):214422, 2017.

[19] Lorenzo Camosi, Nicolas Rougemaille, Olivier Fruchart, Jan Vogel, and Stanislas Rohart. Micromagnetics of antiskyrmions in ultrathin films. *Physical Review B*, 97(13):134404, 2018.

[20] Ajaya K Nayak, Vivek Kumar, Tianping Ma, Peter Werner, Eckhard Pippel, Roshnee Sahoo, Franoise Damay, Ulrich K Rößler, Claudia Felser, and Stuart SP Parkin. Magnetic antiskyrmions above room temperature in tetragonal heusler materials. *Nature*, 548(7669):561–566, 2017.

[21] Praveen Vir, Nitesh Kumar, Horst Borrmann, Bayardulam Jamijansuren, Guido Kreiner, Chandra Shekhar, and Claudia Felser. Tetragonal superstructure of the antiskyrmion hosting heusler compound mn1. 4ptsn. *Chemistry of Materials*, 31(15):5876–5880, 2019.

[22] Tianping Ma, Ankit K Sharma, Rana Saha, Abhay K Srivastava, Peter Werner, Praveen Vir, Vivek Kumar, Claudia Felser, and Stuart SP Parkin. Tunable magnetic antiskyrmion size and helical period from nanometers to micrometers in a d2d heusler compound. *Advanced Materials*, 32(28):2002043, 2020.

[23] Kosuke Karube, Licong Peng, Jan Masell, Xiuzhen Yu, Fumitaka Kagawa, Yoshinori Tokura, and Yasujiro Taguchi. Room-temperature antiskyrmions and sawtooth surface textures in a non-centrosymmetric magnet with s 4 symmetry. *Nature Materials*, pages 1–6, 2021.

[24] AN Bogdanov and DA Yablonskii. Thermodynamically stable" vortices" in magnetically ordered crystals. the mixed state of magnets. *Zh. Eksp. Teor. Fiz*, 95:182, 1989.

[25] Siying Huang, Chao Zhou, Gong Chen, Hongyi Shen, Andreas K Schmid, Kai Liu, and Yizheng Wu. Stabilization and current-induced motion of antiskyrmion in the presence of anisotropic dzyaloshinskii-moriya interaction. *Physical Review B*, 96(14):144412, 2017.

[26] Niels Bohr. *Studier over metallernes elektrontheori*. Thaning et Appel in Komm., 1911.

[27] H-J Van Leeuwen. Problemes de la théorie électronique du magnétisme. *J. Phys. Radium*, 2(12):361–377, 1921.

[28] LALE Landau and Es Lifshitz. On the theory of the dispersion of magnetic permeability in ferromagnetic bodies. *Phys. Z. Sowjetunion*, 8(153):101–114, 1935.

[29] Felix Bloch. Zur theorie des austauschproblems und der remanenzerscheinung der ferromagnetika. *Zeitschrift für Physik*, 74(5-6):295–335, 1932.

[30] William Fuller Brown Jr. Theory of the approach to magnetic saturation. *Physical Review*, 58(8):736, 1940.

[31] X Liu, MM Steiner, R Sooryakumar, GA Prinz, RFC Farrow, and G Harp. Exchange stiffness, magnetization, and spin waves in cubic and hexagonal phases of cobalt. *Physical Review B*, 53(18):12166, 1996.

[32] P Grünberg, CM Mayr, W Vach, and M Grimsditch. Determination of magnetic parameters by means of brillouinscattering. examples: Fe, ni, ni0. 8fe0. 2. *Journal of Magnetism and Magnetic Materials*, 28(3):319–325, 1982.

[33] John MD Coey. *Magnetism and magnetic materials*. Cambridge University Press, 2010.

[34] Alberto P Guimarães and Alberto Passos Guimaraes. *Principles of nanomagnetism*, volume 7. Springer, 2009.

[35] Andrew Taylor Galkiewicz. *Magnetic domain wall dynamics in patterned nanowires*. PhD thesis, UNIVERSITY OF MINNESOTA, 2015.

[36] Frank Herman and Sherwood Skillman. *Atomic structure calculations*. Prentice-Hall, 1963.

[37] Louis Néel. L'anisotropie superficielle des substances ferromagnétiques. *Comptes Rendus Hebdomadaires Des Seances De L Academie Des Sciences*, 237(23):1468–1470, 1953.

[38] Mathias Getzlaff. *Fundamentals of magnetism*. Springer Science & Business Media, 2007.

[39] MT Johnson, PJH Bloemen, FJA Den Broeder, and JJ De Vries. Magnetic anisotropy in metallic multilayers. *Reports on Progress in Physics*, 59(11):1409, 1996.

[40] Patrick Bruno. Dipolar magnetic surface anisotropy in ferromagnetic thin films with interfacial roughness. *Journal of applied physics*, 64(6):3153–3156, 1988.

[41] A Fert and Peter M Levy. Role of anisotropic exchange interactions in determining the properties of spin-glasses. *Physical Review Letters*, 44(23):1538, 1980.

[42] A Fert. Magnetic and transport properties of metallic multilayers. In *Materials Science Forum*, volume 59, pages 439–480. Trans Tech Publ, 1990.

[43] Matthias Bode, M Heide, K Von Bergmann, P Ferriani, S Heinze, G Bihlmayer, A Kubetzka, O Pietzsch, S Blügel, and R Wiesendanger. Chiral magnetic order at surfaces driven by inversion asymmetry. *Nature*, 447(7141):190–193, 2007.

[44] P Ferriani, K Von Bergmann, EY Vedmedenko, S Heinze, M Bode, M Heide, G Bihlmayer, S Blügel, and R Wiesendanger. Atomic-scale spin spiral with a unique rotational sense: Mn monolayer on w (001). *Physical review letters*, 101(2):027201, 2008.

[45] SV Grigoriev, Yu O Chetverikov, D Lott, and A Schreyer. Field induced chirality in the helix structure of dy/y multilayer films and experimental evidence for dzyaloshinskii-moriya interaction on the interfaces. *Physical review letters*, 100(19):197203, 2008.

[46] M Heide, G Bihlmayer, and S Blügel. Dzyaloshinskii-moriya interaction accounting for the orientation of magnetic domains in ultrathin films: Fe/w (110). *Physical Review B*, 78(14):140403, 2008.

[47] A Crépieux and Claudine Lacroix. Dzyaloshinsky–moriya interactions induced by symmetry breaking at a surface. *Journal of magnetism and magnetic materials*, 182(3):341–349, 1998.

[48] AN Bogdanov and UK Rößler. Chiral symmetry breaking in magnetic thin films and multilayers. *Physical review letters*, 87(3):037203, 2001.

[49] L Berger. Exchange interaction between ferromagnetic domain wall and electric current in very thin metallic films. *Journal of Applied Physics*, 55(6):1954–1956, 1984.

[50] John C Slonczewski et al. Current-driven excitation of magnetic multilayers. *Journal of Magnetism and Magnetic Materials*, 159(1):L1, 1996.

[51] Shufeng Zhang and Z Li. Roles of nonequilibrium conduction electrons on the magnetization dynamics of ferromagnets. *Physical review letters*, 93(12):127204, 2004.

[52] Gen Tatara and Hiroshi Kohno. Theory of current-driven domain wall motion: Spin transfer versus momentum transfer. *Physical review letters*, 92(8):086601, 2004.

[53] Mikhail I Dyakonov and VI Perel. Current-induced spin orientation of electrons in semiconductors. *Physics Letters A*, 35(6):459–460, 1971.

[54] JE Hirsch. Spin hall effect. *Physical Review Letters*, 83(9):1834, 1999.

[55] Jairo Sinova, Dimitrie Culcer, Qian Niu, NA Sinitsyn, T Jungwirth, and Allan H MacDonald. Universal intrinsic spin hall effect. *Physical review letters*, 92(12):126603, 2004.

[56] AV Khvalkovskiy, V Cros, D Apalkov, V Nikitin, M Krounbi, KA Zvezdin, A Anane, J Grollier, and A Fert. Matching domain-wall configuration and spin-orbit torques for efficient domain-wall motion. *Physical Review B*, 87(2):020402, 2013.

[57] Victor M Edelstein. Spin polarization of conduction electrons induced by electric current in two-dimensional asymmetric electron systems. *Solid State Communications*, 73(3):233–235, 1990.

[58] Yu A Bychkov and Emmanuel I Rashba. Oscillatory effects and the magnetic susceptibility of carriers in inversion layers. *Journal of physics C: Solid state physics*, 17(33):6039, 1984.

[59] Yu A Bychkov and É I Rashba. Properties of a 2d electron gas with lifted spectral degeneracy. *JETP lett*, 39(2):78, 1984.

[60] YZ Wu, C Won, A Scholl, A Doran, HW Zhao, XF Jin, and ZQ Qiu. Magnetic stripe domains in coupled magnetic sandwiches. *Physical review letters*, 93(11):117205, 2004.

[61] André Thiaville, Stanislas Rohart, Émilie Jué, Vincent Cros, and Albert Fert. Dynamics of dzyaloshinskii domain walls in ultrathin magnetic films. *EPL (Europhysics Letters)*, 100(5):57002, 2012.

[62] G Chen, J Zhu, A Quesada, J Li, AT N'Diaye, Y Huo, TP Ma, Y Chen, HY Kwon, C Won, et al. Novel chiral magnetic domain wall structure in fe/ni/cu (001) films. *Physical review letters*, 110(17):177204, 2013.

[63] J-P Tetienne, T Hingant, LJ Martínez, S Rohart, André Thiaville, L Herrera Diez, K Garcia, J-P Adam, J-V Kim, J-F Roch, et al. The nature of domain walls in ultrathin ferromagnets revealed by scanning nanomagnetometry. *Nature communications*, 6(1):1–6, 2015.

[64] SV Tarasenko, A Stankiewicz, VV Tarasenko, and J Ferré. Bloch wall dynamics in ultrathin ferromagnetic films. *Journal of magnetism and magnetic materials*, 189(1):19–24, 1998.

[65] AP Malozemoff and JC Slonczewski. *Magnetic Domain Walls in Bubble Materials: Advances in Materials and Device Research*, volume 1. Academic press, 2016.

[66] Werner Döring. Über die trägheit der wände zwischen weißschen bezirken. *Zeitschrift für Naturforschung A*, 3(7):373–379, 1948.

[67] Hiroshi Kohno and Gen Tatara. Chapter 5 - theoretical aspects of current-driven magnetization dynamics. In Teruya Shinjo, editor, *Nanomagnetism and Spintronics*, pages 189 – 229. Elsevier, Amsterdam, 2009.

[68] André Thiaville and Yoshinobu Nakatani. Domain-wall dynamics in nanowiresand nanostrips. In *Spin dynamics in confined magnetic structures III*, pages 161–205. Springer, 2006.

[69] O Boulle, S Rohart, LD Buda-Prejbeanu, E Jué, IM Miron, Stefania Pizzini, Jan Vogel, G Gaudin, and A Thiaville. Domain wall tilting in the presence of the dzyaloshinskii-moriya interaction in out-of-plane magnetized magnetic nanotracks. *Physical review letters*, 111(21):217203, 2013.

[70] S. Ali Nasseri, Bhaskarjyoti Sarma, Gianfranco Durin, and Claudio Serpico. Analytical modelling of magnetic dw motion. *Physics Procedia*, 75:974 – 985, 2015. 20th International Conference on Magnetism, ICM 2015.

[71] Viola Krizakova, J Peña Garcia, Jan Vogel, Nicolas Rougemaille, Dayane de Souza Chaves, Stefania Pizzini, and André Thiaville. Study of the velocity plateau of dzyaloshinskii domain walls. *Physical Review B*, 100(21):214404, 2019.

[72] Norman L Schryer and Laurence R Walker. The motion of 180 domain walls in uniform dc magnetic fields. *Journal of Applied Physics*, 45(12):5406–5421, 1974.

[73] JC Slonczewski. Dynamics of magnetic domain walls. In *AIP Conference Proceedings*, volume 5, pages 170–174. American Institute of Physics, 1972.

[74] Jose Peña Garcia, Aymen Fassatoui, Marlio Bonfim, Jan Vogel, André Thiaville, and Stefania Pizzini. Magnetic domain wall dynamics in the precessional regime: Influence of the dzyaloshinskii-moriya interaction. *Physical Review B*, 104(1):014405, 2021.

[75] Thai Ha Pham, J Vogel, J Sampaio, M Vaňatka, J-C Rojas-Sánchez, M Bonfim, DS Chaves, F Choueikani, P Ohresser, E Otero, et al. Very large domain wall velocities in pt/co/gdox and pt/co/gd trilayers with dzyaloshinskii-moriya interaction. *EPL (Europhysics Letters)*, 113(6):67001, 2016.

[76] Hongxin Yang, André Thiaville, Stanislas Rohart, Albert Fert, and Mairbek Chshiev. Anatomy of dzyaloshinskii-moriya interaction at co/pt interfaces. *Physical review letters*, 115(26):267210, 2015.

[77] Dayane de Souza Chaves, Fernando Ajejas, Viola Křižáková, Jan Vogel, and Stefania Pizzini. Oxidation dependence of the dzyaloshinskii-moriya interaction in pt/co/m o x trilayers (m= al or gd). *Physical Review B*, 99(14):144404, 2019.

[78] Fernando Ajejas, Viola Křižáková, Dayane de Souza Chaves, Jan Vogel, Paolo Perna, Ruben Guerrero, Adrian Gudin, Julio Camarero, and Stefania Pizzini. Tuning domain wall velocity with dzyaloshinskii-moriya interaction. *Applied Physics Letters*, 111(20):202402, 2017.

[79] Yoko Yoshimura, Kab-Jin Kim, Takuya Taniguchi, Takayuki Tono, Kohei Ueda, Ryo Hiramatsu, Takahiro Moriyama, Keisuke Yamada, Yoshinobu Nakatani, and Teruo Ono. Soliton-like magnetic domain wall motion induced by the interfacial dzyaloshinskii–moriya interaction. *Nature Physics*, 12(2):157–161, 2016.

[80] Soong-Geun Je, Duck-Ho Kim, Sang-Cheol Yoo, Byoung-Chul Min, Kyung-Jin Lee, and Sug-Bong Choe. Asymmetric magnetic domain-wall motion by the dzyaloshinskii-moriya interaction. *Physical Review B*, 88(21):214401, 2013.

[81] A Hrabec, NA Porter, A Wells, MJ Benitez, G Burnell, S McVitie, D McGrouther, TA Moore, and CH Marrows. Measuring and tailoring the dzyaloshinskii-moriya interaction in perpendicularly magnetized thin films. *Physical Review B*, 90(2):020402, 2014.

[82] Duck-Ho Kim, Dae-Yun Kim, Sang-Cheol Yoo, Byoung-Chul Min, and Sug-Bong Choe. Universality of dzyaloshinskii-moriya interaction effect over domain-wall creep and flow regimes. *Physical Review B*, 99(13):134401, 2019.

[83] M Vaňatka, Juan-Carlos Rojas-Sánchez, Jan Vogel, Marlio Bonfim, M Belmeguenai, Y Roussigné, A Stashkevich, A Thiaville, and S Pizzini. Velocity asymmetry of dzyaloshinskii domain walls in the creep and flow regimes. *Journal of Physics: Condensed Matter*, 27(32):326002, 2015.

[84] O Boulle, LD Buda-Prejbeanu, E Jué, IM Miron, and G Gaudin. Current induced domain wall dynamics in the presence of spin orbit torques. *Journal of Applied Physics*, 115(17):17D502, 2014.

[85] Satoru Emori and Geoffrey SD Beach. Enhanced current-induced domain wall motion by tuning perpendicular magnetic anisotropy. *Applied Physics Letters*, 98(13):132508, 2011.

[86] Satoru Emori, Uwe Bauer, Sung-Min Ahn, Eduardo Martinez, and Geoffrey SD Beach. Current-driven dynamics of chiral ferromagnetic domain walls. *Nature materials*, 12(7):611–616, 2013.

[87] T Aetal Moore, IM Miron, G Gaudin, G Serret, S Auffret, B Rodmacq, A Schuhl, Stefania Pizzini, Jan Vogel, and M Bonfim. High domain wall velocities induced by current in ultrathin pt/co/alox wires with perpendicular magnetic anisotropy. *Applied Physics Letters*, 93(26):262504, 2008.

[88] Toshiki Gushi, Matic Jovicevic Klug, Jose Pena Garcia, Sambit Ghosh, Jean-Philippe Attané, Hanako Okuno, Olivier Fruchart, Jan Vogel, Takashi Suemasu, Stefania Pizzini, et al. Large current driven domain wall mobility and gate tuning of coercivity in ferrimagnetic mn4n thin films. *Nano letters*, 19(12):8716–8723, 2019.

[89] Naoto Nagaosa and Yoshinori Tokura. Topological properties and dynamics of magnetic skyrmions. *Nature nanotechnology*, 8(12):899–911, 2013.

[90] Jiadong Zang, Vincent Cros, and Axel Hoffmann. *Topology in Magnetism*, volume 192. Springer, 2018.

[91] Tony Hilton Royle Skyrme. A unified field theory of mesons and baryons. *Nuclear Physics*, 31:556–569, 1962.

[92] A Bogdanov and A Hubert. Thermodynamically stable magnetic vortex states in magnetic crystals. *Journal of magnetism and magnetic materials*, 138(3):255–269, 1994.

[93] A Bogdanov and A Hubert. The properties of isolated magnetic vortices. *physica status solidi (b)*, 186(2):527–543, 1994.

[94] XZ Yu, Naoya Kanazawa, Yoshinori Onose, K Kimoto, WZ Zhang, Shintaro Ishiwata, Yoshio Matsui, and Yoshinori Tokura. Near room-temperature formation of a skyrmion crystal in thin-films of the helimagnet fege. *Nature materials*, 10(2):106–109, 2011.

[95] Xichao Zhang, Yan Zhou, Kyung Mee Song, Tae-Eon Park, Jing Xia, Motohiko Ezawa, Xiaoxi Liu, Weisheng Zhao, Guoping Zhao, and Seonghoon Woo. Skyrmion-electronics: writing, deleting, reading and processing magnetic skyrmions toward spintronic applications. *Journal of Physics: Condensed Matter*, 32(14):143001, 2020.

[96] Roland Wiesendanger. Nanoscale magnetic skyrmions in metallic films and multilayers: a new twist for spintronics. *Nature Reviews Materials*, 1(7):1–11, 2016.

[97] Wang Kang, Yangqi Huang, Xichao Zhang, Yan Zhou, and Weisheng Zhao. Skyrmion-electronics: An overview and outlook. *Proceedings of the IEEE*, 104(10):2040–2061, 2016.

[98] Giovanni Finocchio, Felix Büttner, Riccardo Tomasello, Mario Carpentieri, and Mathias Kläui. Magnetic skyrmions: from fundamental to applications. *Journal of Physics D: Applied Physics*, 49(42):423001, 2016.

[99] Wataru Koshibae, Yoshio Kaneko, Junichi Iwasaki, Masashi Kawasaki, Yoshinori Tokura, and Naoto Nagaosa. Memory functions of magnetic skyrmions. *Japanese Journal of Applied Physics*, 54(5):053001, 2015.

[100] Pramey Upadhyaya, Guoqiang Yu, Pedram Khalili Amiri, and Kang L Wang. Electric-field guiding of magnetic skyrmions. *Physical Review B*, 92(13):134411, 2015.

[101] Yangqi Huang, Wang Kang, Xichao Zhang, Yan Zhou, and Weisheng Zhao. Magnetic skyrmion-based synaptic devices. *Nanotechnology*, 28(8):08LT02, 2017.

[102] Kyung Mee Song, Jae-Seung Jeong, Biao Pan, Xichao Zhang, Jing Xia, Sunkyung Cha, Tae-Eon Park, Kwangsu Kim, Simone Finizio, Jörg Raabe, et al. Skyrmion-based artificial synapses for neuromorphic computing. *Nature Electronics*, 3(3):148–155, 2020.

[103] Sebastian Mühlbauer, Benedikt Binz, F Jonietz, Christian Pfleiderer, Achim Rosch, Anja Neubauer, Robert Georgii, and Peter Böni. Skyrmion lattice in a chiral magnet. *Science*, 323(5916):915–919, 2009.

[104] XZ Yu, Yoshinori Onose, Naoya Kanazawa, JH Park, JH Han, Yoshio Matsui, Naoto Nagaosa, and Yoshinori Tokura. Real-space observation of a two-dimensional skyrmion crystal. *Nature*, 465(7300):901–904, 2010.

[105] W Münzer, A Neubauer, T Adams, S Mühlbauer, C Franz, F Jonietz, R Georgii, P Böni, B Pedersen, M Schmidt, et al. Skyrmion lattice in the doped semiconductor fe 1- x co x si. *Physical Review B*, 81(4):041203, 2010.

[106] Stefan Heinze, Kirsten Von Bergmann, Matthias Menzel, Jens Brede, André Kubetzka, Roland Wiesendanger, Gustav Bihlmayer, and Stefan Blügel. Spontaneous atomic-scale magnetic skyrmion lattice in two dimensions. *Nature Physics*, 7(9):713–718, 2011.

[107] Seonghoon Woo, Kai Litzius, Benjamin Krüger, Mi-Young Im, Lucas Caretta, Kornel Richter, Maxwell Mann, Andrea Krone, Robert M Reeve, Markus Weigand, et al. Observation of room-temperature magnetic skyrmions and their current-driven dynamics in ultrathin metallic ferromagnets. *Nature materials*, 15(5):501–506, 2016.

[108] Felix Büttner, Ivan Lemesh, and Geoffrey SD Beach. Theory of isolated magnetic skyrmions: From fundamentals to room temperature applications. *Scientific reports*, 8(1):1–12, 2018.

[109] AA Belavin and AM Polyakov. Metastable states of two-dimensional isotropic ferromagnets. *JETP lett*, 22(10):245–248, 1975.

[110] XZ Yu, W Koshibae, Y Tokunaga, K Shibata, Y Taguchi, N Nagaosa, and Y Tokura. Transformation between meron and skyrmion topological spin textures in a chiral magnet. *Nature*, 564(7734):95–98, 2018.

[111] Olivier Fruchart, Pierre-Olivier Jubert, Mustafa Eleoui, Fabien Cheynis, Bogdana Borca, Philippe David, Valérie Santonacci, Annick Liénard, Manabu Hasegawa, and Claire Meyer. Growth modes of fe (110) revisited: a contribution of self-assembly to magnetic materials. *Journal of Physics: Condensed Matter*, 19(5):053001, 2007.

[112] John E Mahan, Kent M Geib, GY Robinson, and Robert G Long. A review of the geometrical fundamentals of reflection high-energy electron diffraction with application to silicon surfaces. *Journal of Vacuum Science & Technology A: Vacuum, Surfaces, and Films*, 8(5):3692–3700, 1990.

[113] Ayahiko Ichimiya and Philip I Cohen. *Reflection high-energy electron diffraction*. Cambridge University Press, 2004.

[114] Shuji Hasegawa. Reflection high-energy electron diffraction. *Characterization of Materials*, 2012.

[115] O Fruchart, S Jaren, and J Rothman. Growth modes of w and mo thin epitaxial (110) films on (1120) sapphire. *Applied surface science*, 135(1):218–232, 1998.

[116] H Fritzsche, J Kohlhepp, and U Gradmann. Epitaxial strain and magnetic anisotropy in ultrathin co films on w (110). *Physical Review B*, 51(22):15933, 1995.

[117] Olivier Fruchart, Anthony Rousseau, Didier Schmaus, A l'Hoir, Richard Haettel, and Luc Ortega. Epitaxial refractory-metal buffer layers with a chemical gradient for adjustable lattice parameter and controlled chemical interface. *Applied Physics Letters*, 98(13):131906, 2011.

[118] U Köhler, C Jensen, C Wolf, AC Schindler, L Brendel, and DE Wolf. Investigation of homoepitaxial growth on bcc surfaces with stm and kinetic monte carlo simulation. *Surface science*, 454:676–680, 2000.

[119] Martin Albrecht, Helmut Fritzsche, and Ulrich Gradmann. Kinetic facetting in homoepitaxy of fe (110) on fe (110). *Surface science*, 294(1-2):1–9, 1993.

[120] H Knoppe and E Bauer. Electronic structure of ultrathin cobalt films on w (110). *Physical Review B*, 48(3):1794, 1993.

[121] JG Ociepa, Peter J Schultz, K Griffiths, and PR Norton. Re-emitted positron energy spectroscopy from thin co films on w (110). *Surface Science*, 225(3):281–291, 1990.

[122] M Pratzer, HJ Elmers, and M Getzlaff. Heteroepitaxial growth of co on w (110) investigated by scanning tunneling microscopy. *Physical Review B*, 67(15):153405, 2003.

[123] Z Nishiyama. X-ray investigation of the mechanism of the transformation from face centered cubic lattice to body centered cubic. *Sci. Rep. Tohoku Univ.*, 23:637, 1934.

[124] Günter Wassermann. Einfluß der α-γ-umwandlung eines irreversiblen nickelstahls auf kristallorientierung und zugfestigkeit. *Archiv für das Eisenhüttenwesen*, 6(8):347–351, 1933.

[125] A Wawro, Z Kurant, M Tekielak, P Nawrocki, E Milińska, A Pietruczik, M Wójcik, P Mazalski, J Kanak, K Ollefs, et al. Engineering the magnetic anisotropy of an ultrathin co layer sandwiched between films of mo or au. *Journal of Physics D: Applied Physics*, 50(21):215004, 2017.

[126] Robert Cahn. Togetherness. *Advanced Materials*, 3(10):472–473, 1991.

[127] Lars Vegard. Die konstitution der mischkristalle und die raumfüllung der atome. *Zeitschrift für Physik*, 5(1):17–26, 1921.

[128] Alan R Denton and Neil W Ashcroft. Vegard's law. *Physical review A*, 43(6):3161, 1991.

[129] H Bulou, A Barbier, G Renaud, B Carrière, R Baudoing-Savois, and JP Deville. Structural investigation of the ptco (0001) interface by gixs. *Surface science*, 377:90–93, 1997.

[130] L Udvardi and L Szunyogh. Chiral asymmetry of the spin-wave spectra in ultrathin magnetic films. *Physical review letters*, 102(20):207204, 2009.

[131] D Cortés-Ortuño and P Landeros. Influence of the dzyaloshinskii–moriya interaction on the spin-wave spectra of thin films. *Journal of Physics: Condensed Matter*, 25(15):156001, 2013.

[132] Jung-Hwan Moon, Soo-Man Seo, Kyung-Jin Lee, Kyoung-Whan Kim, Jisu Ryu, Hyun-Woo Lee, Robert D McMichael, and Mark D Stiles. Spin-wave propagation in the presence of interfacial dzyaloshinskii-moriya interaction. *Physical Review B*, 88(18):184404, 2013.

[133] Kh Zakeri, Yu Zhang, J Prokop, T-H Chuang, N Sakr, Wen-Xin Tang, and J Kirschner. Asymmetric spin-wave dispersion on fe (110): direct evidence of the dzyaloshinskii-moriya interaction. *Physical review letters*, 104(13):137203, 2010.

[134] Kai Di, Vanessa Li Zhang, Hock Siah Lim, Ser Choon Ng, Meng Hau Kuok, Jiawei Yu, Jungbum Yoon, Xuepeng Qiu, and Hyunsoo Yang. Direct observation of the dzyaloshinskii-moriya interaction in a pt/co/ni film. *Physical review letters*, 114(4):047201, 2015.

[135] Mohamed Belmeguenai, Jean-Paul Adam, Yves Roussigné, Sylvain Eimer, Thibaut Devolder, Joo-Von Kim, Salim Mourad Cherif, Andrey Stashkevich, and André Thiaville. Interfacial dzyaloshinskii-moriya interaction in perpendicularly magnetized pt/co/alo x ultrathin films measured by brillouin light spectroscopy. *Physical Review B*, 91(18):180405, 2015.

[136] Jaehun Cho, Nam-Hui Kim, Sukmock Lee, June-Seo Kim, Reinoud Lavrijsen, Aurelie Solignac, Yuxiang Yin, Dong-Soo Han, Niels JJ Van Hoof, Henk JM Swagten, et al. Thickness dependence of the interfacial dzyaloshinskii–moriya interaction in inversion symmetry broken systems. *Nature communications*, 6(1):1–7, 2015.

[137] Mitsuo Kataoka. Spin waves in systems with long period helical spin density waves due to the antisymmetric and symmetric exchange interactions. *Journal of the Physical Society of Japan*, 56(10):3635–3647, 1987.

[138] PJ Metaxas, JP Jamet, A Mougin, M Cormier, J Ferré, Vincent Baltz, B Rodmacq, B Dieny, and RL Stamps. Creep and flow regimes of magnetic domain-wall motion in ultrathin pt/co/pt films with perpendicular anisotropy. *Physical review letters*, 99(21):217208, 2007.

[139] Lorenzo Camosi. *Toplogical magnetic solitons in thin epitaxial films with reduced symmetry*. PhD thesis, Université Grenoble Alpes, 2018.

[140] Kowsar Shahbazi, Aleš Hrabec, Simone Moretti, Michael B Ward, Thomas A Moore, Vincent Jeudy, Eduardo Martinez, and Christopher H Marrows. Magnetic properties and field-driven dynamics of chiral domain walls in epitaxial pt/co/au x pt 1- x trilayers. *Physical Review B*, 98(21):214413, 2018.

[141] José AC Broekaert. Daniel c. harris: Quantitative chemical analysis, 2015.

[142] C Chappert, K Le Dang, P Beauvillain, H Hurdequint, and D Renard. Ferromagnetic resonance studies of very thin cobalt films on a gold substrate. *Physical Review B*, 34(5):3192, 1986.

[143] Patrick Bruno. Magnetic surface anisotropy of cobalt and surface roughness effects within neel's model. *Journal of Physics F: Metal Physics*, 18(6):1291, 1988.

[144] Lev Aleksandrovich Shuvalov et al. *Modern Crystallography IV: Physical Properties of Crystals*. Springer, 1988.

[145] L Albini, G Carlotti, G Gubbiotti, M Madami, and S Tacchi. In situ investigation of ultrathin fe/cu (110) films by brillouin light scattering. *Journal of Applied Physics*, 89(11):7383–7385, 2001.

[146] Jürgen Fassbender, G Güntherodt, CH Mathieu, B Hillebrands, R Jungblut, J Kohlhepp, MT Johnson, DJ Roberts, and GA Gehring. Correlation between structure and magnetic anisotropies of co on cu (110). *Physical Review B*, 57(10):5870, 1998.

[147] Lijun Zhu, Xin Ma, Xiaoqin Li, and Robert A Buhrman. Interfacial dzyaloshinskii-moriya interaction and spin-orbit torque in au1-xptx/co bilayers with varying interfacial spin-orbit coupling. *arXiv preprint arXiv:2007.09817*, 2020.

[148] Xin Ma, Guoqiang Yu, Chi Tang, Xiang Li, Congli He, Jing Shi, Kang L Wang, and Xiaoqin Li. Interfacial dzyaloshinskii-moriya interaction: Effect of 5 d band filling and correlation with spin mixing conductance. *Physical review letters*, 120(15):157204, 2018.

[149] Harihar Behera and Gautam Mukhopadhyay. Fermi velocity modulation in graphene by strain engineering. In *AIP Conference Proceedings*, volume 1512, pages 360–361. American Institute of Physics, 2013.

[150] Dayane de Souza Chaves. *The dynamics of chiral domain walls in multilayer films with perpendicular magnetic anisotropy*. PhD thesis, Université Grenoble Alpes, 2018.

[151] Marlio Bonfim. *Micro bobines à champ pulsé: applications aux champs forts et à la dynamique de renversement de l'aimantation à l'échelle de la nanoseconde par effet Kerr et dichroïsme circulaire magnétique de rayons X*. PhD thesis, Université Joseph-Fourier-Grenoble I, 2001.

[152] Arne Vansteenkiste, Jonathan Leliaert, Mykola Dvornik, Mathias Helsen, Felipe Garcia-Sanchez, and Bartel Van Waeyenberge. The design and verification of mumax3. *AIP advances*, 4(10):107133, 2014.

[153] Jonathan Leliaert, Mykola Dvornik, Jeroen Mulkers, Jonas De Clercq, MV Milošević, and Bartel Van Waeyenberge. Fast micromagnetic simulations on gpu—recent advances made with. *Journal of Physics D: Applied Physics*, 51(12):123002, 2018.

[154] J Stöhr, HA Padmore, S Anders, T Stammler, and MR Scheinfein. Principles of x-ray magnetic dichroism spectromicroscopy. *Surface review and letters*, 5(06):1297–1308, 1998.

[155] Peter Fischer and Hendrik Ohldag. X-rays and magnetism. *Reports on Progress in Physics*, 78(9):094501, 2015.

[156] Lorenzo Camosi, Jose Peña Garcia, Olivier Fruchart, Stefania Pizzini, Andrea Locatelli, Tevfik Onur Menteş, Francesca Genuzio, Justin M Shaw, Hans T Nembach, and Jan Vogel. Self-organised stripe domains and elliptical skyrmion bubbles in ultra-thin epitaxial au0. 67pt0. 33/co/w (110) films. *New Journal of Physics*, 23(1):013020, 2021.

[157] Gong Chen, Alpha T N'Diaye, Sang Pyo Kang, Hee Young Kwon, Changyeon Won, Yizheng Wu, ZQ Qiu, and Andreas K Schmid. Unlocking bloch-type chirality in ultrathin magnets through uniaxial strain. *Nature communications*, 6(1):1–7, 2015.

[158] AB Kashuba and Valery L Pokrovsky. Stripe domain structures in a thin ferromagnetic film. *Physical Review B*, 48(14):10335, 1993.

[159] TNG Meier, M Kronseder, and CH Back. Domain-width model for perpendicularly magnetized systems with dzyaloshinskii-moriya interaction. *Physical Review B*, 96(14):144408, 2017.

[160] Wanjun Jiang, Pramey Upadhyaya, Wei Zhang, Guoqiang Yu, M Benjamin Jungfleisch, Frank Y Fradin, John E Pearson, Yaroslav Tserkovnyak, Kang L Wang, Olle Heinonen, et al. Blowing magnetic skyrmion bubbles. *Science*, 349(6245):283–286, 2015.

[161] Roméo Juge, Soong-Geun Je, Dayane de Souza Chaves, Liliana D Buda-Prejbeanu, José Peña-Garcia, Jayshankar Nath, Ioan Mihai Miron, Kumari Gaurav Rana, Lucia Aballe, Michael Foerster, et al. Current-driven skyrmion dynamics and drive-dependent skyrmion hall effect in an ultrathin film. *Physical Review Applied*, 12(4):044007, 2019.

[162] XS Wang, HY Yuan, and XR Wang. A theory on skyrmion size. *Communications Physics*, 1(1):1–7, 2018.

[163] Jing Xia, Xichao Zhang, Motohiko Ezawa, Qiming Shao, Xiaoxi Liu, and Yan Zhou. Dynamics of an elliptical ferromagnetic skyrmion driven by the spin–orbit torque. *Applied Physics Letters*, 116(2):022407, 2020.

[164] Roméo Juge, Soong-Geun Je, Dayane de Souza Chaves, Stefania Pizzini, Liliana D Buda-Prejbeanu, Lucia Aballe, Michael Foerster, Andrea Locatelli, Tevfik Onur Menteş, Alessandro Sala, et al. Magnetic skyrmions in confined geometries: Effect of the magnetic field and the disorder. *Journal of Magnetism and Magnetic Materials*, 455:3–8, 2018.

[165] Joo-Von Kim and Jeroen Mulkers. On quantifying the topological charge in micromagnetics using a lattice-based approach. *IOP SciNotes*, 1(2):025211, 2020.

[166] G Siracusano, R Tomasello, A Giordano, V Puliafito, B Azzerboni, O Ozatay, M Carpentieri, and G Finocchio. Magnetic radial vortex stabilization and efficient manipulation driven by the dzyaloshinskii-moriya interaction and spin-transfer torque. *Physical review letters*, 117(8):087204, 2016.

[167] Vedat Karakas, Aisha Gokce, Ali Taha Habiboglu, Sevdenur Arpaci, Kaan Ozbozduman, Ibrahim Cinar, Cenk Yanik, Riccardo Tomasello, Silvia Tacchi, Giulio Siracusano, et al. Observation of magnetic radial vortex nucleation in a multilayer stack with tunable anisotropy. *Scientific reports*, 8(1):1–9, 2018.

[168] NS Gusev, AV Sadovnikov, SA Nikitov, MV Sapozhnikov, and OG Udalov. Manipulation of the dzyaloshinskii–moriya interaction in co/pt multilayers with strain. *Physical review letters*, 124(15):157202, 2020.